

An Exploration of Conifer Canopy Anisotropy:
3D Modeling Versus Airborne Imaging Spectrometer and
Multispectral Scanner Imagery

by


Charles Nils Burnett

B.Sc., University of Alberta, Edmonton, 1993


A Thesis Submitted in Partial Fulfilment of the
Requirements for the Degree of
MASTER OF SCIENCE


in the Department of Geography

We accept this thesis as conforming
to the required standard


Dr. K. O. Niemann, Supervisor (Department of Geography)


Dr. M. Sondheim, (Department of Geography, Adjunct)


Dr. N. J. Livingston, (Department of Biology)


Dr. D. Goodenough, External (Pacific Forestry Centre, Canadian Forest Service)

© Charles Nils Burnett, 1999

University of Victoria

All rights reserved. This thesis may not be reproduced in whole or in part,
by photocopy or other means, without the permission of the author.

Supervisor: Dr. Olaf Niemann

ABSTRACT

Canopy biophysical data measured in the field was compared to modeled simulations of bidirectional reflectance (BR) and to airborne hyper-spectral and multi-spectral scanner imagery. The simulations were produced using a 3D computer graphics implementation of the geometric-optical model of Li and Strahler (1984). Two independent experiments were undertaken. In the first experiment, a solar position change of 7° in zenith and 68° in azimuth produced changes in reflectance from Douglas-fir (*Pseudotsuga menziesii*) forest stands on Vancouver Island. AVIRIS-measured change and 3D-modeled reflectance change were compared for 5 conifer stands ranging in age from 20 to 150 years. Sites 8, 9 and 10 contained mature ($>30\text{m}$ in height) Douglas fir stands, while site 7 and 6 were populated by 30 year old and 10 year old trees respectively. Change in values recorded by the spectrometer varied with wavelength. In the 700-800nm range, a grouping pattern of sites 8, 9, and 10 separate from sites 7 and 6 was discernible, suggesting even with only a $7^\circ/68^\circ$ change in solar position, canopy shape may have a measurable effect on reflectance. Topography was incorporated into a second iteration of the first experiment, resulting in change estimates closer to the measured reflectance. Firm relationships between change and biophysical parameters were neither found nor expected with so few BR measurements and with the use of end-member reflectance values that were extracted from the literature rather than *in situ*.

In the second experiment, semi-hemispheric bidirectional reflectance functions were calculated at two spectral wavelengths for two stands (aged 40 and 150 years) using the 3D graphical modeling method described above, but with modifications to the input variables. These functions were compared against each other and then compared to canopy measurements from multi-spectral airborne imagery.

Ray-traced renderings demonstrate very accurate calculation of the areal extent of each of the four Li and Strahler geometric-optical model (GOM) components; however, the model is too simplistic for accurate BR modeling. For example, the differences in the BR change due to wavelength suggest the importance of introducing spectral parameters to the GOM. If the spectral information is incorporated into a 3D graphics/ray-tracing approach to modeling, the method could provide a powerful tool for the estimation of BR corrections for remotely sensed imagery acquired over topographically complex areas. This implementation of a simple version of the Li and Strahler model has demonstrated some of the strengths and weaknesses of using models in forest canopy research.

Examiners:

[Redacted]

Dr. K. O. Niemann, Supervisor (Department of Geography)

[Redacted]

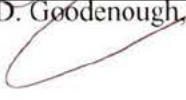
Dr. M. Sondheim, (Department of Geography, Adjunct)

[Redacted]

Dr. N. J. Livingston, (Department of Biology)

[Redacted]

Dr. D. Goodenough, External (Pacific Forestry Centre, Canadian Forest Service)



Acknowledgements

My gratitude to Dr. Goodenough for making available the two RS datasets used in this thesis, and for his useful suggestions at key moments of the research. My thanks to Dr. Niemann for his mentorship, his assistance in sending me to the International Airborne Conference in Copenhagen in 1997 and for access to the fine Spatial Sciences Lab facilities. My thanks to Dr. D. Leckie for his enthusiasm for and support of this project.

My gratitude and love to Families Jones and Cameron and the rest of the staff and students at SMUS for giving Lily and I a home. Special thanks to Dr. M. Wulder, L. B. Miller and Dr. M. Burnett who were my editors and much more. My thanks to family and friends, for assistance and support as I rolled a-long.

TITLE PAGE	i	v
ABSTRACT		ii
LIST OF EXAMINERS		iii
ACKNOWLEDGEMENTS		vi
TABLE OF CONTENTS		v
TABLE OF FIGURES		viii
TABLE OF TABLES		x
1. INTRODUCTION AND RESEARCH OBJECTIVES		1
1.1. Introduction		1
1.2. Defining Concepts		2
1.2.1. The remotely sensed scene		2
1.2.2. Bidirectional reflectance		3
1.2.3. The canopy reflectance model		7
1.3. Research Objectives		8
1.4. Organization of the Thesis		9
2. LITERATURE REVIEW		9
2.1. Forest Bidirectional Reflectance		9
2.1.1. The hot spot		11
2.2. Forest BR Measurement Campaigns		12
2.3. Forest BR and Modeling		15
2.3.1. The Li and Strahler geometric-optical model		16
2.3.2. Inversion: the grail		18
2.3.3. Terrain Effects		19
2.4. Chapter Summary		21
3. METHODS		22
3.1. Introduction & Study Area		22

		vi
3.2.	Experiment 1: AVIRIS Measured And Modeled BR Versus Field Data	25
3.2.1.	Study Site Description	25
3.2.2.	AVIRIS data collection	27
3.2.3.	AVIRIS Processing	28
3.2.4.	ΔR (reflectance) extraction form AVIRIS images	30
3.2.5.	Stand model building	31
3.2.6.	Estimation of end-member areal extent	37
3.2.7.	Calculation of R_{pixel}	38
3.3.	Experiment 2: MEIS-II BR and Modeled BR Versus Field Data	39
3.3.1.	Study site descriptions	39
3.3.2.	Stand model building	41
3.3.3.	Estimation of end-member areal extent	42
3.3.4.	MEIS II data collection & processing	43
3.3.5.	R (radiance) values for MEIS-II modeling	44
3.3.6.	Calculation of R (pixel)	46
3.3.7.	Determination of L-resolution MEIS values	48
3.4.	Chapter Summary	49
4.	RESULTS & ANALYSIS	50
4.1.	Introduction	49
4.2.	Experiment 1: AVIRIS BR	49
4.2.1.	ΔR_{AVIRIS} (R_{829} versus R_{902})	49
4.2.2.	Predicted change from BR model	60
4.2.3.	ΔR_{AVIRIS} vs. Site Biophysical Parameters	62
4.3.	Experiment 2: MEIS-II BR	64
4.3.1.	Results: bidirectional radiance hemisphere modeling	64
4.3.2.	Analysis: $R_{MEIS-II}$ vs R_{MODEL} (1st Run)	68
4.3.3.	Analysis: R_{MEISII} versus R_{MODEL} (Final Run)	70
4.4.	Chapter Summary	71
5.	SUMMARY AND CONCLUSIONS	73
5.1.	Summary	73

		vii
5.1.1	Experiment 1: AVIRIS BR	74
5.1.2.	Experiment 2: MEIS –II versus ray-tracing-based GOM	75
5.2.	Conclusions	77
5.3.	Future Research	78
Appendix A. Glossary		79
Appendix B. Bibliography		80
Appendix C. Sensors		86
Appendix D. Solar Angle Calculation		90
Appendix E. POV-Ray Source Code		94

Table of Figures

Figure 1-1. BR in airborne video imagery (from Pellikka, 1998)	3
Figure 1-2. An example of bidirectional reflectance change	5
Figure 1-3. Four plots of the directional distribution of (from Deering 1989)	6
Figure 2-1. Geometry of BRDF equation	10
Figure 2-2. Color composite images of three flightlines of ASAS	13
Figure 2-3. Bidirectional reflectance for spruce and pine stands	14
Figure 2-4. Geometry of an illuminated crown and its shadow and demonstration	17
Figure 2-5. Schematic showing the effects of terrain on the shadowing effects	20
Figure 3-1. Flow diagram of AVIRIS BR experiment	23
Figure 3-2. Flow diagram of MEIS-II Modeling experiment	24
Figure 3-3. Study site locations at Sooke Lake, Vancouver Island	25
Figure 3-4. Band 36 of August 29 AVIRIS image, radiometrically corrected	29
Figure 3-5. August 29 AVIRIS band 36 with Delaunay triangulation warp	30
Figure 3-6. September 02 AVIRIS band 36 image with Delaunay warp	30
Figure 3-7. Modeled site 10 stand, using perspective camera	32
Figure 3-8. Tree parameters collected in field visits	36
Figure 3-9. Demonstration of the incorporation of slope and aspect into model	37
Figure 3-10. Nadir view of modeled Site 10 stand	38
Figure 3-11. Oblique photograph looking south at the Experiment 2 location	40
Figure 3-12. Oblique view of modeled MEIS-II experiment stands	42
Figure 3-13. An RGB (ch6, ch4, ch3) cropped MEIS-II image of the Haysite	44
Figure 3-14. Radiance of transects through immature and mature canopies	45
Figure 3-15. Extraction of R end-member values by point sampling	46
Figure 3-16. Modeling areal proportions with different solar zenith	47
Figure 3-17. L-resolution sample areas in MEIS-II image	50
Figure 4-1. Site 10 AVIRIS mean reflectance of 3x3 sample	51
Figure 4-2. Site 9 AVIRIS mean reflectance of 3x3 sample	52
Figure 4-3. Site 8 AVIRIS mean reflectance of 3x3 sample	53
Figure 4-4. Site 7 AVIRIS mean reflectance of 3x3 sample	54
Figure 4-5. Site 6 AVIRIS mean reflectance of 3x3 sample	55
Figure 4-6. Summary of spectral areas of separability	57
Figure 4-7. Plot of change in percentage points between AVIRIS images	58
Figure 4-8. Plot of normalized change in percentage points between images	59
Figure 4-9. Suggested BR Working Set	60

Figure 4-10. Ray-tracing output showing gradations of shadow	65
Figure 4-11. Semi-hemispheric models: immature canopy at 641 and 875 nm	67
Figure 4-12. Semi-hemispheric models: mature canopy at 641 and 875 nm	66
Figure 4-13. Radiance change with change in sunlit background (R_g) value	69
Figure 5-1. Ray-traced model of Englemann spruce using ray-tracing modeling software	78
Figure D-1. Horizon coordinates (from Duffett-Smith, 1979)	91
Figure D-2. Equatorial coordinates on the celestial sphere	91

Tables

Table 3-1. Ages, stem density numbers, height and LAI for AVIRIS experiment	26
Table 3-2. Species composition in percent and DBH for AVIRIS experiment	26
Table 3-3. AVIRIS sensor specifications by spectrometer	27
Table 3-4. AVIRIS flight specifications for passes used in AVIRIS experiment	28
Table 3-5. Solar position data for AVIRIS experiment	33
Table 3-6. Site-specific tree model equations	35
Table 3-7. MEIS-II filter specifications	43
Table 3-8. Numerical analysis of component areal extents	48
Table 4-1. Component areal extent by ray-tracing (from Burnett <i>et al.</i> , 1997)	61
Table 4-2. Final model predicted component areal extent and reflectance change	62
Table 4-3. Comparison between biophysical parameters, ΔR and modeled ΔR	63
Table 4-4. Image derived component radiance values and derivation for modeling runs	66
Table 4-5. Comparison between MEIS-II radiance measures and model estimates	68
Table C-1. AVIRIS sensor specifications	87
Table C-2. AVIRIS flight specifications	87
Table C-3. Stereo A MEIS II filter set, 1993	88
Table C-4. MEIS-II specifications	89
Table D-1 Solar position at time of AVIRIS flight	90

1. Introduction and Research Objectives

1.1. Introduction

When solar radiation is incident on a vegetation canopy it is scattered and reflected and the direction and spectral composition of the reflected radiation is altered in complex ways by the scene elements (needles or leaves, branches and trunks) and groups of elements. For optical remote sensing purposes, part of this altered and reflected radiation is intercepted and measured by a remotely positioned sensor (Goel 1989). The extraction of useful information depends upon the ability to relate these remote measurements to the state of vegetated surface as defined by biophysical properties such as biomass, leaf area index (LAI), fraction of incident photosynthetically active radiation absorbed by the canopy (F_{apar}), canopy gap fraction and canopy roughness (Z_o). Biophysical properties are determined by *internal* factors (such as dominant species composition and architecture, needle age, nutrition and water content, understory composition and architecture, litter composition, exposed bedrock and soil characteristics and slope and aspect, and their measurement is complicated by *external* factors such as illumination position and sensor position. The measured reflectance of the surface depends not only on the biochemical properties and structure of that surface but also on the relative positions of the source of light and the sensor. This phenomenon is called anisotropy or **bidirectional reflectance** (BR), and the neatness of its name belies the challenges it poses to the remote sensing community.

BR describes the preferential reflectance of solar radiation from a terrestrial surface (Colwell 1974; Deering 1989; Kimes *et al.* 1987). By 'preferential', it is meant that re-radiated energy is not distributed equally throughout the hemisphere. The distribution pattern is unique to each surface and based upon surface characteristics such as structure and chemical composition. For instance, it is common for a surface to re-radiate more energy back towards the direction of direct illumination (backscatter) and less away (fore-scatter). Remotely placed sensors located at different position of the hemisphere will, thus, record different measurements for the same surface. Examples of BR effects for bare soil, an agricultural crop and a forest are given below. In this thesis, the characteristics of forested surfaces are further examined to better understand the factors affecting BR distribution. BR presents many challenges to practitioners of remote sensing. These challenges include making a comparison between canopies measured at different times (complicated by different illumination positions or from different sensor positions), and finding a solid empirical relationship between discrete remotely sensed measures and canopies

that vary over time and space in terms of composition and architecture. On the other hand, other investigators have suggested that since BR is a function of canopy parameters, there exists the potential to extract those parameters from measurements of BR (Goel 1989; Barnsley *et al.* 1994; Ranson *et al.* 1994)

In this thesis, I sought to develop a better understanding of the BR of conifer canopies through a comparison of airborne measurements of anisotropy and computer graphics simulations calibrated with known positions of sensor and sun, and position and dimensions of scene elements (trees). The hypotheses underlying this thesis are that (1) stand-level reflectance for canopies exhibiting distinct geometric features, such as conifers, is strongly related to shadow fraction, sunlit canopy fraction, sunlit background fraction, and their reflectances (Hall *et al.* 1995); (2) changes in the proportions of these fractions are related to canopy structural changes (Goel 1989); and (3) canopy structure relates to the age and species of trees found within the stand (Nilson and Petersen 1994).

1.2. Defining Concepts

At this point it will be useful to describe the framework within which the experiments were conducted. The following sections introduce some basic remote sensing terminology and canopy modeling concepts pertinent to the research undertaken.

1.2.1. The remotely sensed scene

Remote sensing is a technique used to obtain information about an object, area or phenomenon through analysis of data acquired by a device that is not in contact with the object, area or phenomenon under investigation (Lillesand and Kiefer 1987). A sensor records scenes as a composite of (ideally) adjacent non-overlapping picture elements, or **pixels**, each of which is a measure of the up-welling radiation integrated over the sensor instantaneous field of view (IFOV), usually expressed in milliradians. In the case of airborne scanning devices (such as the two employed in this thesis), an image is constructed from the radiance values sequentially recorded at each position of the IFOV. The instrument's optical system and the size of the detector array (Lillesand and Kiefer 1987) determine the IFOV of a scanning instrument. The instrument's ground resolution cell (GRC) is a function of the altitude and speed of the platform and the IFOV. Pixel composition is, in turn, a function of the GRC size and the size and distribution of the scene elements. For example, the signal that is recorded by a sensor above a conifer forest will be an integration of the direct and indirect reflectance from needles, stems, branches, boles, understory vegetation, soils and litter (Guyot *et al.* 1989). These elements are

often grouped into minimum resolvable entities called *image-objects* (Hay *et al.* 1997), which, for current sensor technology, would be ‘trees.’

1.2.2. Bidirectional reflectance

If the GRC/canopy biophysical relationship determines the value recorded at the sensor, then it is the vegetation canopy BR that determines the *relative* tone (i.e. the range of possible values) on the remote sensing imagery collected in the short wave (0.3-3.0 μm) part of the spectrum (Colwell 1974). The most conspicuous example of this phenomenon is the brightening of an image in the backscatter (towards the direction of the illumination) direction. This effect is called the **hot spot** or *heligensheim* and is caused by the hiding of shadows by illuminated elements in the scene, when the illumination and sensor angles converge. An illustration of BR-produced radiance variation is presented in Figure 1-1, top panel (from Pellikka 1998).

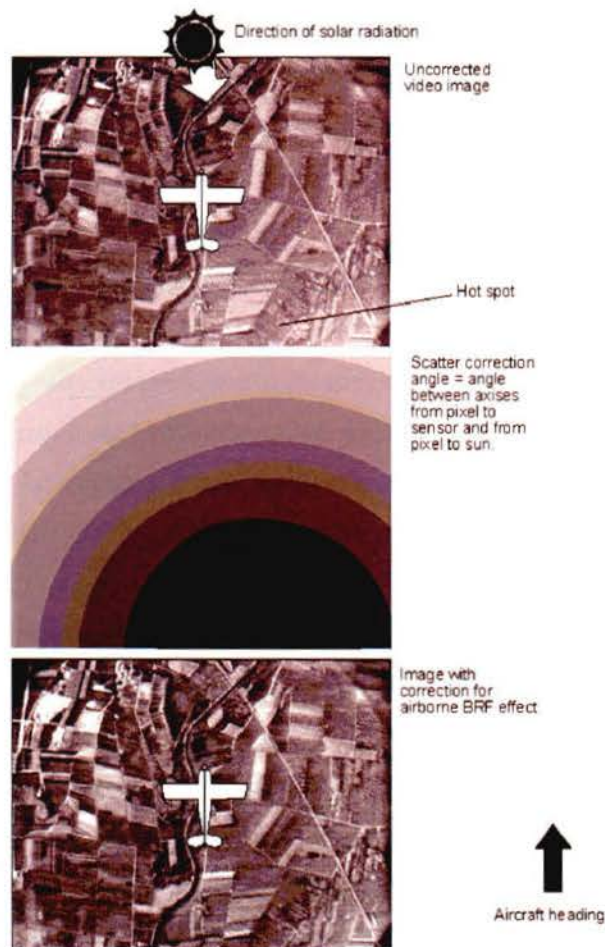


Figure 1-1. BR in airborne video imagery: panel 1, BR in a single image; panel 2, distribution and hotspot effect; panel 3, image after correction (from Pellikka, 1998).

The fields in the south of the image appear brighter because the sensor 'view' of the shadowed areas is blocked by sunlit elements. As presented in Figure 1-1 (middle panel), the BR effect (the darkest region equals the area of greatest hotspot effect) exists across the video image, changing the intensity of recorded radiance relative to sensor and illumination positions. Removal of BR effects may be done through empirical means (i.e. comparison between the same feature type in different parts of the image) but is complicated when an image is very heterogeneous. The bottom panel of Figure 1-1 is an example of an empirically corrected image.

For a forest canopy, illumination source position controls the amount of shadow cast by trees (i.e. the higher the solar position the shorter the shadows) whereas the sensor position controls how much of the shadow component makes up the GRC. Figure 1-2 shows the latter effect. By recording fore-, aft- and nadir-looking views, the Multispectral Electro-optical Imaging Spectrometer II (MEIS-II) sensor effectively records from three different sensor positions at the same canopy-sun geometry. In the example, the sun azimuth is approximately 100°. Note the tone of the imagery within the white circle in each panel. The tone is lightest in the top panel (fore-view) because the sensor GRCs are filled with sunlit crowns, the shadows hidden behind said crowns. The middle (nadir-viewed) image has a moderate tone, with both sunlit and shadowed portions of the crown composing a pixel. The bottom panel, showing the aft-view, is the darkest due to the large proportion of shadowed surfaces making up the pixel GRCs.

In keeping with conventions found in the remote sensing literature, the abbreviation BR is used in this thesis to represent both bidirectional reflectance and bidirectional radiance. Reflectance is equal to the radiance divided by the amount of total incident radiation. Though perhaps ambiguous, I believe this convention to be harmless since BR describes a phenomenon and not a measurement that can be described in units. By referring to BR, the user is implying that the directional characteristics of a surface are being examined. The MEIS imagery shown in Figure 1-2 had not been corrected to reflectance. It should be noted that, for a given location on the ground, the recorded differences are the result of BR (position of sensor in hemisphere) convolved with the effects of path radiance (distance from target to sensor). A proportion of the signal measured at the sensor is not energy upwelling from the surface, but is energy directed into the path of the sensor by scattering of energy in the atmosphere between the surface and sensor. The longer the 'path' between the sensor and target, the more scattered energy will contribute to the signal, and oblique views produce longer paths.

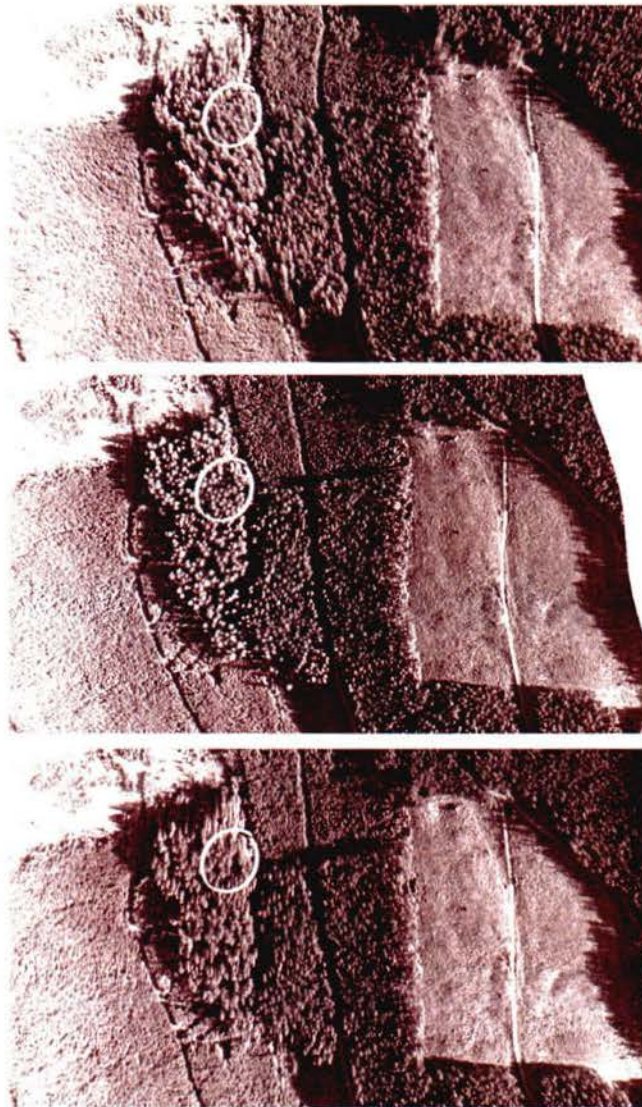


Figure 1-2. An example of bidirectional reflectance change caused by changes in sensor location, from top panel down: MEIS-II channel 4 (fore-looking), channel 6 (nadir-looking) and channel 0 (aft-looking). Motion of aircraft is towards the top of the page.

A third demonstration of BR is given in Figure 1-3. The three dimensional (3D) reflectance plots of tallgrass prairie shown here are interpolated from multiple measurements acquired with a boom-mounted radiometer by Deering (1989). Note that with the sun at 180° azimuth (1-3a), the hotspot shows strongly in the backscatter (NE, back towards the illumination source) direction in (1-3b&c). The reason for Figures 1-3d being bowl shaped relates to the canopy structure of this ecotype/system. Viewed from any direction but from the vertical, the dense sheaves of grass hide all parts of the background from the sensor and result in a relatively bright signal. Only from nadir will the pixel signal incorporate any soil background, and thus darken.

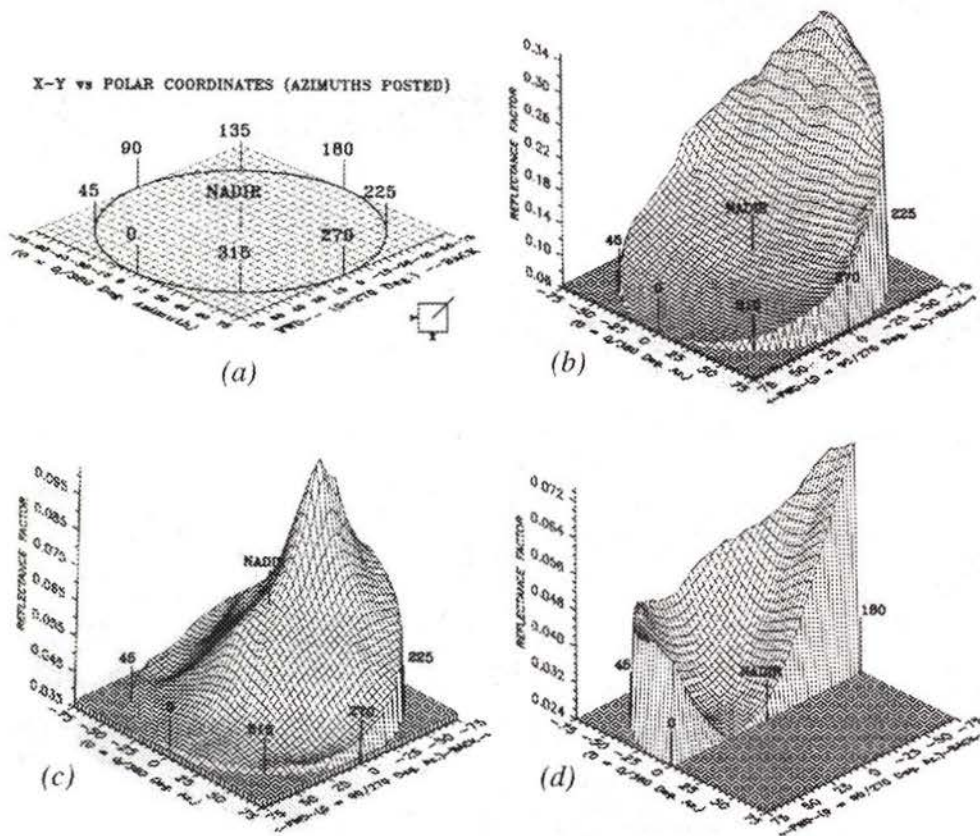


Figure 1-3. Four plots of the directional distribution of reflectance caused by change in view angle: (a) polar-coordinate system viewing azimuths (posted) represented on a Cartesian (x-y) plane as used in three-dimensional plotting. View zenith angles are shown out to $\pm 75^\circ$, as shown on the x-y-axis label; (b) Recently plowed bare-soil field; (c) 662nm sand shinnery oak-oak-rangeland community (at SZA=31°); (d) 662nm tall grass prairie grassland community (at SZA=48°); (from Deering 1989).

1.2.3. The canopy reflectance model

As the objects in the scene decrease in size relative to the sensor GRC, relating pixel values directly to scene elements (or more specifically, to scene element parameters such as LAI, height or age) becomes more difficult. This is because a relatively large GRC will contain spectral information from neighbouring objects and/or background. On the other hand, a relatively small GRC may provide numerous measurements (pixels) of a single object. This is the basis for the concepts of pixel purity and scale in remote sensing.

Models offer a means of exploring object/GRC relationships and Goel (1987) reports on over 75 models specific to the vegetation canopy. Canopy reflectance (CR) models employ a wide variety of methods to represent the vegetation-radiation space. These methods include

computer simulation models, turbid medium models, geometric models, and hybrid combinations. The underlying commonality of CR models is their intent to relate a discrete pixel measurement (or measurements, if multispectral or multi-directional information is being examined) to a set of scale and space continuous processes. One solution to this problem is to model each pixel as a combination of component scene elements or image objects. This approach is called mixture modeling or spectral mixture analysis. Mixture modeling was alluded to in the above discussion of the hotspot, where a single pixel was described as being composed of a finite number of scene elements.

The CR model used in this thesis is the geometric optical model developed by Li and Strahler (1985; 1986; 1992) which treats the canopy as a mixture of large, three dimensional, vegetation-filled objects that are distinct from each other and are placed on a contrasting background. When viewed at nadir and with a mono-directional light source, these geometric objects cast shadows onto each other and the background. Taking a linear mixture modeling approach, Li and Strahler (1985; 1986; 1992) decompose the resultant modeled scenes into three or four scene elements (or end-members): sunlit and shaded crown, and sunlit and shaded background. In this thesis, 3D graphics are used to build the simulated scene as opposed to the mathematical modeling found in Li and Strahler (1985; 1986; 1992). Comparisons are then made between the (actual) measured radiance or reflectance values and the (modeled) areal proportions of the four end-members as calculated from the 3D graphics ‘snap shots’ for given illumination solar zenith and solar azimuth angles (SZA & SAA).

1.3. Research Objectives

The objective of this research is to contribute to an understanding of conifer bidirectional reflectance as defined by the following questions:

1. *To what extent is canopy structure a factor of BR in conifer forest canopies; and*
2. *How does stand age change the canopy structure / reflectance relationship in a Douglas-fir (*Pseudotsuga menziesii*) forest?*

Comparing modeled simulations of BR to airborne measurements of real-world anisotropy is one approach to answering these questions. The simulations were produced using a computer graphics implementation of the geometric optical model of Li and Strahler (1985; 1986; 1992). A secondary research question was posed, which was derived from an examination of the thesis method:

3. *What are the benefits of using a 3-D graphics implementation of the geometric optical model?*

The following two experiments were designed as attempts to address these research questions:

Experiment 1. To explore the extent to which BR relationships exist and change with solar position in a Douglas-fir forest, remotely sensed measurements of reflectance and tree characteristics were acquired for stands of various ages. Ground measures of canopy biophysical characteristics included leaf area index (LAI) and diameter at breast height (DBH). Canopy reflectance change was recorded remotely by airborne imaging spectrometer at two times of the day. Time changes resulted in solar position changes of 7° in the zenith and 68° in the azimuth. Predicted change was then estimated using a computer-generated simulation incorporating sun-position data, canopy data, and site slope and aspect. Comparisons were made between the measured change, modeled change, and canopy biophysical parameters.

Experiment 2. Four BRF plots were calculated in order to refine the modeling method and to compare the differences between modeled semi-hemispheric distributions of BR factors and actual canopy biophysical characteristics. Plots were calculated for a mature and an immature stand of Douglas-fir at two spectral wavelengths. These BRF plots were compared to one another and to airborne multispectral scanner imagery.

Flow diagrams describing each experiment are provided in Figures 3-1 and 3-2.

1.4. Organization of the Thesis

The thesis is divided into 5 chapters. Context for the research, a description of the research objectives and a layout of the thesis document are provided in the Introduction Chapter. In the Literature Review chapter, a more detailed exploration of the terminology and concepts used in remote sensing and forest canopy modeling is presented. The Literature Review chapter is subdivided into sections on forest BR, measurements of forest BR, and modeling of forest BR. The backbone of the thesis is the assumptions and steps taken to acquire results, and these are detailed in the Method chapter. The Method chapter is further broken down into descriptions of the Study Area, AVIRIS Experiment and MEIS-II Experiment. The results of the experiments are found in separate sections within the Results and Discussion chapter. A summary of each experiment, conclusions reached from the individual experiments and from a comparison between the experiments, and a section on future research make up the Summary & Conclusions chapter. The Appendices section includes a glossary, a description of the sensors used, a guide to spherical geometry and solar angle calculation and, lastly, a sample listing of a text file used to generate a 3-D graphics canopy simulation.

2. Literature Review

The literature review section is broken up into three sections. First, in the forest bidirectional reflectance (BR) section, background on the nature of BR of forest canopies is surveyed. The second section explores the varied measurement campaigns directed towards developing a further understanding of forest BR which have been conducted to date. Lastly, the forest BR modeling section describes attempts made to bridge BR theory and BR measurement with models.

2.1. Forest Bidirectional Reflectance

If an infinitely large Lambertian surface is positioned horizontally and below a remote observer it shows a hemispherical distribution of reradiation that is independent of view angle. That is, the amount of energy reradiated from the surface changes neither when the observer nor the illuminating source changes position. Every surface that is characterized by a distribution of reradiation other than this pattern is viewed as a surface of non-Lambertian distribution. The reasons for this non-Lambertian distribution are (1) roughness by Rayleigh's criterion, (2) the shadowing of the surface (which varies with the view angle), and (3) the slope of the surface (Cierniewski and Courault 1993). The basic definition of the land surface bidirectional reflectance distribution function (BRDF) is that of Nicodemus *et al.* (1977) and Swain and Davis (1978) cited in Pellikka (1998):

$$BRDF = \frac{L}{E_c} = f(q_s, a_s, q_p, a_p) \quad \text{Equation 2-1}$$

where E_c is the incident irradiance on a horizontal surface from a cone of radiation; L is the radiance reflected from the surface toward the sensor; q_s is the zenith angle of the incident direction; a_s is the azimuth angle of the incident direction; q_p is the zenith angle of the reflected direction; and a_p is the azimuth angle of the reflected direction. The geometry for Equation 2-1 is presented in Figure 2-1.

Equation 2-1 defines the directional radiation regime in terms of infinitesimally small elements of solid angle. A more practical measure, the bidirectional reflectance factor (BRF), is defined as BR measures integrated into quantities of solid angle, or "reflectance at a multitude of possible view angles at a given time or solar position (Walthall *et al.* 1985). The term 'bidirectional' in the context of the BRDF and BRF refers to the description of the angular

position of two elements, i.e. the source of (incident) radiation and terminus (the sensor) (Milton 1989, *in* Cierniewski and Courault 1993).

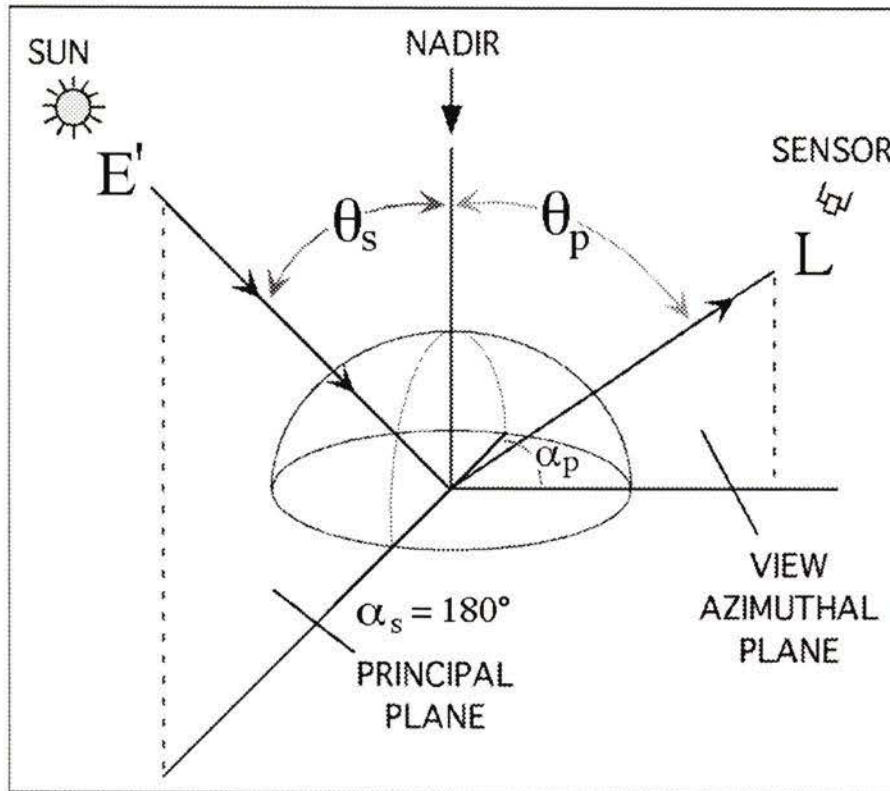


Figure 2-1. Geometry of BRDF equation defined by Nicodemus *et al.* (1977) and Swain and Davis (1978). In this case the solar azimuth is 180° . The symbols are explained in Equation. 2-1 (Deering 1989, modified from Pellikka 1998).

For both albedo and carbon cycle studies, there is a need for accurate surface reflectance data (Kimes *et al.* 1993). Models incorporating surface reflectance data often use surface albedo as an integrated measure of the directional reflectance signal. Albedo is the total reflectance of the surface integrated over all angles of the upward hemisphere, and as such cannot be directly measured by aircraft- or spacecraft-based remote sensing instrumentation (Deering 1989). Efforts to estimate albedo from remote sensing data have been constrained by the available instrumentation that typically provide observations of reflected radiance from a small number of view directions in narrow spectral bands. As a consequence, albedo is often assumed to be equivalent to nadir reflectance factor (Ranson *et al.* 1991). Errors involved in estimating hemispherical reflectance from nadir or single off-nadir reflectance measurements are high: Kimes and Sellers (1985) documented errors as great as 45%.

2.1.1. The hot spot

First discovered by Seeliger (1887; 1895) in light scattering from the rings of Saturn, the increase in brightness of a surface viewed in the backscatter direction is called heiligenschein or the hot spot (Hapke *et al.* 1996). In terrestrial laboratories the hot spot was first reported in light scattered from particulate surfaces by Oetking (1966). Examples of the hotspot in grassland and sparse woodlands can be seen in Figures 1-3(b-f). Two common BRDF surfaces are presented; the bowl-shaped grassland shape showing little hotspot and more of a general increase in reflectance from higher view zenith angles, while the sparse woodland example demonstrates a good example of a hot spot peak. This appears to be intuitively correct, as grasslands are relatively bright when viewed from the ground, but darker when viewed from above. Woodland canopies, on the other hand, are dark at higher zenith angles (side views contain more under-canopy shadow) and brightest when viewed from above (the direction producing a view with the least shadow).

Hapke *et al.* (1996) examines two potential mechanisms for the production of the hot spot: shadow hiding and coherent backscatter. If the medium consists of scatterers that are large compared with the wavelength of the incident light, they will cast well-defined shadows on the other parts of the medium. These shadows are partly visible when the surface is viewed from any direction except the direction of the source of incident light. At this specific angle each scatterer hides its own shadow and the IFOV contains the least amounts of shadow components. As viewing and illumination angles diverge, shadows gradually become visible, decreasing scene brightness, in a manner characteristic of the shape (and spatial arrangement) of the objects in the scene.

The information about the shape of the objects is, at least in principle, recoverable from directional radiance measurements. For instance, the shape (amplitude and the angular width) of the hot spot are thought to be closely related to biophysical parameters such as average leaf size, leaf-area index, and leaf-inclination angle, as well as crown size, shape and density (Gerstl and Simmer 1986; Li and Strahler 1986, 1992; Ross and Marshak 1989; Brakke and Otterman 1990; Pinty *et al.* 1989; Strahler and Jupp 1990; Jupp and Strahler 1991). Kimes *et al.* (1987) note that an understanding of BRDF characteristics of forest canopies is important for relating remote-sensing observations of biomass, species, stand structure and albedo. A relationship between forest structure, photosynthetically-active radiation (PAR), albedo and BRDF values is demonstrated in Ranson *et al.* (1994). Barnsley *et al.* (1994) conclude that it may be possible to extract detailed information about a surface, over and above that available from multispectral and

multitemporal analyses, through knowledge of its **angular reflectance properties**. The problem thus becomes one of identifying the minimum and optimum combination of view and illumination directions needed to differentiate between one vegetated canopy and another; solutions to this issue have been approached by measurement campaigns and through vegetation canopy modeling.

2.2. *Forest BR Measurement Campaigns*

Measurements of the BR characteristics of vegetation have received widespread attention over the past several years as a way to better monitor and measure the structure and state of ecosystems (Ranson *et al.* 1994). However, measurements of the BR of forest canopies have been rare, particularly near-canopy level measurements. The logistical difficulties of making measurements above forest canopies, plus the complexity of natural forest stand geometry as compared to that of row crops, are primary reasons for the paucity of forest canopy measurements from surface-based platforms (Deering *et al.* 1994). Below are examples of exceptions using airborne platforms.

Kimes *et al.* (1986) measured the directional reflectance distributions for both a hardwood and pine forest canopy as a function of sun angle from a helicopter platform using a hand-held radiometer in AVHRR band 1 (0.58 - 0.68 μm) and band 2 (0.73 - 1.1 μm). Measurements and model simulations showed that the scattering behaviour of relatively dense forest canopies is similar to the scattering behaviour of agricultural crops and natural grasslands. Only in more sparse forest canopies with significant spacing between the tree crowns (or clumps of tree crowns) does the scattering behaviour deviate from homogeneous agricultural and natural grassland canopies (Kimes *et al.* 1986).

This clumping of vegetation material has two effects on the radiant transfers within the canopy: A) it increases the probability of gap to the understory and/or soil layers that increases the scattering properties and potential of these lower layers, and B) it increases the number of low transmitting clumps of vegetation within the scene causing increased backscatter and decreased forward scatter to occur relative to the homogeneous case. Thus, for a typical forest canopy, the peak backscatter reflectance can be increased as much as 30 percent relative to an equivalent homogeneous canopy due to phenomena A and 35 percent due to phenomena B, or a cumulative increase of as much as 65 percent (Kimes *et al.* 1986).

Ranson *et al.* (1994) collected directional measures of stands containing red and black spruce (*Picea rubra* and *Picea mariana*), hemlock (*Tsuga canadensis*), white pine (*Pinus strobus*) and bog using the Advanced Solid-State Array Spectroradiometer (ASAS). ASAS, an airborne,

off-nadir pointing, imaging spectroradiometer (Irons *et al.* 1991), acquired data in 29 spectral bands in the visible and near-infrared (ca. 450-880 nm), and at seven fore-to-aft view angles (45° , 30° and 15° in the forward direction, nadir [0°], and 15° , 30° and 45° in the aft direction). Imagery was acquired at view azimuths parallel, oblique, and perpendicular to the principal plane of the sun (Figure 2-2). Normalized differential vegetation index (NDVI) values calculated from the directional reflectance measurements were assessed for sensitivity to view angle.

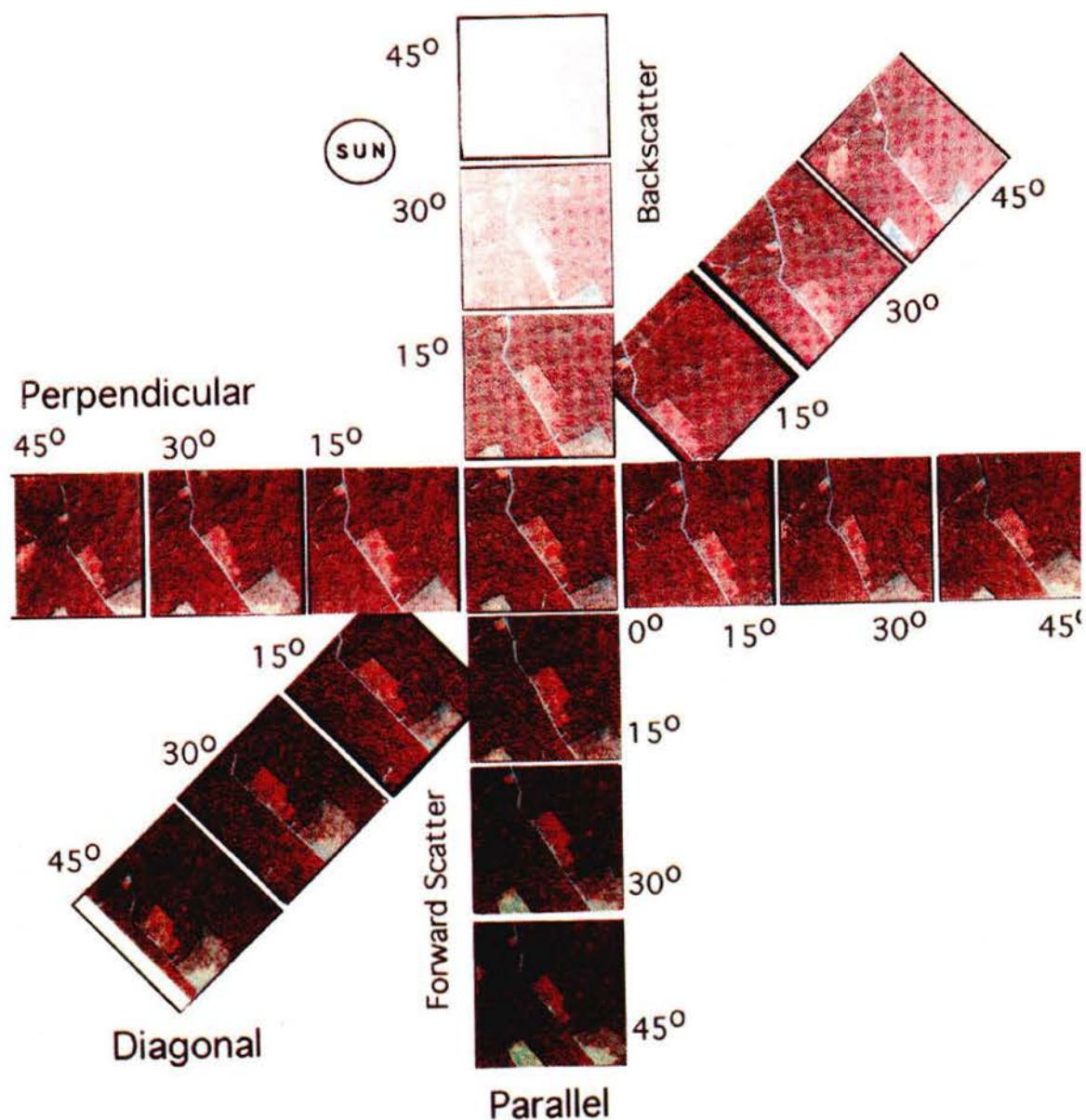


Figure 2-2. Colour composite images of three flightlines of ASAS over the spruce site acquired between 13:35 and 13:53 EDT (solar zenith angle = 43°) on 8 September 1990. These images were created from a composite of ASAS bands 25 (789 nm), 16 (658 nm), and 9 (559 nm) (from Ranson *et al.* 1994)

Maximum NDVI was measured in the forward-scattered direction and minimum NDVI was observed in the backscattered direction. Estimated fraction of absorbed photosynthetically active radiation (F_{APAR}) was determined from the hemispherical PAR reflectance for several canopy types within the forest area. Examining the relationships with NDVI revealed a strong dependence of NDVI on F_{APAR} for nadir and 45° forward-scattered data. A poor relationship was observed for data acquired at 45° in the backscattered direction and for NDVI derived from the hemispheric reflectance. From these results, it is apparent that the sensor viewing geometry that minimizes the contribution of reflectance from branches and the ground will yield higher relationships between F_{APAR} and NDVI.

Syrén (1994) concentrated on two coniferous species. Nadir-viewed reflectances of mature and young stands of Scotch pine (*Pinus sylvestris*) and Norway spruce (*Picea abies*) were measured from a helicopter in four spectral bands centred at 485 nm, 654 nm, 841 nm and 1676 nm. The results show significant increase in nadir reflectance with decreasing solar zenith angle.

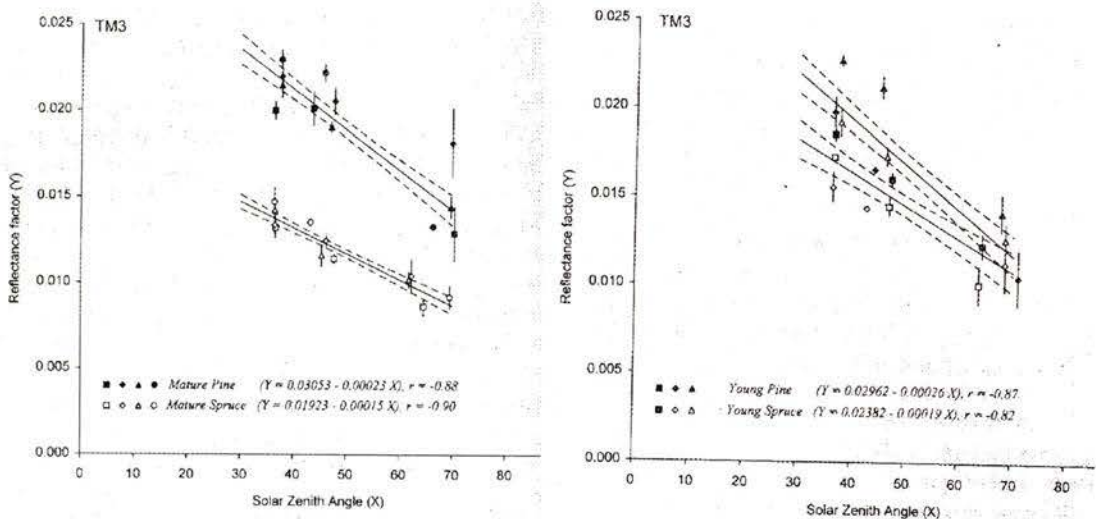


Figure 2-3. Bidirectional reflectance for spruce and pine stands at different solar zenith angles and spectral bands; (a) mature stands in TM3 channel, (b) immature stands in TM3 channel. Symbols indicate the mean value for different stands with 95% confidence interval (square = stand 1, diamond = stand 2, triangle = stand 3, circle = stand 4). Lines show best-fitted linear relationship between the solar zenith angle and reflectance and dashed lines the 95% confidence limits for prediction means (from Syrén 1994).

On average, reflectance factors increased by 1-2% for each degree of decreasing solar zenith angle. Band ratios showed that there is a disproportionate reflectance response in several of the spectral bands at varying zenith angles, *differently expressed according to stand type and age* [emphasis added] (Figure 2-3). Syrén (1994) calculated linear functions of canopy reflectance for each canopy type and produced nomograms (reflectance correction factors) for mature spruce stands, for use when normalizing multitemporal spectral data.

2.3. *Forest BR and Modeling*

The interaction of light with leaves and needles has been explored in depth through laboratory analysis (Gates *et al.* 1965; Gausman and Allen 1973; Gausman 1977). When extrapolating leaf-level properties to the stand level, however, the physical assumptions of horizontal layers of leaves do not hold, yielding unrealistic solutions (Hall *et al.* 1995). Williams (1991) reports that the magnitude of reflectance throughout the visible and near infrared wavelength region was found to decrease dramatically for the conifer species as scene complexity increased from the needle, to the branch, to the canopy level. These results emphasize the role of canopy constituents, such as needles, twigs, branches, bark, and understory material, in altering the reflectance characteristics of the overall “scene” (Williams 1991). Modeling efforts that have explored the canopy reflectance relationship are numerous, with over two dozen models having been proposed. CR models are reviewed in detail in Goel (1987). The subset of models described herein was chosen to introduce the reader to models that take into account the BR characteristics of woodland canopies and which relate to our 3D graphics model / AVIRIS & MEIS-II experiments. First, a taxonomical structure for remote sensing models suggested by Li and Strahler (1986) is described.

It is recognized that when a sensor views a scene, the recorded radiance represents an integration of the spectral reflectance characteristics of the corresponding objects in the scene convolved within the spatial resolution of the sensor (Jupp *et al.* 1988; 1989). Strahler *et al.* (1986) divides models into two classes: H and L resolution, based upon the relationship between the size of objects in the scene and size of the GRC of the image. An H-resolution model is defined as one in which the elements in the scene are larger than the resolution cells; the L-resolution model presents the opposite case. The introduction of such nomenclature is germane because both resolution situations are explored in this thesis. The 1 - 8m diameter tree crowns found in the study area are too small to be resolved in the L-resolution AVIRIS imagery (20m GIFOV) but are resolved by many pixels in the H-resolution 1 m MEIS II (1m GIFOV) imagery.

Canopy reflectance (CR) models can be placed into four general classes (Goel 1988): (1) computer simulation models, (2) turbid medium models, (3) geometric models, and (4) hybrid combinations of (2) and (3). In computer simulation models, the arrangement and orientation of vegetation elements are simulated on a computer. Each element is divided into a finite number of sub-elements and then, a Monte Carlo procedure (selection of random numbers) is used to determine if a given beam of light will hit one of the sub-elements. In this way, the interception and scattering of radiation is numerically followed. These models are computationally intensive, but they have the advantage of allowing a more realistic simulation of radiation in the canopy.

In turbid medium models, vegetation elements are treated as small absorbing and scattering particles (plates and cylinders), with given optical properties, distributed randomly in horizontal layers and oriented in given directions (Goel 1989). The canopy is usually treated as a horizontally uniform plane-parallel layer and thus the radiation field depends only on the coordinate z (perpendicular to the canopy) and not x and y . These models are successful in representing the reflectance of denser and more horizontally uniform canopies in which the vegetation elements are smaller in size than the height of the canopy (Goel 1987).

When the vegetation elements are sparsely distributed (such as with some shrub and forest canopies, orchards and planted crops in early stages of development) the canopy is best modeled using geometric means (Gauthier *et al.* 1992). Here, the scene is modeled as a ground surface (of known reflective properties) with geometrical objects or protrusions of prescribed shapes and dimensions (cylinders, spheres, cones and ellipsoids, etc.) and optical properties (reflectance, transmittance and absorptance) placed on the ground in a defined manner. The interception of light and the shadowing by the protrusions and the reflectance from the ground surface are analyzed to determine the reflectance from the canopy. The Li and Strahler geometric model (Li and Strahler 1985; 1986; Schaaf *et al.* 1994) is described as a geometric-optical model because it incorporates the optical properties of the scene elements, and so does not rely solely on shadow calculation.

2.3.1. The Li and Strahler geometric-optical model

In the geometric-optical approach, the bidirectional reflectance is modeled as a purely geometric phenomenon that results when scenes of discrete, 3D objects are illuminated and viewed from different positions in the hemisphere. The shape of the objects, their count densities and patterns of placement are the driving variables, as they condition the mixture of sunlit and shaded objects and background that is observed from a particular view direction, given a certain

direction of illumination (Li and Strahler 1986). This mixture in turn controls the brightness apparent to an observer or a radiometric instrument. Li and Strahler (1985; 1986; 1992) emphasized the individual tree canopy as the fundamental element in modeling, and have applied geometric-optical models of bidirectional reflectance successfully for open and moderately closed stands of conifers treated as “green” cones or spheroids on a contrasting background.

The geometric-optical approach is particularly well suited to describing the BR of forest and woodland canopies, where the concentration of leaf material within crowns and the resulting between-tree gaps make plane-parallel, radiative transfer models inappropriate and where tree and shadowed backgrounds interaction account for a large proportion of the variance in images (Strahler and Jupp 1990). In addition, the geo-optical approach leads to invertible formulations in which spatial and directional variance provide the means for remote estimation of tree crown size, shape and total cover from remotely sensed imagery (Strahler and Jupp 1990).

The geometric-optical models used in this thesis are that of Li and Strahler (1985; 1986). These models treat canopies as L-resolution objects; that is, a pixel is made up of many tree objects. The radiance of the pixel is an area-weighted sum of the radiance signature for three or four components, namely sunlit crown, sunlit background, and shadow (later broken into shadowed crown and shadowed background).

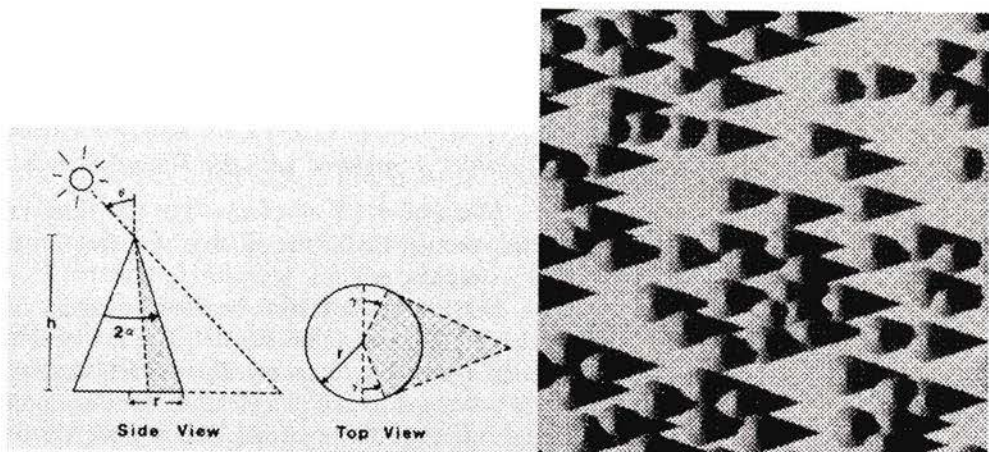


Figure 2-4. Geometry of an illuminated crown and its shadow (left) and demonstration the “Nadir-viewing cone model;” cones on a contrasting plane (right) (from Li and Strahler, 1985).

The Li and Strahler model calculates stand (pixel) reflectance R in a given spectral band as follows:

$$R = R_g \cdot g + R_c \cdot c + R_s \cdot s \quad \text{Equation 2-2}$$

where R_g is the signature of sunlit ground; R_c the signature of sunlit crown, and R_s the signature for shadowed areas. The variables g , c and s represent the proportion of the pixel that each component covers. Equation 2-2 defines the model used in the AVIRIS experiment. The model used in the MEIS-II experiment was introduced in Li and Strahler (1986) and differs in that the shadow component is further broken down into shadowed crown (R_t) and shadowed background (R_z) components:

$$R = R_g \cdot g + R_c \cdot c + R_z \cdot z + R_t \cdot t \quad \text{Equation 2-3}$$

Later refinements of the model include spheroid crown shapes instead of cones and mutual shadowing of crowns (Li and Strahler 1992), introduction of a hybrid methodology to model discontinuous canopies (Li *et al.* 1995), and incorporation of slope parameters (Schaaf *et al.* 1994). Because reflectance is represented as a linear process, the component signatures are assumed constant and thus are assumed to be independent of their relative proportions in the pixel. Interactions between component proportions and their signatures are not included, for example, multiple scattering between tree crowns and between crowns and the background can affect shadow signatures and thus signatures are not constant in reality. However, in real vegetation, especially those of low to medium densities, the variation between signatures of shadowed and sunlit, crown and background components is usually much greater than the variation within signatures of these components (Li and Strahler 1992). Thus a geometric model should be a reasonable first order approximation of stand reflectance (Gemmell 1998). Validation of the Li and Strahler model has shown reasonable agreement with measured reflectances (Abuelgasim and Strahler 1994; Schaaf and Strahler 1994).

2.3.2. Inversion: the grail

The inference of canopy biophysical characteristics from pixel-level measures of reflectance, by numerical iteration and convergence (i.e. matching reflectance values to parameter sets), is a process referred to as “inversion” (Goel and Thompson 1984). The problem with inversion, according to Hall *et al.* (1995), is that the dimensionality of the remotely sensed measurement space must equal or exceed the number of parameters that must be estimated and, in the more complex models, the number of parameters that must be estimated is large. That is, the dimensionality requirements for their inversion often exceed the intrinsic dimensionality of the airborne or satellite data. The dimensionality of remotely sensed data for a single viewing angle and date is determined by the number of independent spectral channels - generally no more than

three or four (Hall *et al.* 1995). Directional measurements and modeling may provide the missing dimensionality.

The inversion of reflectance models provides an objective method for estimating biophysical characteristics from remotely sensed data. Inversion involves adjusting model parameters until the model reflectance best matches the measured reflectance (Goel 1989). Inversion methods are applicable to all sites and sampling conditions, and do not rely on empirical calibration of reflectances against measured biophysical properties, although some knowledge of ecosystem characteristics can be used to constrain the solution domain (Privette *et al.* 1996). Studies suggest that, in practice, geometric-optical models are able to retrieve useful biophysical information (Hall *et al.* 1995; Woodcock *et al.* 1997).

Woodcock *et al.* (1997) inverted the Li - Strahler model using inputs of Landsat TM and digital terrain data. Analysis of extensive field data in the form of “test” stands from four National Forests indicate the following about the Li - Strahler model: 1) the underlying assumptions of independence between tree size and crown shape are valid, 2) the means for tree geometry parameters vary between forest types, 3) estimates of forest cover are reliable, and 4) estimates of tree size are unreliable due to a breakdown in the relationship between image intra-stand variance and tree size. Improvements in estimates of tree size will require additional data beyond a single Landsat TM image, with multidirectional data a promising possibility (Woodcock *et al.*, 1997).

2.3.3. Terrain Effects

One of the research objectives of this thesis was to assess the effect of slope and aspect when modeling BR for different conifer forest canopies. Figure 2-5 demonstrates some of the geometric effects of slope on shadowing. Terrain alters stand reflectance in three ways (Gemmell 1998). First, sloping terrain changes the areas of the shadows cast on the background. Second, mutual shadowing relations between tree crowns are altered. The net result is to alter the relative proportions of the illuminated and shadowed components observed by the sensor. Third, the component signatures are modulated relative to the flat terrain (i.e. path length through the canopy changes).

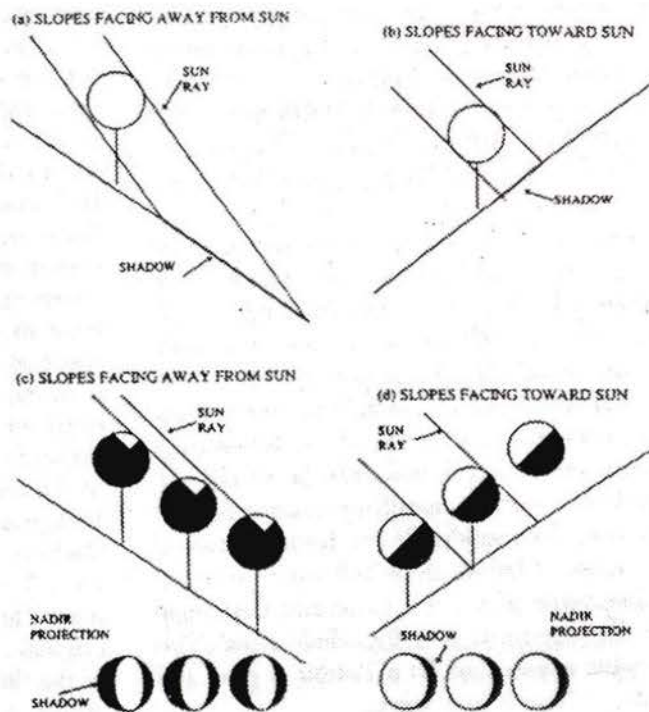


Figure 2-5. Schematic showing the effects of terrain on the shadowing effects within a forest stand. Spheres are used for simplicity. a) and b) show the effect of slope and aspect on the area of shadow cast from a single crown onto the sloping background. c) and d) show the effect of slope and aspect on the mutual shadowing relations between tree crowns (from Gemmell 1998).

Terrain effects have been addressed in several recent papers (Cavayas and Teillet 1985; Schaaf *et al.* 1994; Gemmell 1995; Woodcock *et al.* 1997; Gemmell 1998). Cavayas and Teillet (1985) simulated the effects of terrain on stand reflectance by use of a geometric-optical model and found that for certain cases of population density and solar zenith angle, the simulation results showed very significant changes in pixel reflectance. Schaaf *et al.* (1994) extend the Li and Strahler model to accommodate a sloping surface. They report that when the BRDF of a flat vegetated surface is compared to the BRDF of a sloping surface that is similarly vegetated, the interaction of the illumination angle and the slope distort the shape of the BRDF. A hemispherical integration of this distorted BRDF provides an albedo for the sloping surface. Schaaf *et al.* (1994) found that, for gentle to moderate slopes, hemispherical reflectances calculated using the Li and Strahler model remained quite similar, although the shapes of the BRDFs changed with the slope and aspect effects. For steep slopes ($>30^\circ$), the shape of the BRDF became quite distorted and there was distinct variation in the albedo values. Woodcock *et al.* (1997) found improved results between measured coverage parameters and those estimated by inversion of the Li and Strahler (1985) model when terrain effects were included in the analysis.

Gemmell (1998) carries out a sensitivity analysis of stand reflectance to slope and aspect and attempts to provide a quantified estimate of errors that would potentially occur if the effects of slope were neglected in the inversion process. It was found that, by neglecting slope in the inversion process, significant errors occurred in the retrieved values of forest coverage. Inversion was tested using real Landsat TM reflectance data from a mountainous site in British Columbia, with a digital terrain model (DTM), forest attribute data, and the 6S atmosphere code. The results indicate that the effects of sloping terrain would preclude the retrieval of forest coverage unless terrain effects were specifically included in the inversion process.

2.4. Chapter Summary

In the preceding pages I have attempted to provide the reader with the minimum background on the theory and research directions pertinent to this modeling experiment. In the first section, bidirectional reflectance theory was presented, BRDF defined, and the shape of BRDF curves explained in relation to various vegetated canopy types. In the second section, three forest BR measurement campaigns were detailed. Modeling research, which attempts to bridge the gap between modeling and measurement was examined in the final section. The forest BR modeling section focused on the development and testing of the Li and Strahler (1985; 1986; 1992) model. The challenges associated with terrain effects on modeling were also discussed.

3. Methods

3.1. Introduction & Study Area

This chapter begins with a review of the study area's geographic, biotic, climatic and anthropogenic characteristics. Following this, the methods of the AVIRIS BR experiment and the MEIS II BR experiment are documented in detail. Two diagrams (Figure 3-1 & 3-2) provide both an illustration of the flow of the experiments and a reference guide for locating methodological documentation regarding site selection, field data collection, remotely sensed data analysis, model building and interpretation.

The study area is located at 48° 35' N, 123° 43' W, 40 km north-west of Victoria, Canada within the (Provincial) Capital Region District water supply area (hereafter referred to as the "Watershed"), north of Sooke Lake (Figure 3-3a&b). Public access is restricted for water quality safety reasons. The terrain is rolling, with flat lowland areas adjacent to Sooke Lake, 100m asl (above sea level), rising over a distance of 2km to ridges of up to 300m asl to the north-west and north. A north-west-south-east trending valley, containing Rithet Creek, bisects the study area.

The patchwork texture of the AVIRIS image in Figure 3-3b gives evidence of the anthropogenic activities in the area. The Sooke Lake area was logged extensively in the early 1890's, with natural regeneration producing commercially viable second growth. Logging continued until a moratorium was introduced in 1991 (Carr *et al.* 1992). The maximum age of the trees in the watershed is approximately 500 years. The clear-cut logging and associated silvaculture management practices (thinning, spacing, road building) have produced landscape level characteristics, such as uniformity in stand age and species, plentiful road access, and the presence of a range of stand ages, that are very conducive to scientific research.

The Watershed was one of three study areas chosen for remotely sensed image acquisition for the System of Experts for Intelligent Data Management (SEIDAM) project (Goodenough 1996; <http://pfc.forestry.ca/~seidam/>). This thesis makes use of two airborne datasets collected in 1994 under the aegis of SEIDAM: two AVIRIS scenes and a MEIS-II image. In addition, SEIDAM ground data provided an essential ingredient to the model building process. Details of these datasets and their use are given in the following pages.

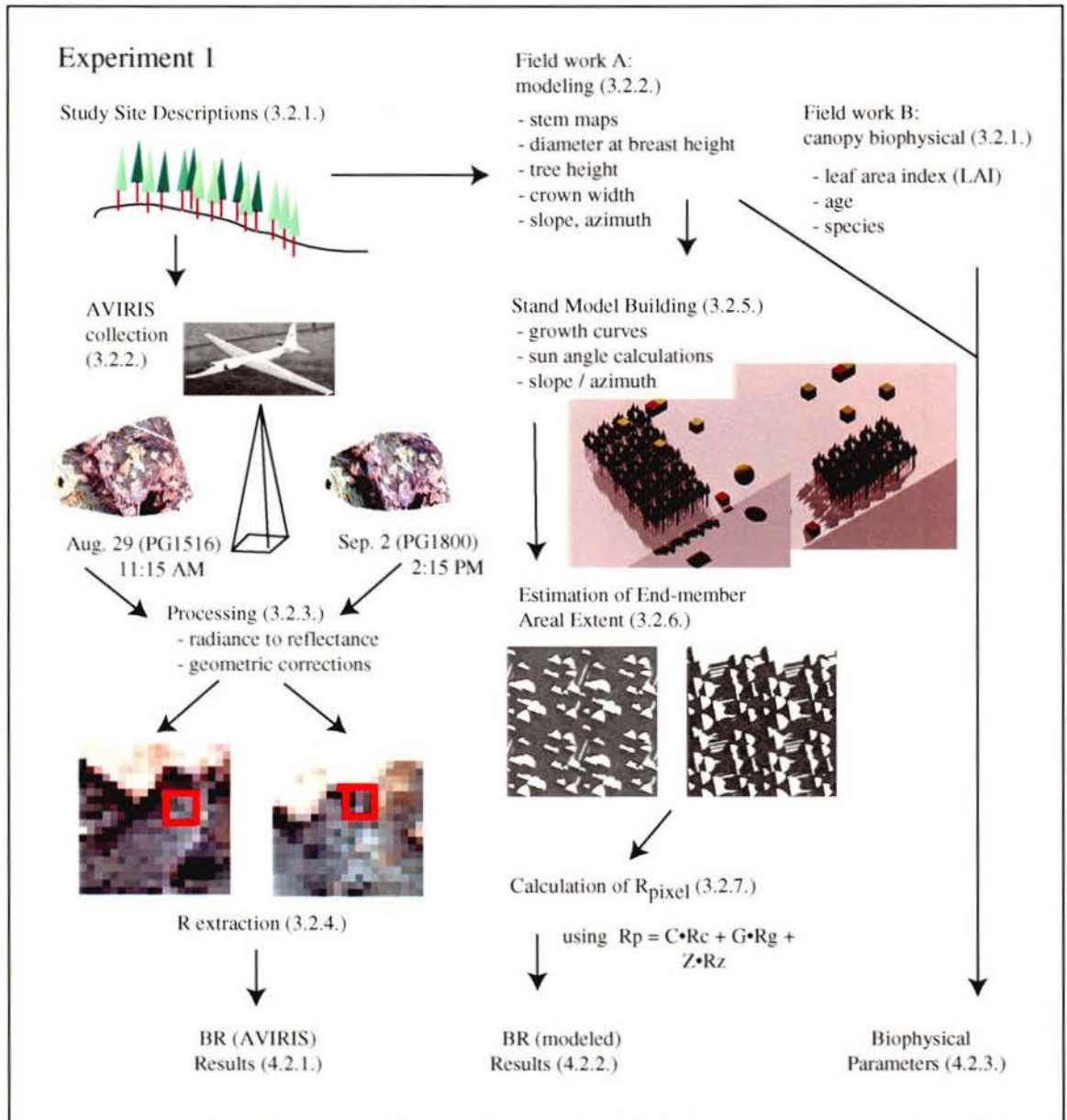


Figure 3-1. Flow diagram of AVIRIS BR experiment.

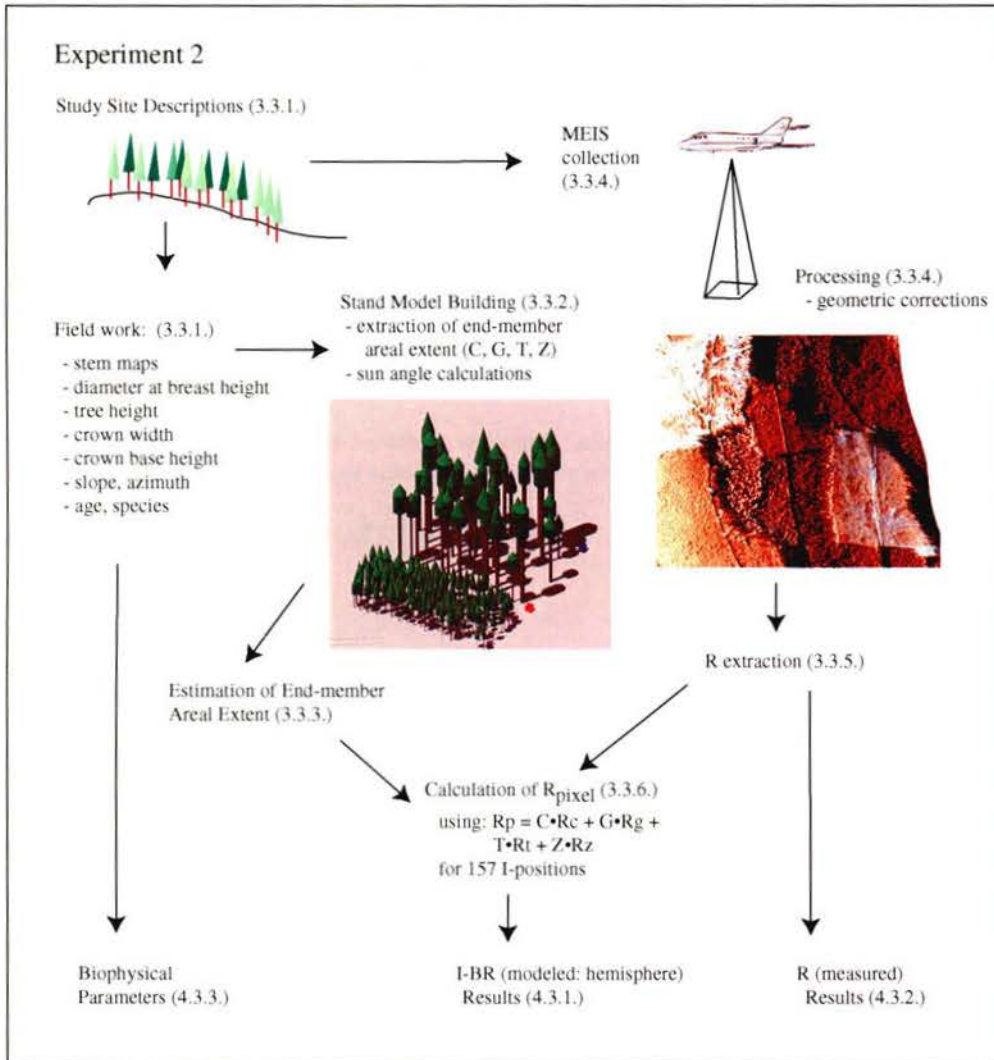


Figure 3-2. Flow diagram of MEIS-II experiment.

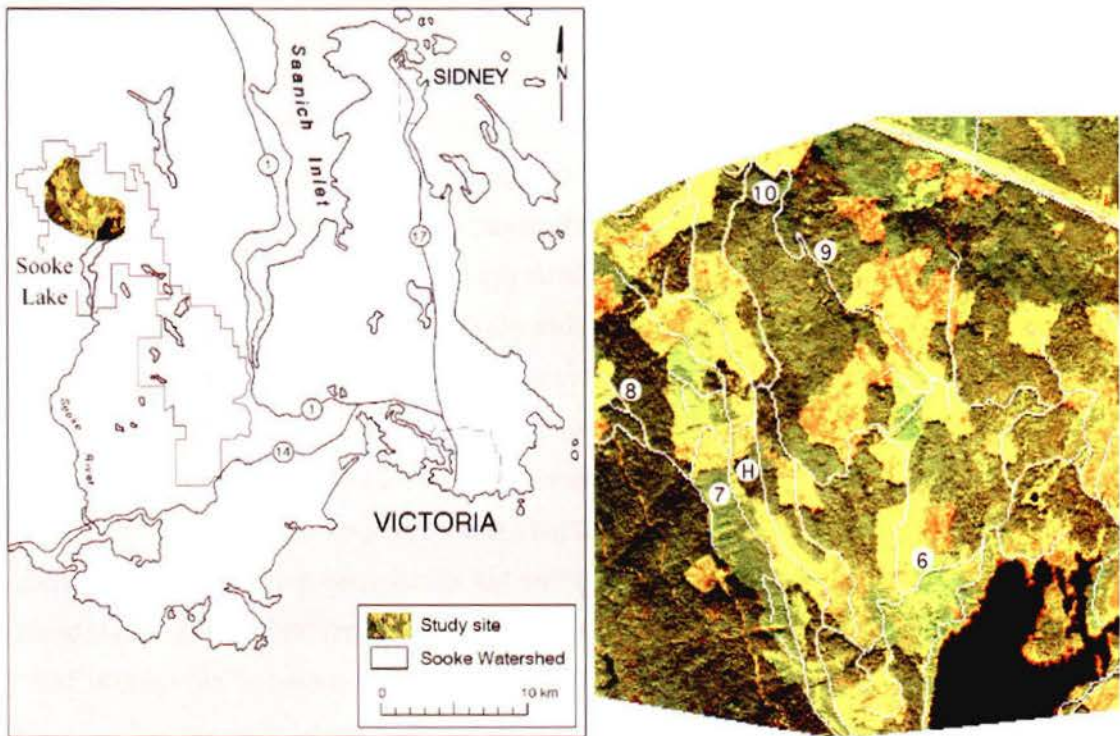


Figure 3-3. Study site locations at Sooke Lake, Vancouver Island. Circles with numbers are AVIRIS experiment sites and the circle with “H” is the MEIS-II experiment site.

3.2. *Experiment 1: AVIRIS Measured and Modeled BR versus Field Data*

3.2.1. Study Site Description

In August of 1993 and 1994, SEIDAM researchers conducted field visits to 10 sites within the watershed. At each site, 20m diameter tree surveys were conducted. For this thesis, five of these study sites were chosen (sites 6, 7, 8, 9, 10). The sites were chosen for their range of stand ages and their location within the coverage of the northern AVIRIS image. The sites encompass a wide range of stand architecture, with stand age ranging from approximately 20 years at site 6 to greater than 140 years at site 10. Additional fieldwork at a mixed-age Douglas-fir stand (named site 11) was carried out to quantify crown architecture relationships. This site was labelled as such for consistency, though no SEIDAM field surveys were conducted there. Site 11 data were used to infer diameter at breast height (DBH) to tree height (H) relationships as described in the stand modeling section (3.2.5).

To build the canopy simulation, both tree geometry and tree location data were required. The SEIDAM field surveys provided stem location (x, y, z) and DBH measurements for all trees greater than 0.2m in diameter. At site 11, crown base height (CBH), crown base width (CBW) and H were collected in addition to stem locations and DBH. Slope and azimuth measurements

were recorded for all sites and checked by comparison to contour data on forest cover maps provided by the Greater Victoria Water District office (GVWD, 1997).

The SEIDAM field surveyors also collected information on species composition and relative foliage density. The latter parameter was deduced from measurements of how quickly the incident radiation is attenuated as it passes through the canopy. The measurements were made using a Licor LAI-2000 Plant Canopy Analyzer (Licor Inc., Lincoln, Nebraska). The LAI-2000 measures the attenuation of diffuse sky radiation at 5 zenith angles simultaneously by projecting the hemispheric view onto 5 detectors arranged in concentric rings. The maximum amount of incident radiation was measured by taking twenty LAI-2000 readings outside of the canopy (usually on an adjacent cut-block) immediately before and after the forty readings within the canopy. One of the assumptions underlying the LAI-2000 methodology is that foliage is randomly distributed both horizontally and azimuthally distributed. Conifer canopies depart from the idea in this regard and require extensive calibration for species and site condition before LAI-2000 readings can be transformed into leaf area index (LAI) estimates. Dr. Hugh Barkley of the Canadian Forest Service is currently conducting destructive sampling to develop a relationship between LAI-2000 measurements and coastal Douglas-fir LAI. The measurements here are thus indicators of relative foliage abundance. The LAI-200 readings and the other biophysical data are presented in tabular form below (Tables 3-1 and 3-2).

Table 3-1. The ages of trees in each site was taken from the CRD Water forest cover map, stem numbers, height and LAI measurements for AVIRIS experiment

site	age (y)	# trees measured	density (trees/ha.)	height range (m)	LAI 2000	LAI-2000 (SE)
6	1-20	18	450	0-10	1.42	0.19
7	20-40	20	500	11-19	3.88	0.08
8	141-250	18	450	29-37	3.36	0.11
9	141-250	27	675	39-46	2.54	0.13
10	141-250	22	550	20-28	3.07	0.29

Table 3-2. Species composition in percent and DBH for AVIRIS experiment sites (DF - Douglas Fir, WRC – Western Red Cedar, WH Western Hemlock).

site	dom. species (%)	0-25cm	25-50	51-75	76-100	>100
6	DF(72) WRC(28)	100%				
7	DF(100)	61%	39%			
8	DF(44) WRC(28) WH(28)	24%	24%	24%	24%	4%
9	DF(63) WRC(37)	51%	40%	9%		
10	DF(91) WRC(9)		44%	52%	4%	

The relatively low LAI value recorded at site 9, the site with the highest tree density, is probably due to a inconsistency between the 20m² area used to survey the site and the larger area used to obtain a statistically significant number of LAI-2000 measurements. The site contained a high tree density, but many of these stems were suppressed having little foliage. In addition, in the vicinity of the site the tree density varied, demonstrating the complexity and discontinuous nature of these naturally regenerated stands.

3.2.2. AVIRIS data collection

Spectrometer data was collected on August 31 and September 2, 1993 by the Advanced Visible and Infrared Imaging Spectrometer (AVIRIS) sensor aboard a NASA ER-2 aircraft. The GRC of the AVIRIS instrument is 20m when flown on the ER-2 at an altitude of approximately 20km. The instrument operates in the 400-2450nm spectral region collecting 210 unique channels with a nominal spectral bandwidth of 10nm (Farrand *et al.* 1994). The spectral range and resolution of the four spectrometers are shown in Table 3-3 and the AVIRIS flight specifications in Table 3-4. Appendix C provides a synopsis of the AVIRIS instrument specifications.

Meteorological data was collected at the Environment Canada weather station at Victoria International Airport, 10 km east of the Watershed, on the same days that remotely sensed data were collected. Weather information was collected at the site and an aerosonde launched to collect atmospheric composition data. Clear skies, with some scattered high cloud, characterized both days. On August 29 there was 25 km horizontal visibility while there was 30km visibility on September 2. Ground temperature at the time of the flights was 21°C and 23°C respectively.

Table 3-3. AVIRIS sensor specifications by spectrometer. The signal to noise ratio (SNR) relates amount of information content relative to noise content in the recorded digital numbers; a higher SNR ratio is desirable. In the case of remote sensing at optical wavelengths, noise in the surface signal is variation in the measurement of radiance that is not related to radiance leaving the target (Landgrebe and Malaret 1986).

<i>Spectrometer</i>	Spectral Range (nm)	Sampling Interval (nm)	SNR
A	396.9 - 702.7	9.6 - 10.1	150:1
B	674.7 - 1283	8.8 - 9.2	140:1
C	1244 - 1867	9.7 - 10.0	70:1
D	1830 - 2454	9.9 - 11.5	30:1

Table 3-4. AVIRIS flight specifications for the two passes used in this study.

<i>Flight Data</i>	Pass 1	Pass 2
Flight Number	930829C run 03	930902A run 05
Date	August 29, 1993	September 02, 1993
GMT start/ end	19:12:36 / 19:15:15	22:11:18 / 22:23:41
Latitude (ϕ) start/end	48:23:41 / 48:40:29 N	48:23:31 / 48:39:30 N
Longitude start/end	-123:39:04 / -123:44:40	-123:39:04 / -123:44:00

3.2.3. AVIRIS Processing

AVIRIS data processing occurred in three phases. First, data were radiometrically, spectrally, and geometrically corrected for sensor effects (Chrien *et al.* 1990) at the NASA Jet Propulsion Laboratory AVIRIS facility. Second, AVIRIS radiance values were converted to reflectance by removal of the atmospheric effects using the MODTRAN-II atmospheric correction program. MODTRAN-II accepts as inputs surface radiance measurements, atmospheric optical depth (aerosonde) data, and field calibration data in the form of measurements taken with a hand-held spectrometer. For this study, the MODTRAN-II model was tuned to a single ground target measurement for which spectral measurements had been made. The differences between the atmospherically corrected (post-MODTRAN-II) AVIRIS data and the ground measurements were used to create a forced-fit function which served to fine tune the imagery for residual atmospheric effects. The results showed an agreement between the corrected AVIRIS data and the MODTRAN-II model of better than 1%, indicating that the default mid-latitude summer MODTRAN-II template was appropriate (Goodenough *et al.* 1996).

The last step before the reflectance data comparison was registration of the two images to known geographic map coordinates. First, the raw August 29 image (Figure 3-4) was registered to Terrain Resource Information Management (TRIM) road network

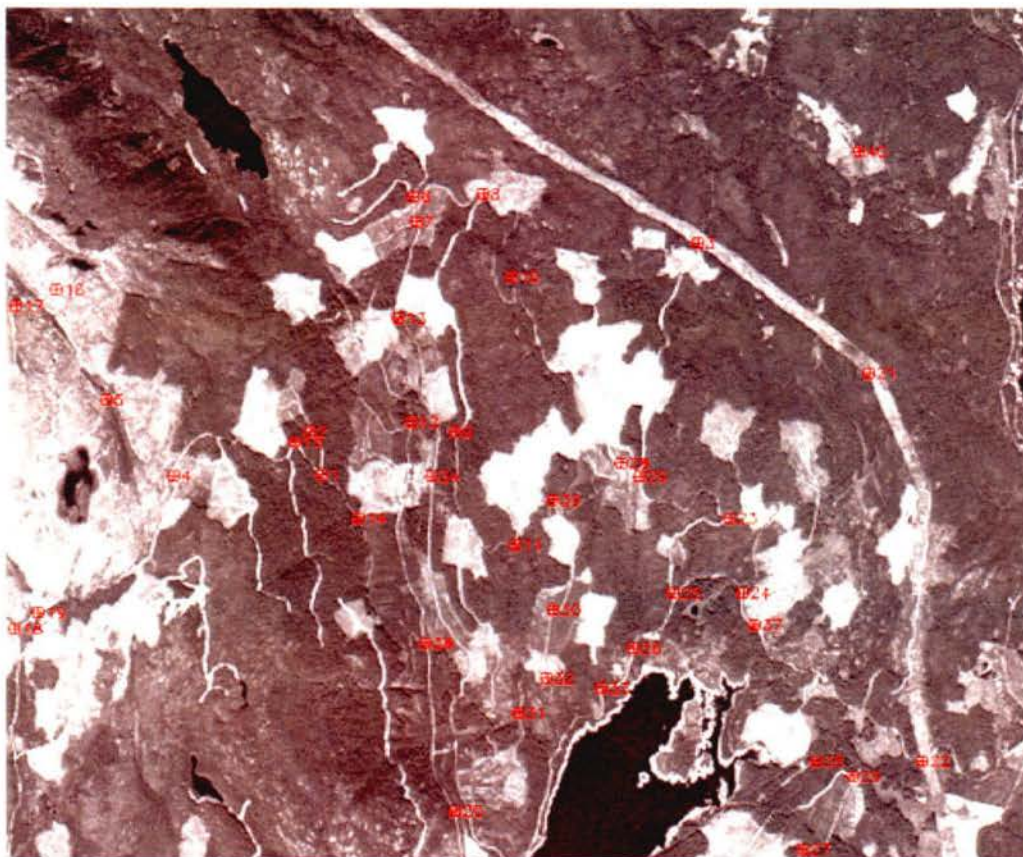


Figure 3-4. Band 36 of August 29 AVIRIS image, radiometrically corrected using MODTRAN-II and before for geometric correction (shown with ground control points (GCPs) at road intersections)

vectors (produced by British Columbia Ministry of Environment Lands and Parks from stereo aerial photographs). TRIM data has a horizontal accuracy of $\pm 10\text{m}$. As there is not a standard procedure for the geo-referencing of AVIRIS imagery, these different registration options were explored: linear, bilinear and Delaunay triangulation. Nearest neighbour resampling is common to all three methods and was chosen to minimize manipulation of reflectance values. The Delaunay triangulation warp was deemed the best warping method based on a visual assessment of the image and the TRIM road network. However, substantial areas of the image were lost due to lack of ground control points in those regions (see Figures 3-5 and 3-6). Delaunay triangulation sets up a network of non-overlapping triangles based on the control points. Without control points in the far regions, image data could not be accurately positioned and was therefore dropped. This loss was deemed inconsequential, as all test sites were well within the registered area. The registration process was carried out using ENVI™ (Research Systems, Inc. Boulder Colorado, at <http://www.rsinc.com>) image processing software.

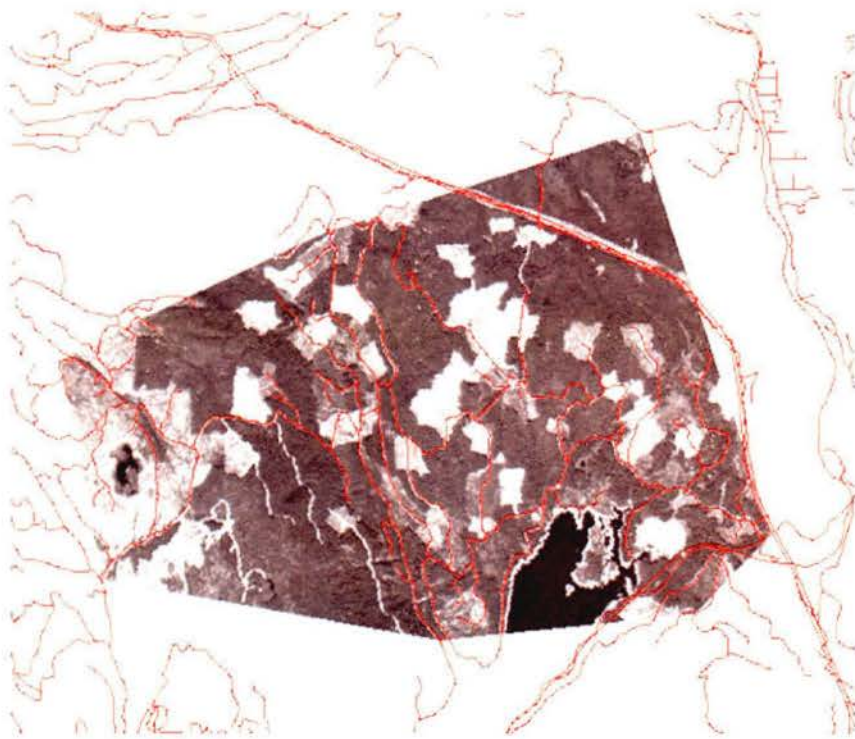


Figure 3-5. August 29 AVIRIS band 36 with Delaunay triangulation warp and nearest neighbour resampling (with TRIM road vectors & GCP tie points).

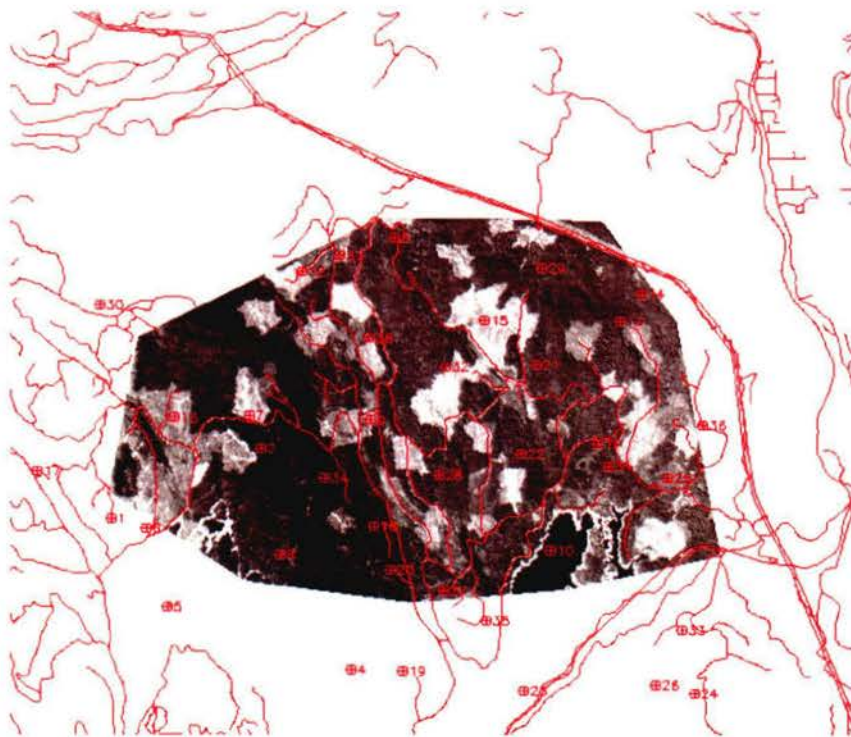


Figure 3-6. September 02 AVIRIS band 36 image with Delaunay triangulation warp and nearest neighbour resampling (with TRIM road vectors & GCP tie points)

3.2.4. ΔR (reflectance) extraction form AVIRIS images

The five study sites were located on the TRIM geo-corrected images using Global Positioning System (GPS)-derived UTM coordinates and from visual matching of the road networks on 1:15,000 aerial photographs and the AVIRIS imagery. At each site, a 3x3 group of pixels taken to be representative of the stand was identified and reflectance data (designated R_{829} for imagery from Aug. 29th) extracted and averaged. The same procedure was followed to extract reflectance data from the second date imagery (designated R_{902} for imagery from Sept. 2nd). Reflectance change was then calculated using:

$$\Delta R = R_{902} - R_{829} \quad \text{Equation 2}$$

Normalized reflectance values were also calculated and their change analyzed. For this, reflectance values were normalized to a pseudo-invariant feature (deep water), according to Equation 3:

$$\Delta R = (R_{902} - R_{902\text{water}}) - (R_{829} - R_{829\text{water}}) \quad \text{Equation 3}$$

3.2.5. Stand model building

The simulated canopy was rendered (built from scene object information and illumination and sensor position geometry) using a ray tracing program (POV-Ray). The scene description file that POV-Ray interprets contains the following scene description blocks:

- A. sensor location;
- B. illumination source position;
- C. tree positions and shapes; and
- D. slope and aspect.

The key procedures and assumptions for making these scene description files are discussed below. A documented listing of the Site 10 POV-Ray scene description file is contained in Appendix E.

A. Sensor Location

The virtual camera ('camera' hereafter) was positioned above the virtual canopy directly above the scene. Two camera projections were experimented with over the course of this research. In an earlier modeling effort (Burnett *et al.* 1996), a perspective projection was used which produced output similar to that of a classic pinhole camera. Light rays radiating towards the centre of the image plane caused scene objects on the periphery to be viewed as if at a higher camera zenith angle than objects in the centre. This is demonstrated in Figure 3-7, where trees on the edge are not viewed from nadir: note how one cannot see the sunlit portion of the tree crowns

in the bottom of the image. The perspective projection camera elicits BR effects associated with the wider swath widths of some sensors (e.g. the NOAA Advanced Very High Resolution Radiometer [AVHRR]), but does not accurately model the instrument characteristics of the 20km altitude AVIRIS sensor. Consequently, an orthographic projection camera was adopted in the final implementations of the model. The orthographic projection camera uses parallel camera rays to create an image of the scene where the camera looks from the nadir position at every part of the scene. Figure 3-10 is an example of a ray-traced scene using an orthographic camera.

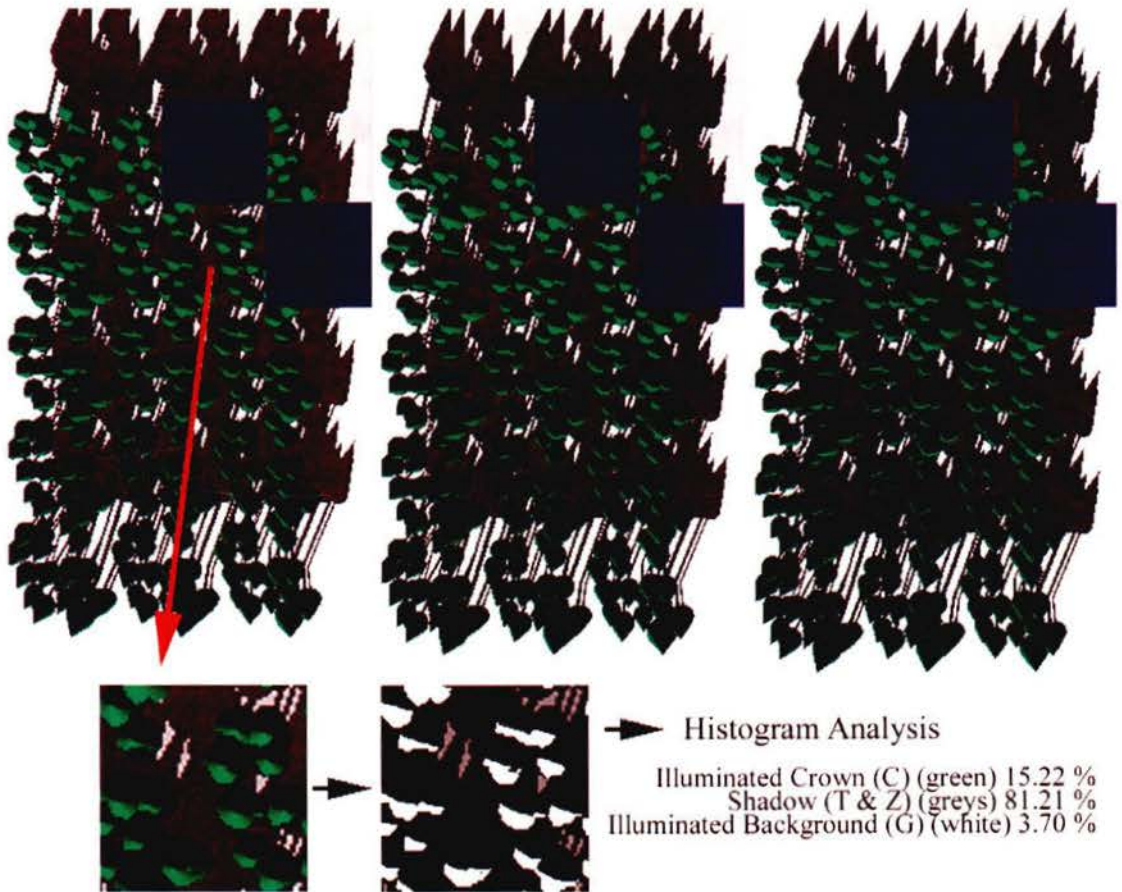


Figure 3-7. Modeled site 10 stand, using perspective camera (note change in area sampled by moving the guide blue boxes); the bottom row shows an example of the mode change to grey-scale and histogram analysis to calculate areal portions.

B. Illumination source position

An important factor concerning the illumination source position was that it be distant from the scene objects so that light rays were approximately parallel, and in so doing, approximate the Sun's rays. Consequently, the illumination source distance was set an arbitrary 10,000m above the virtual canopy. Use of 10,000m produces an angle difference of 0.11° from nadir to the edge of the 20m plot. I could have set the sun to a correct (approximate) 93 billion metres (producing an arc of $1.23 \times 10^{-8}^\circ$ across the plot, but deemed the 0.11° arc to be sufficiently small. The illumination source coordinate position was calculated in a two step process:

(1) calculate solar zenith angle (SZA) and azimuth angle (SAA) from flight time, date and position data using spherical geometry; and,

(2) translate SZA and SAA into model coordinates (x, y, z) using trigonometry.

Celestial objects, like the sun, are recorded in astronomical reference guides such as the *Astronomical Almanac* using the equatorial coordinate system. This coordinate system refers the position of celestial objects to the plane of the Earth's equator. However, the positions of the illumination (sun) and camera positions used to model terrestrial surfaces utilize a horizon coordinate system. In order for the models accurately portray the solar positions for the two AVIRIS passes, it was necessary to convert the equatorial coordinate-based AVIRIS reference data found in Table 3-4 to horizon coordinates found in Table 3-5. A detailed account of these calculations can be found in the Appendix D.

Table 3-5. Solar position data (Altitude = 90 – SZA)

Solar Position Relative to the study sites		
Flight # (Date)	PG1516 (930829)	PG1800 (930902)
Altitude ($^\circ$ above horizon)	48.70	41.09
Azimuth ($^\circ$, south= 180°)	156.27	224.51

The calculated solar angle values were verified by comparison to a computer program called Planet C 6.2 (see Appendix D). The second step in this process was to translate the solar position information in SAA and SZA format into the x, y and z Cartesian coordinates used in the ray-tracing program, using the Pythagorean theorem.

The final consideration with regard to illumination was whether to program an ambient light source. Ambient light plays an important role in illuminating areas within shadow. Since the model used in this study did not differentiate between levels of shadow, no ambient light source was programmed. Emphasis was instead given to creating "hard" edges for the estimation of the areal extent of the model variables (C, T, G, and Z).

C. Tree positions and shapes

Tree x, y and z positions were extracted from the 20m diameter stem survey data. Because the height of the trees in the sites and the low solar azimuth angles at the time of the AVIRIS flights, shadows were cast that exceeded the survey extent. Thus, the simulation required information about tree distributions to the sun-ward of the modeled site. For example, at one sloping site, tree distribution data up to seven times the size of the 20m diameter plots was necessary to ensure that the proper amount of shadow was incorporated into the analysis. A solution to this problem, relying on an interpolation from existing data, was adopted.

Building the simulated stand through interpolation of the field data may be approached using a spatial arrangement model or through a template method. In the spatial arrangement modeling method, tree density, spacing and size distributions are extracted from the field data and a set of virtual trees generated as required based on this information. Because of the small (20m^2) size of the SEIDAM surveys, this procedure was considered impractical. Instead, a “template” method was used wherein 20m^2 of the surveyed tree positions and sizes were sampled, and this template was then replicated at 20m intervals to form a larger virtual stand in whichever direction was necessary. Artefacts of this method are repetitive patterns within the virtual canopy (see, for example, Figure 3-7). To avoid this, offset placement of the templates was used. In addition, samples were taken from three sub-areas within the 20m^2 modeled stand.

A number of steps were required to translate the survey data into the site-specific tree templates. First, stem locations had to be changed from UTM coordinates to coordinates in a Cartesian system. Then, DBH was used to estimate H based on a DBH/H relationship extracted through regression from a plot of 30 trees in the 40m^2 site 11 (*cf.*, Flewelling, 1994; Avery and Berlin, 1992). This DBH/H relationship was modified for each site. For each site, height ranges were drawn from the CRD Water forest cover map. Then, each tree’s DBH was mapped to an H within the range according to the site 11 DBH/H log relationship. Table 3-6 shows the mechanistic equations used to place each tree within the height and CR range for each site using the tree DBH.

Table 3-6. Site-specific tree model equations derived from relationships between tree height and DBH on a range of tree sizes in Plot 11. H equation coefficients place the tree inside the range found on the forest cover map.

Site	H Range (m) (forest cover map)	H (m) tree height	CR (m) crown radius	CH (m) crown height	CBH (m) height to base of crown
6	0-10m	6.391*LOG (DBH)	-2.1043 + (2.5141 * LOG (DBH))	H/3	CBH = 2 * H/3
7	11-19m	11.391*LOG (DBH)	-2.1043 + (2.5141 * LOG (DBH))	H/3	CBH = 2 * H/3
8	29-38m	7.751+13.391*L OG (DBH)	-2.1043 + (2.5141 * LOG (DBH))	H/3	CBH = 2 * H/3
9	39-46m	20.751+13.391* LOG (DBH)	-2.1043 + (2.5141 * LOG (DBH))	H/3	CBH = 2 * H/3
10	20-28m	1.751+13.391*L OG (DBH)	-2.1043 + (2.5141 * LOG (DBH))	H/3	CBH = 2 * H/3

Once tree height was estimated, crown base height (CBH) was calculated by the simple approximation described in Table 3-6 using the relationship specific to that site. This approximation was based on measurements taken from visits to sites 8, 9, 10 and 11.

Finally, crown base diameter (CBD) was estimated. Again, a relationship based on samples from the 30 tree, mixed age Douglas-fir site (Site 11) was used, and the equations generated (unique to each site) can be found in Table 3-6. Once DBH, age, and species had been translated into H, DBH, CBH and CBD, a virtual tree could be built at the x, y, z location as surveyed during the SEIDAM field visits. Each modeled tree consisted of a cone (crown) and a cylinder (stem) which was coded in POV-Ray description language:

```
TREE a
    //stem
    object { cone { 15*y, 0.27, 0.0, 0.27
// make a cone with top and base radius
equal to 0.27m (i.e. a cylinder) //
    translate < -10, 0, -10 > }
// move to x, y, z //
    pigment {colour Brown}}
// colour the stem brown //

    //crown
    object { cone { 15*y, 0.0, 0.0, 2.2
// make a cone 15m tall, radius 0 at top,
2.2m at base //
    translate < -10, 15, -10 > }
// move above stem //
    pigment {colour Green}}
// change colour to green //
```

The output from this code can be seen in Figure 3-8a.

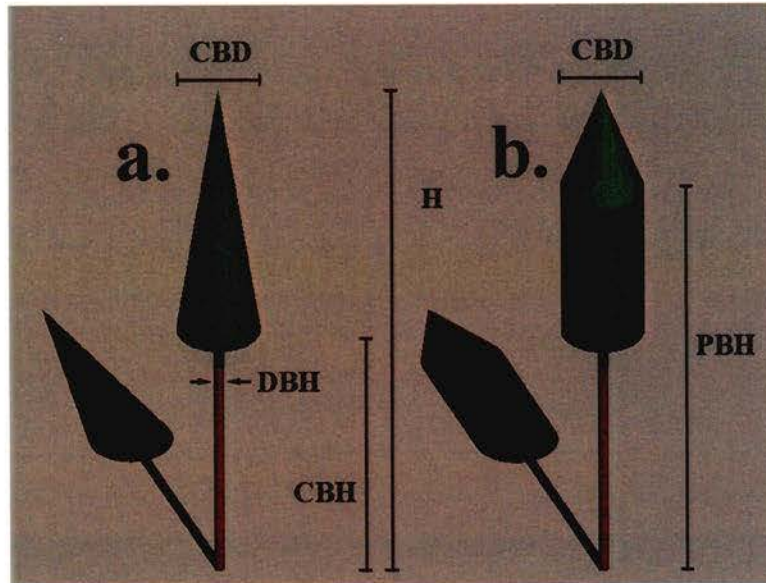


Figure 3-8. Tree parameters collected in field visits or interpolated from field survey and displayed using example output from POV-Ray ray-tracing program

D. Slope and aspect

The last section of the scene description file required the inclusion of a plane that corresponded to the slope and aspect found at the site. The earliest runs of this experiment (Burnett *et al.* 1996) did not use a slope component, which resulted in large discrepancies between modeled reflectance changes and the AVIRIS measurements. When the range of topographic situations was considered, it became obvious that slope and aspect must be incorporated and so a vector (normal to the real slope) was added to the code describing the background plane in the virtual canopy scene:

```
plane {
    <0, 0.878, -0.479> , -0
    // vector normal to plane: for site 10, 15° slope,
    // 245° azimuth, and transpose (-0) to origin //
    pigment {colour rgb <1.0, 1.0, 1.0> }
    // colour = white //
```

An added challenge was to get each tree position translated to a new on-slope coordinate. This process was accelerated by the use of a spreadsheet program. The descriptor file for site 10 (1st sun position) found in Appendix E shows the text file that POV-Ray interprets to render the image found in Figure 3-9. In the next section, the component areal calculation is detailed. Note that the calculation was completed twice, once with the slope information omitted and then a second time with slope and aspect added to the model.

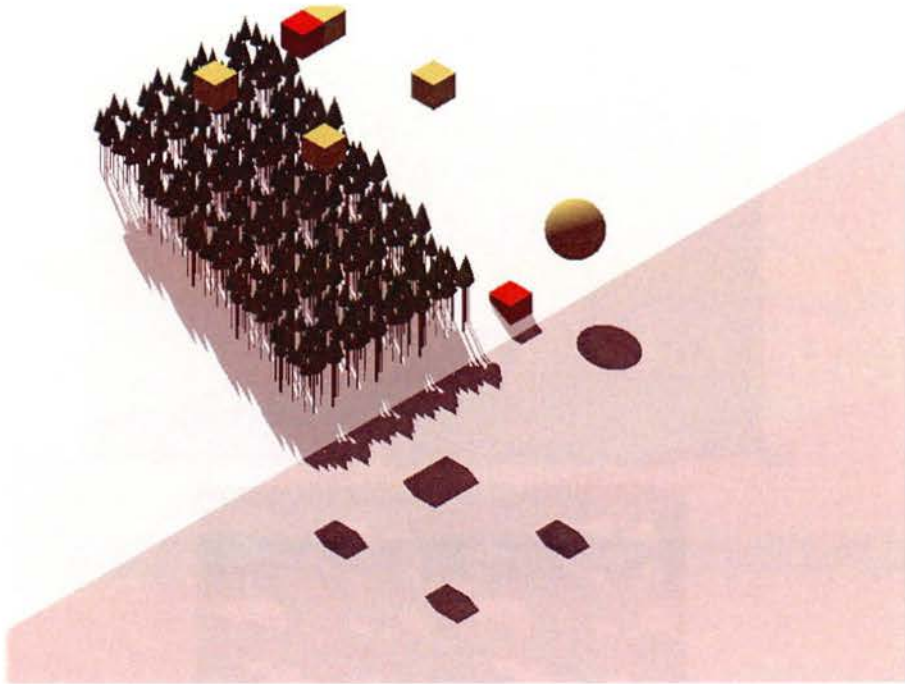


Figure 3-9. Demonstration of the incorporation of slope and aspect into model: an oblique view of site 10, modeled using POV-Ray

3.2.6. Estimation of component areal extent

Once each site was translated into POV-Ray descriptor code, the extraction of component areal extent estimates could begin. Three randomly placed samples were taken and the mean of the three samples used to represent the larger canopy model. These samples were acquired by moving a 20m² frame above the canopy. The frame was built using four cubes that can be seen to “float” over the canopy in Figure 3-9. The cubes can also be seen as blue boxes in Figure 3-7. Areal extents of sunlit canopy, sunlit ground, shadowed canopy and shadowed ground were then extracted from within the area subtended by the framing cubes, as shown in Figure 3-7 and Figure 3-10. Figure 3-10a shows nadir viewed canopy and Figure 3-10b shows the extracted subset region in grey-scale mode. This was the image that was examined using Adobe Photoshop™ (www.adobe.com) image analysis software.

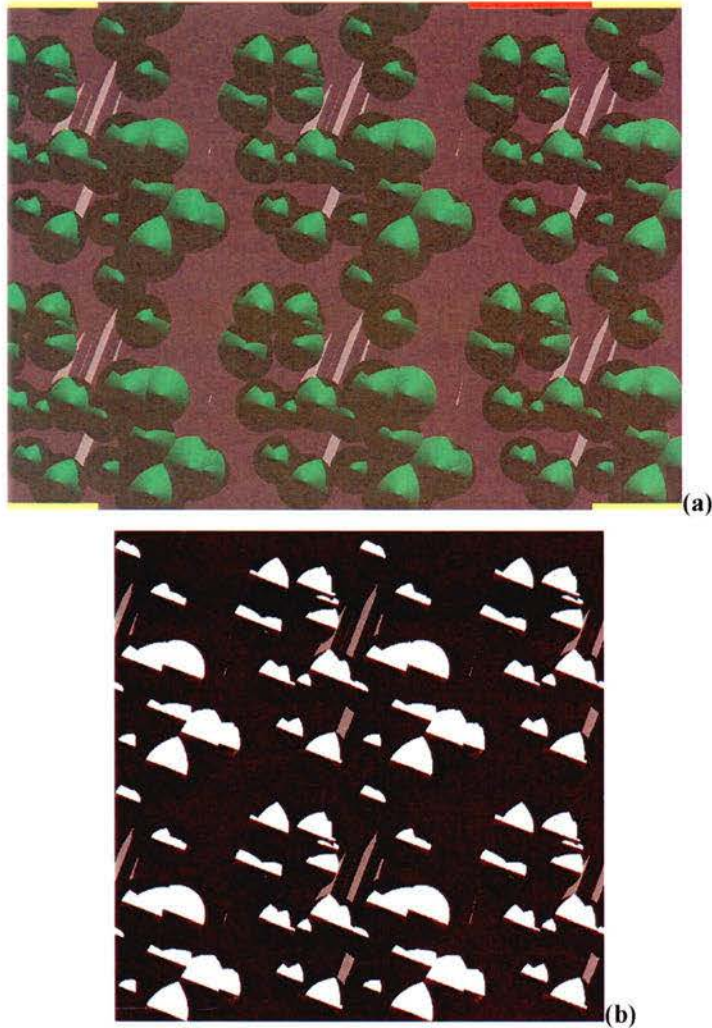


Figure 3-10. Nadir view of (a) modeled Site 10 stand and (b) cropped and classified area used to calculate component proportions. Note the three grey levels: dark grey and black are shadow, light grey is sunlit background and white is sunlit crown.

3.2.7. Calculation of R_{pixel}

The equation and values used to calculate the reflectance of a single composite AVIRIS pixel based on the reflectances of its components and their areal proportions used by Li and Strahler (1992) are applied in this experiment. Using the following equation:

$$R_{\text{pixel}} = C \cdot R_c + G \cdot R_g + S \cdot R_s, \quad \text{Equation 4}$$

Values for R_c , R_g , and R_s of 0.3, 0.7, and 0.0 respectively were input. The use of reflectance spectra taken from the literature is not uncommon. Gemmell (1998) used conifer crown reflectances taken from Cavayas and Teillet (1985) and a sunlit ground reflectance value from Rosema *et al.* (1992) as inputs into the Li and Strahler model. The use of 0.0 for R_s is probably the weakest assumption, since zero reflectance is improbable in most wavelengths, except,

perhaps in the near-infrared. This highlights the difficulties in using literature-based constants for studies where the requirements are different (i.e. use of hyper spectral data).

3.3. *Experiment 2: MEIS-II BR and Modeled BR versus Field Data*

3.3.1. Study site descriptions

The study sites used by Hay and Niemann (1994) along Rithet Creek were ideal for a comparison between measured and modeled radiance as a function of solar angle since they were topographically level and a detailed survey dataset was available for each stand. An “H” in Figure 3-1 marks the study sites. The oblique aerial photograph in Figure 3-11 shows Sooke Lake at the south end of the Rithet Valley. The point of the yellow arrow marks the Experiment 2 location, with the immature stand north of (below) the mature stand. The stands are known collectively as the ‘Haysite,’ after Geoff Hay who first established the plots and whose survey data is used extensively in the analysis.



Figure 3-11. Oblique photograph looking south at the Experiment 2 site location (below yellow arrowhead) with Sooke Lake in background

The immature stand, planted in 1965 and spaced in 1975, is composed predominantly of Douglas-fir (*Pseudotsuga menziesii*) with some Western Hemlock (*Tsuga heterophylla*). Tree height ranged from 11m to 25m. The mature stand contains trees ranging in age from 140 to 250 years and in height from 20m to 70m. The Hay and Niemann (1994) fieldwork provided H, CBD, DBH, and x, y coordinates for each tree within the plot. Additional site visits were required to derive an approximation of the CBH to H relationship. Measurements were obtained from 20 trees using an Abney level and fibreglass tape (Kesser 1970).

3.3.2. Stand model building

Tree mensuration data (Hay and Niemann 1994) were translated into POV-Ray scene descriptor language in a manner similar to that employed in the AVIRIS BR experiment. There were some necessary differences in the form of this translation since CBD and H were known and did not have to be interpolated from forest cover map and growth curve data. Additionally, the model tree geometry was changed to resemble real tree envelopes by shaping the trees as shown in Figure 3-8b. The tree shown in Figure 3-8b was rendered using the POV-Ray scene code shown below:

```
TREE b
//stem
    object { cone { 15*y, 0.27, 0.0, 0.27
// make a cone with top and base radius
equal to 0.27m (i.e. a cylinder) //
    translate < 10 , 0, -10> }
// move to x, y, z //
    pigment {colour Brown}}
// colour the stem brown //
//body
    object { cone { 9*y, 2.2, 0.0, 2.2
// make a cone with top and base radius
equal to 2.2m (i.e. a cylinder)
    translate < 10, 15, -10> }
// move above stem //
    pigment {colour Green}}
// change colour to green //
//crown
    object { cone { 6*y, 0.0, 0.0, 2.2
// make a cone 6m tall, radius
0 at top, 2.2m a base //
    translate < 10 ,24, -10> }
// move above body //
    pigment {colour Green}}
// change colour to green //
```

CBH was calculated using a simple approximation of $CBH = 0.33 * TH$. This approximation is consistent with the field measurements of 20 sampled trees at the Haysite.

Once built, each stand was modeled separately, but they are shown together in the following rendered image for the purpose of comparison. Figure 3-13 shows an oblique view of the stands with the virtual camera looking south. The coloured boxes serve to mark the range of each study site (immature & mature stands).

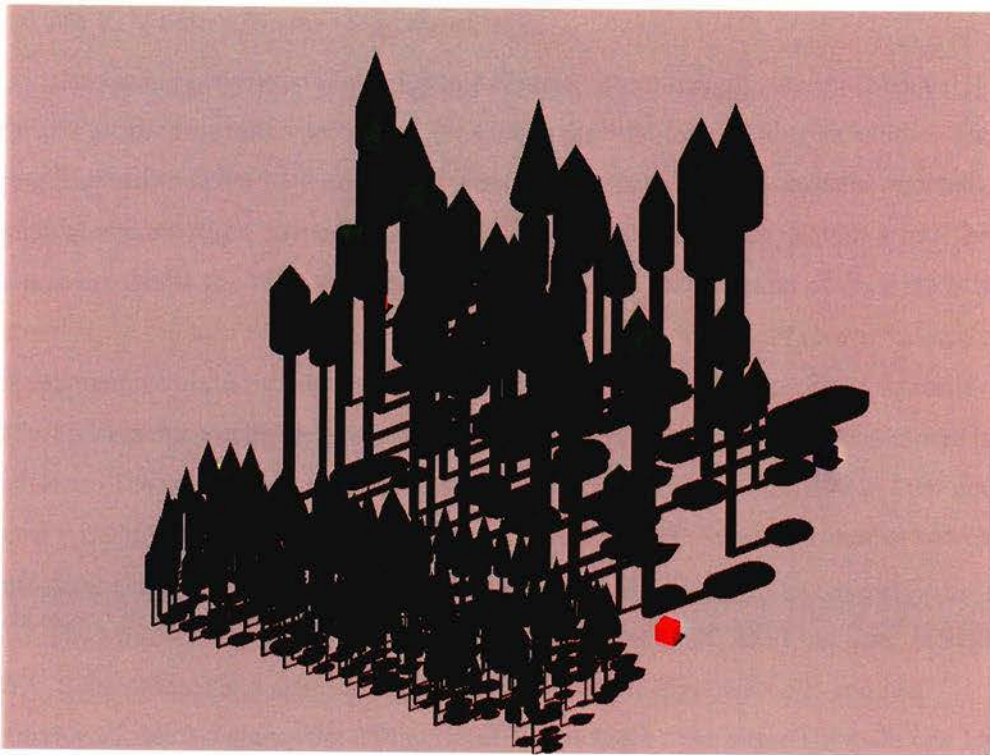


Figure 3-12. Oblique view of modeled MEIS-II experiment immature and mature stands. The coloured boxes are designed to mark the boundaries of the mature stand.

3.3.3. Estimation of component areal extent

As in the AVIRIS experiment, for each illumination position a subset of the larger rendered model is extracted for the purpose of component areal extent analysis. An enlarged 40m^2 area was rendered for the MEIS-II experiment. The change to a 40m^2 area instead of a 20m^2 area was made so that within-stand shadow variation could be captured in one subset, rather than averaged over 3 samples. The sensor position (i.e. virtual camera position) was fixed with a nadir view angle to the centre of the modeled area and was programmed to have an orthographic perspective. Canopy simulations were rendered for 156 illumination angles ($[\text{SZA} = 0^\circ \text{ to } 60^\circ \text{ in } 15^\circ \text{ increments}] \times [12 \text{ SAA}]$) for each of the two sites. Thus, a total of 302 images were rendered and areal extents for C, G, T, and Z extracted. Each image required 40 minutes of rendering time on a 100MHz Macintosh PowerPC computer. Due to the time required for image rendering, this phase of the work required an entire week of nearly continuous computer time.

3.3.4. MEIS II data collection & processing

The second generation Multi-detector Electro-optical Imaging Sensor (MEIS II) (Till *et al.* 1983) is an airborne multispectral imager using a push-broom scanning technique. The imaging component of MEIS-II consists of a multi-element linear array detector oriented perpendicular to the flight direction and located in the focal plane of an imaging lens. The distant scene is focused onto the CCD array, and the response from each element of the array is sampled electronically to produce a line image of the scene below. As the aircraft moves forward a new line is captured, so that a two-dimensional image of the scene is built up. Eight channels of data are recorded and the spectral sensitivity of each is bracketed using spectral filters placed in front of each lens. The spectral response of the sensor (without a filter) is from 390 to 1100 nm. Nadir radiance is recorded in six channels and off-nadir (fore and aft) recorded in another two channels. The off-nadir channels may be used to produce a stereo pair.

The MEIS-II sensor was flown over the study site at 11:30 AM local time on September 2, 1993. Solar altitude and azimuth angles at the time of the flight were 52° and 133° respectively. Table 3-7 shows the 8 filters used for the flight. The aircraft altitude was 1428 m, resulting in a ground resolution cell (GRC) of approximately 1.0m.

Table 3-7. MEIS-II filter specifications (*used in Experiment 2)

Channel	0 (stereo)	1*	2	3*	4 (stereo)	5	6	7
Wavelength	549	641	518	875	549	448	553	675
Orientation	aft- looking	nadir	nadir	nadir	fore- looking	nadir	nadir	nadir

The raw MEIS-II data was geometrically corrected to TRIM planimetric data. Each MEIS II flight line is 8 channels deep, with each channel having a dimension of 7100 samples by 27400 lines (i.e. each a 195 MB file), a memory-intensive dataset with which to work. Accordingly, a smaller image centred on the study site (Figure 3-13) was cropped out of the full sized image.

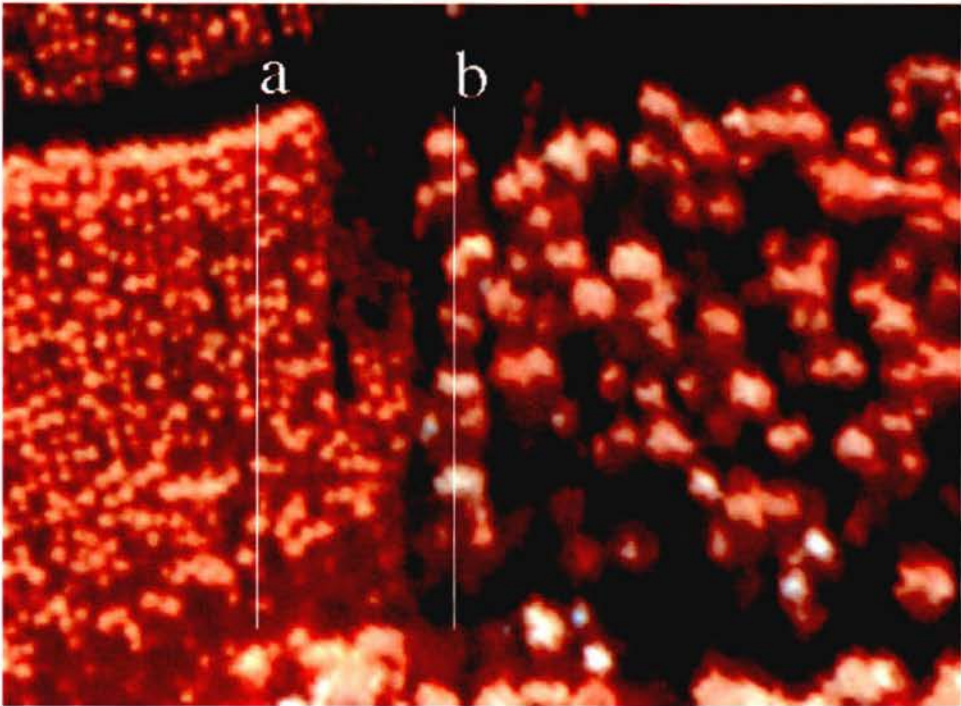


Figure 3-13. An RGB (ch6,ch4,ch3) cropped MEIS-II image of the Haysite stands. North is to the left. Figure shows extraction of R values using transects: a-transect runs through the 40 year old 'immature' stand to the north, while b-transect runs through the 150+ year old 'mature' stand to the south

3.3.5. R (radiance) values for MEIS-II modeling

R value estimates for the MEIS-II experiment model were extracted from the imagery. Though it is potentially hazardous to extract model inputs from the data to which it will be compared (model/reality independence is compromised), this method was deemed to be an improvement over the method used in the AVIRIS experiment, wherein component radiance values were extracted from literature citing work with different species and forest types. Two methods of R estimation were examined, the transect survey and the interpreted sample.

The Transect Survey

Using image processing software, radiance values from two transects were extracted and graphed (Figure 3-14). The transects were placed to cross through the centres of a representative sample of crowns and through several canopy openings. Transect 'b' is not well placed. The radiance values plotted in transect b are probably contaminated by the reflectance from the bright response of the neighbouring immature stand. Additionally, the 'wells' between the trees in transect b will undoubtedly be brighter since the canopy is open to the side, allowing ambient sky

light in. End member radiance values were taken from the transect graph (Figure 3-13) in the following manner (note that R values were different for the immature and mature canopies):

- **R_c**, the sunlit crown values were found by taking the mean of the peaks of the graphs;
- **R_t**, shadowed crown values estimated from the mean of a sample of R values taken from the right shoulders of the radiance peaks. The right shoulder of the peak was estimated to be a measure of the shadowed crown because the right shoulder of the peak is the northern side of the crown. The northern side of the crown is more likely to include several pixels of shadowed tree than the sunlit side of the crown (the left shoulder);
- **R_z**, the widest troughs in the graphs were assumed to be the best location to extract an estimate of R_z, shadowed background;
- **R_g**, sunlit ground (R_g) values are problematic to accurately estimate due to the density of the forest canopies used in the study plots made 'pure' location of sunlit ground scarce. To deal with accuracy problems, R_g values were first extracted from a non-forested area to the east of the site. The assumption was that the dense ground vegetation of the non-forested area (composed of salal and mixed shrubs) should mimic the heavy undergrowth found under the immature and mature plots. Assuming equivalence between R_g and the sunlit clear-cut was a poor methodological choice, and is discussed in the Analysis chapter.

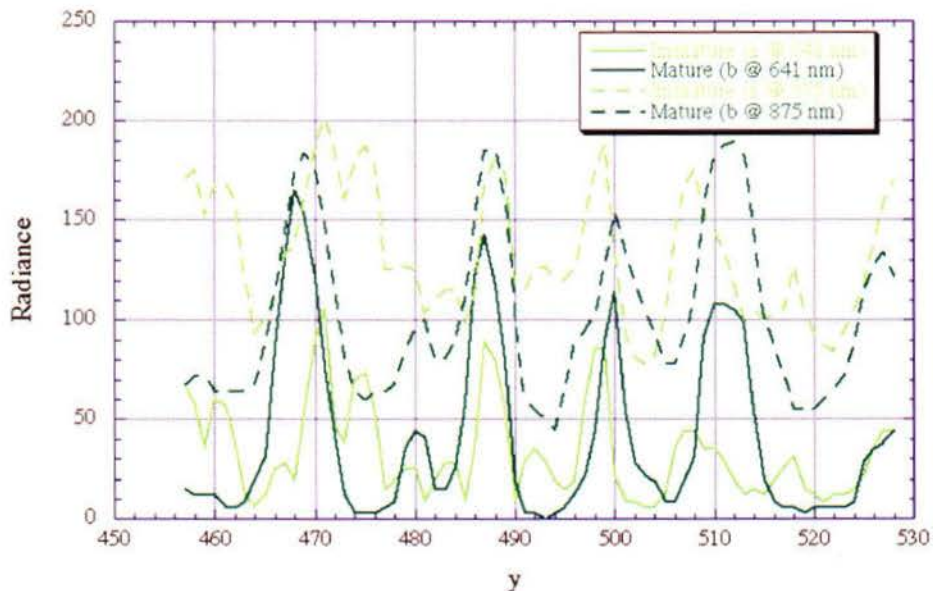


Figure 3-14. Radiance of transects through immature and mature canopies. The y axis describes the number of pixels from the north end of each transect to the south.

The Point Sampling Method

The strength of the Transect Method, mainly that it is relatively objective, is offset by its lack of representation, and so an alternative method was used. The Point Sampling Method relies on the use of in depth site knowledge from field visits, air photographs, and survey data to pinpoint areas in the image where ‘pure’ radiance values could be extracted. Figure 3-15 shows the locations used for the point sampling process.

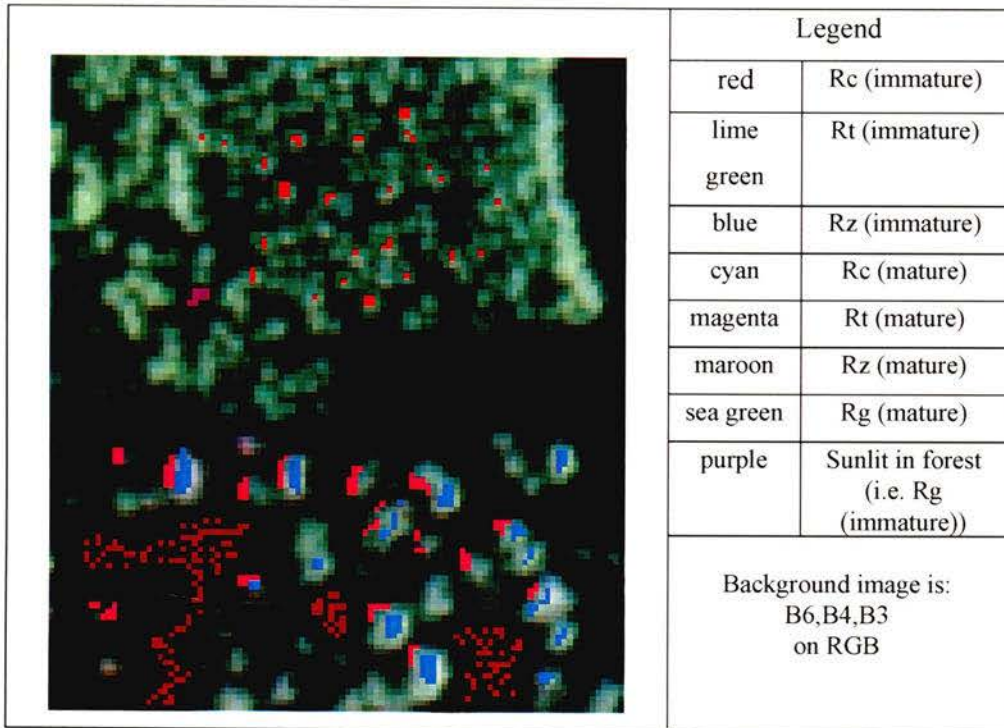


Figure 3-15. Extraction of R component values by point sampling

3.3.6. Calculation of R (pixel)

R_{pixel} was calculated in the same manner as used in AVIRIS experiment except that the shadow component was broken into two parts; T (shadowed crown) and Z (shadowed background). Figure 3-16 shows model renderings (three out of 146 made for each canopy for each) for the generation of a semi-hemispheric BR surface, and a grey scale image showing the resulting areal classification for each end member.

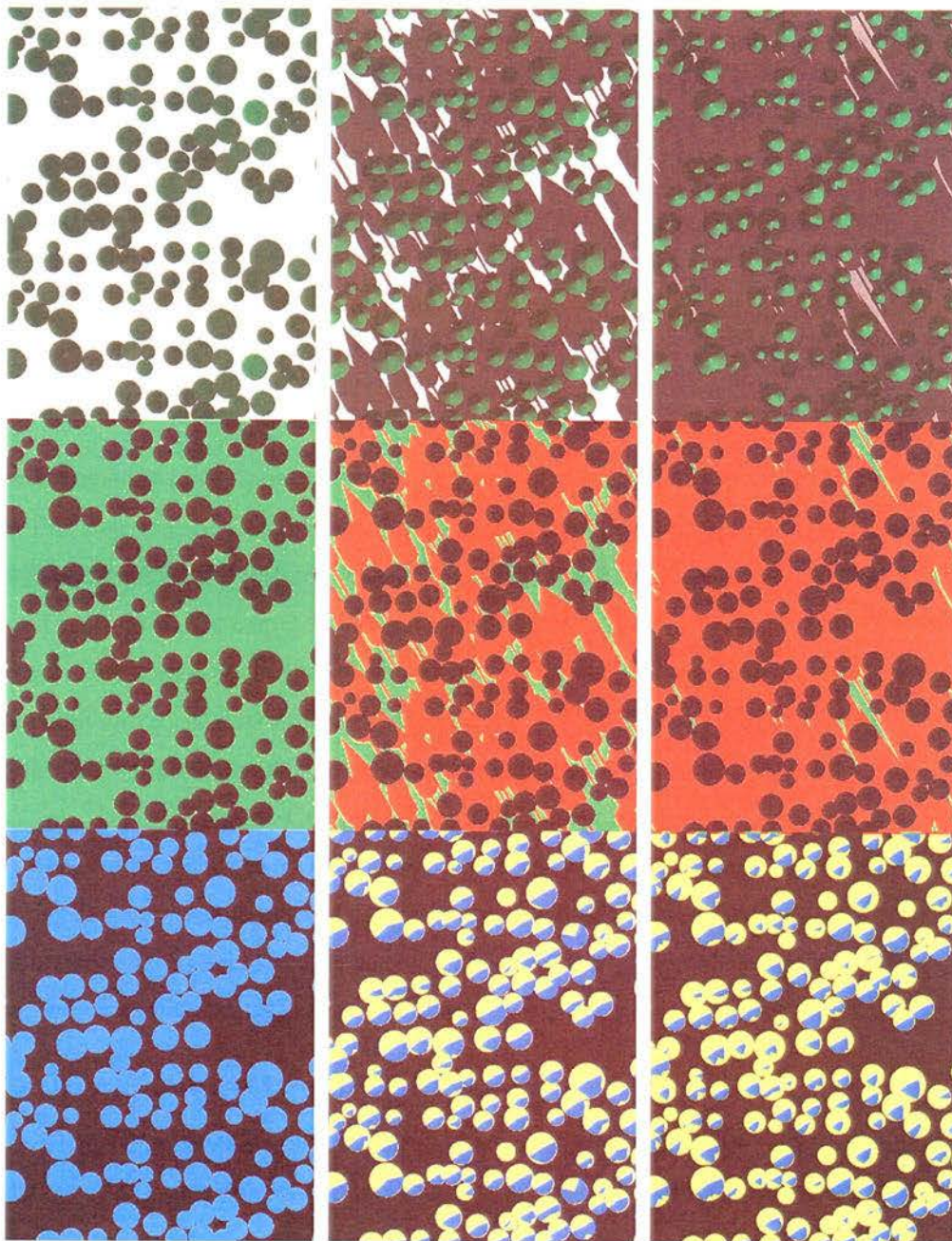


Figure 3-16. Modeling areal proportions for solar azimuth angle (SAA) of 150° with different solar zenith angles (SZA 0° (nadir); SZA 25°; SZA 60°). Central panels show amount of shadow cast by trees (red portion). Lower panels show amount of shadow in the crown (sunlit = blue / shadow = yellow)

Table 3-8. Numerical analysis of areal extents extracted using Photoshop from the modeled stands in Figure 3-16.

Ray-tracing of immature stand: SZA=0° (run 1/13); SAA=150°	Ray-tracing of immature stand: SZA=25° (run 7/13); SAA=150°	Ray-tracing of immature stand: SZA=60° (run 13/13); SAA=150°
Crowns masked out: G = 55.36% Z = 0.64%	Crowns masked out: G = 15.04% Z = 41.69%	Crowns masked out: G = 11.28% Z = 44.72%
Background masked out: C = 43.44% T = 0.56%	Background masked out: C = 27.24% T = 16.03%	Background masked out: C = 10.35% T = 33.65%

The determination of component areal extents using Adobe Photoshop™ is a two stage process. In the first step, the crowns are masked out and the relative proportions of shadowed and unshadowed background (G and Z; Table 3-8, second row) are assessed. Note the rapid change from all sunlit to almost completely shade, which relates to the height and shape of the trees in the scene. Subsequently, the background is masked out and the crowns are assessed for their relative amounts of shadow and non-shadowed area (C and T; Table 3-8, third row). Finally, R_{pixel} for each rendered sun position is calculated using:

$$R_{\text{pixel}} = C \cdot R_c + G \cdot R_g + T \cdot R_t + Z \cdot R_z \quad \text{Equation 5}$$

The values were graphed to produce a semi-hemispheric surface and for the SAA and SZA rendering closest to the position of the sun at the time of the MEIS-II pass, a comparison was made between the modeled and measured radiance. A description of the extraction of R_{pixel} values for each of the stands is described next.

3.3.7. Determination of L-resolution MEIS values

The modeled values used to calculate the semi-hemispheric BR surfaces required some validation. Validation was sought through a comparison between the values generated by the model for each stand (immature and mature) and an L-resolution sample of each stand in the MEIS-II image. L-resolution samples were acquired by taking the mean of the radiance measurements for sample areas of approximately 40m² (Figure 3-17). The use of the simple mean to up-scale the 1m image to 20m² GRC has been shown to provide an adequate up-scaling method, though other up-scaling algorithms are possible (Hay et al. 1994).

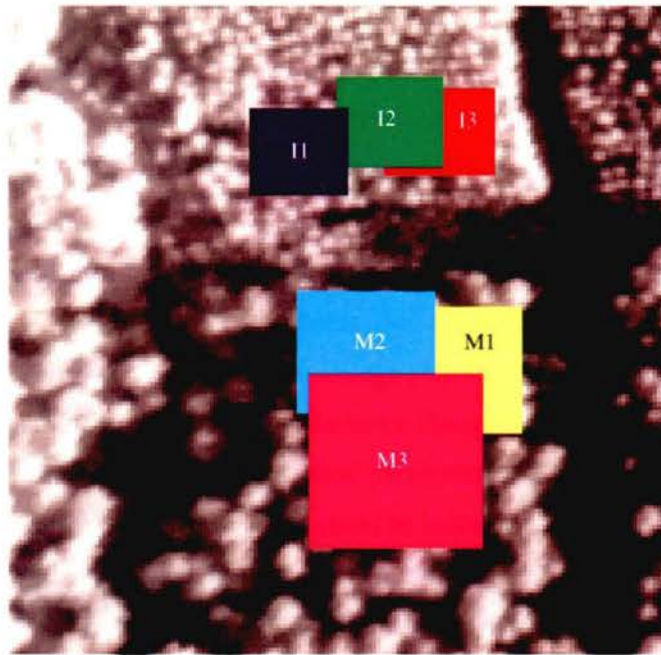


Figure 3-17. L-resolution sample areas in MEIS-II image. I = immature, and M = mature.

3.4. Chapter Summary

Modeling complex systems such as vegetation canopies involves breaking an integrated and continuous natural system into a series of independent and discrete analogues. This chapter provides a detailed description of the steps developed to implement and derive results from one particular canopy type. The research did not follow an instruction set imported from another work, rather, through an extended series of problem/solution steps, the method described in this chapter evolved. The process was sometimes awkward and often time-consuming because no ‘comprehensive’ tools were available.

The chapter also details the similarities and differences between the methods of the two experiments: AVIRIS measures are reflectances while MEIS-II are radiances; in the AVIRIS experiment a three component model is implemented, while in the MEIS-II experiment, the shadow component is broken down further into shadowed crown and shadowed background; in the AVIRIS experiment, two measurements are available (allowing for a true BR comparison) as compared to the one pass MEIS-II experiment; in the AVIRIS experiment, topography played an important and confounding role, whereas the sites for the MEIS-II experiment were relatively flat.

4. Results & Analysis

4.1. Introduction

This chapter follows the format of the Methods chapter; each experiment is presented separately with comparisons *between* the experiments left until the Summary and Conclusions chapter. For each sub-section of each experiment, the results and analysis are coupled. Thus, for the AVIRIS BR experiment (4.2), reflectance change (4.2.1) is presented and then compared, followed by a presentation and analysis of reflectance change versus modeled change (4.2.2), and finally, reflectance change versus site biophysical parameters (4.2.3) are presented and analysed. This structure was adopted so that discussion could be initiated while the pertinent results had the reader's attention. The experiment results which are presented and then analysed in the MEIS II BR experiment (4.3) are: bidirectional radiance hemisphere modeling (4.3.1), $R_{\text{MEIS-II}}$ versus R_{MODEL} (4.3.2), and model re-calibration (R_g / areal) (4.3.3).

4.2. Experiment 1: AVIRIS BR

4.2.1. ΔR_{AVIRIS} (R_{829} versus R_{902})

The mean reflectance curves for the five sites at the two illumination positions are given in Figures 4-1 to 4-5. Each figure consists of two graphs, with the upper graph showing the reflectance curves for the first part of the AVIRIS spectral range (383nm to 1342nm), and the lower graph showing the reflectance curves from 1422nm to 2502nm. Note that the Y-axis range varies between the upper and lower graphs. Noise is expected in AVIRIS data in two regions, where the four AVIRIS spectrometers over-lap, and where the spectrometers straddle atmospheric absorption areas of the spectrum. This noise is apparent in the curves presented here, in the form of high and low spikes. The spectrometer overlap regions are located between 680-703nm, 1244-1283nm, and 1830-1867nm. The central 1820-1950nm region contained a high degree of noise, which may be attributed to absorption by atmospheric H_2O . As a result, this region was removed from consideration. Each graph plots the mean R values for R_{829} and R_{902} with dashed lines showing one standard deviation around the mean. The dashed lines show sections of the spectrum wherein within-stand variance is low enough for comparison between sites.

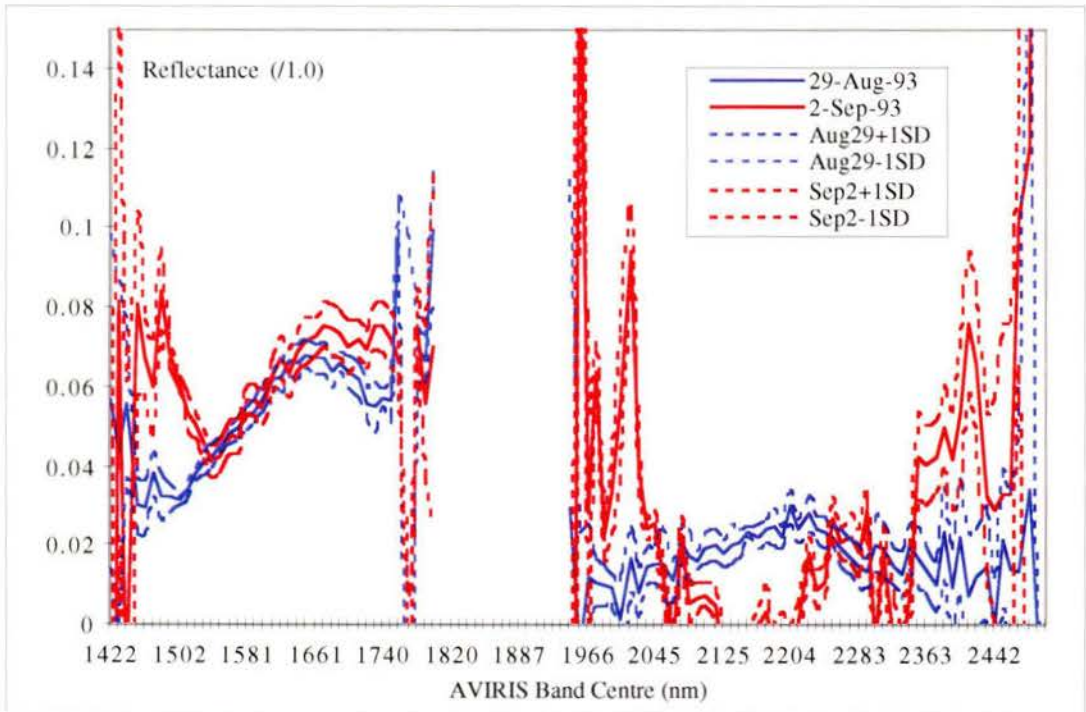
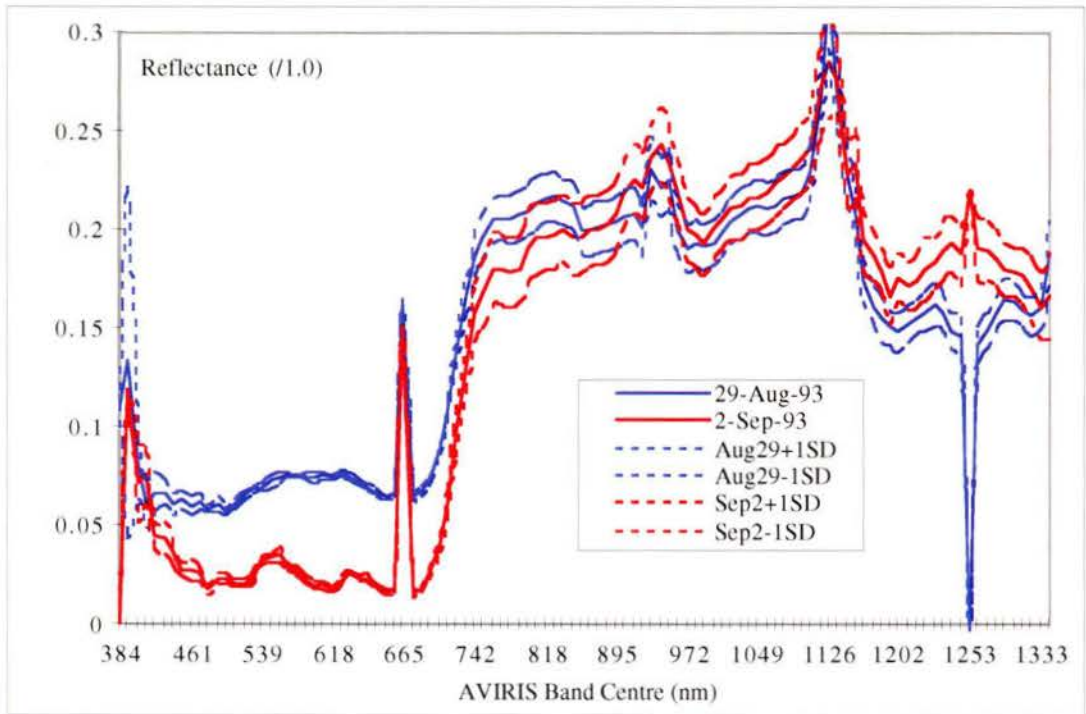


Figure 4-1. Site 10 AVIRIS mean reflectance of 3x3 sample with dashed lines showing one standard deviation (top, 384 - 1342 nm; bottom, 1422 - 2502 nm)

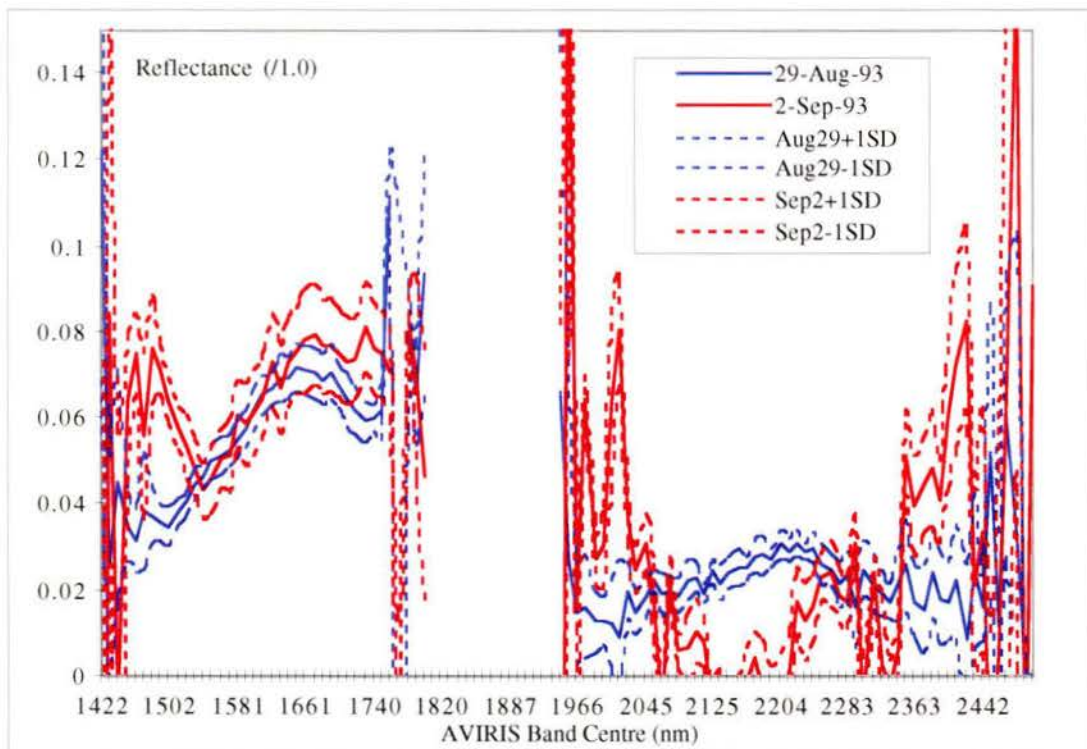
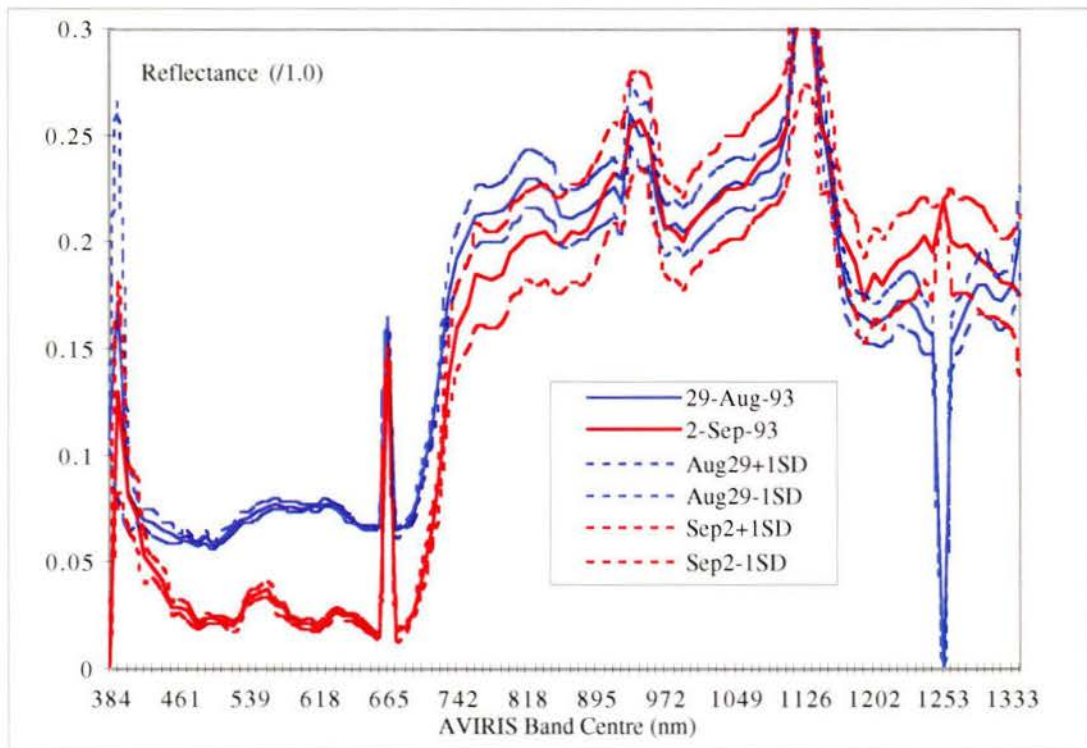


Figure 4-2. Site 9 AVIRIS mean reflectance of 3x3 sample with dashed lines showing one standard deviation (top, 384 - 1342 nm; bottom, 1422 - 2502 nm)

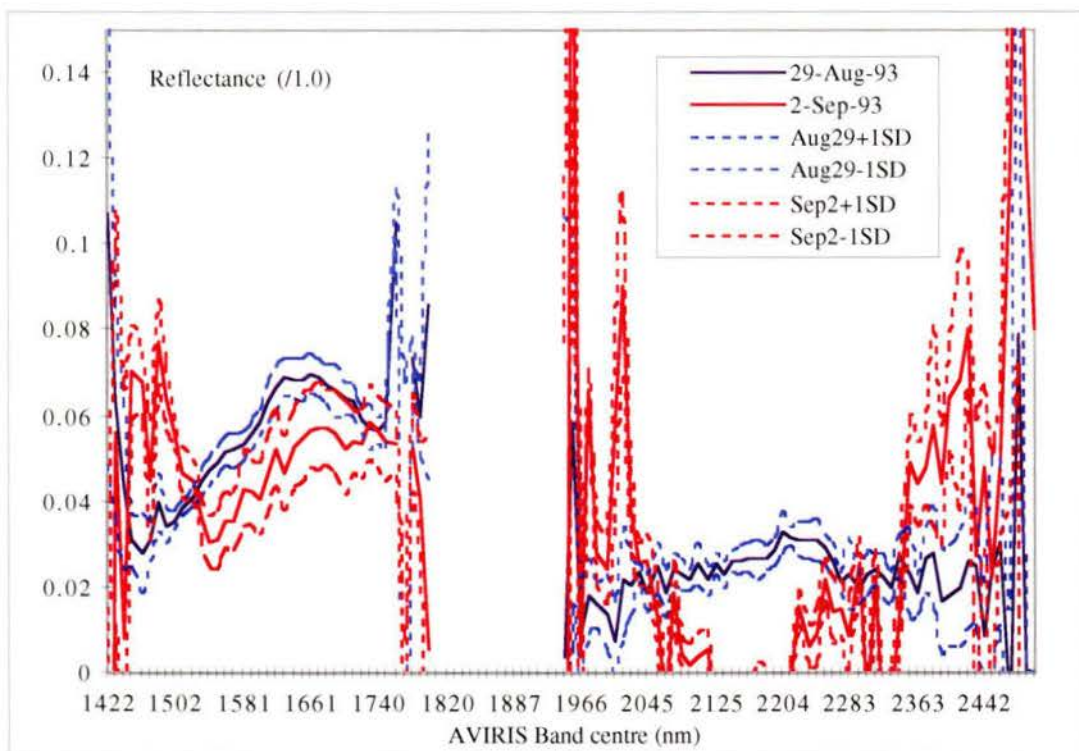
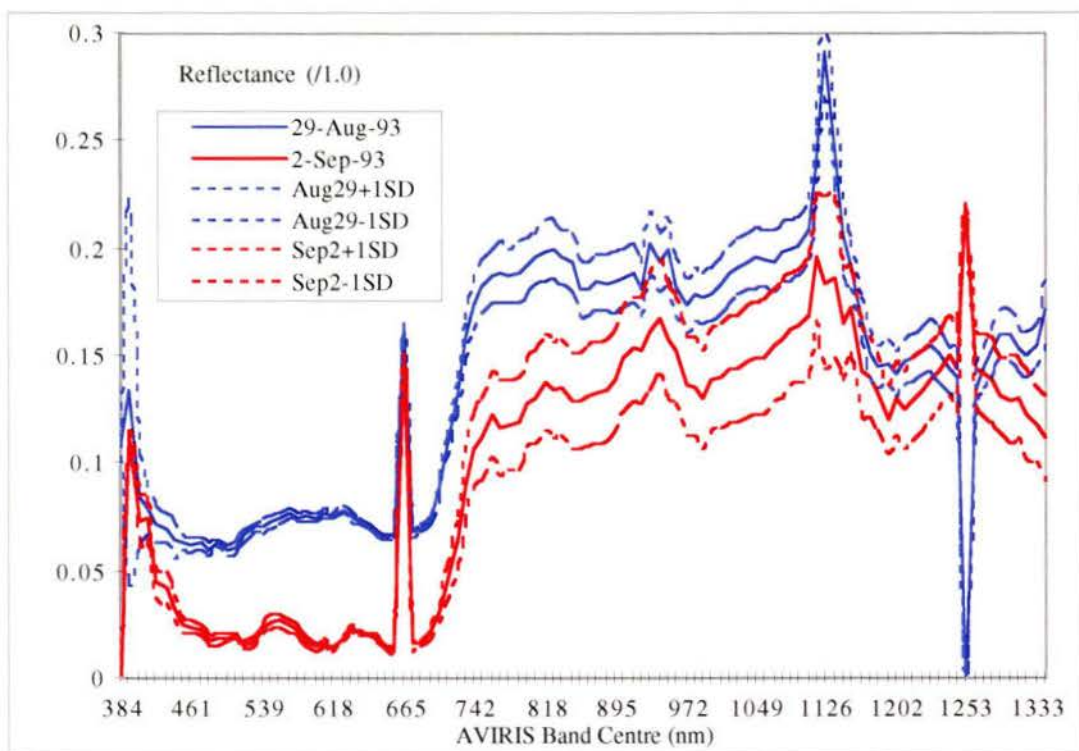


Figure 4-3. Site 8 AVIRIS mean reflectance of 3x3 sample with dashed lines showing one standard deviation (top, 384 - 1342 nm; bottom, 1422 - 2502 nm)

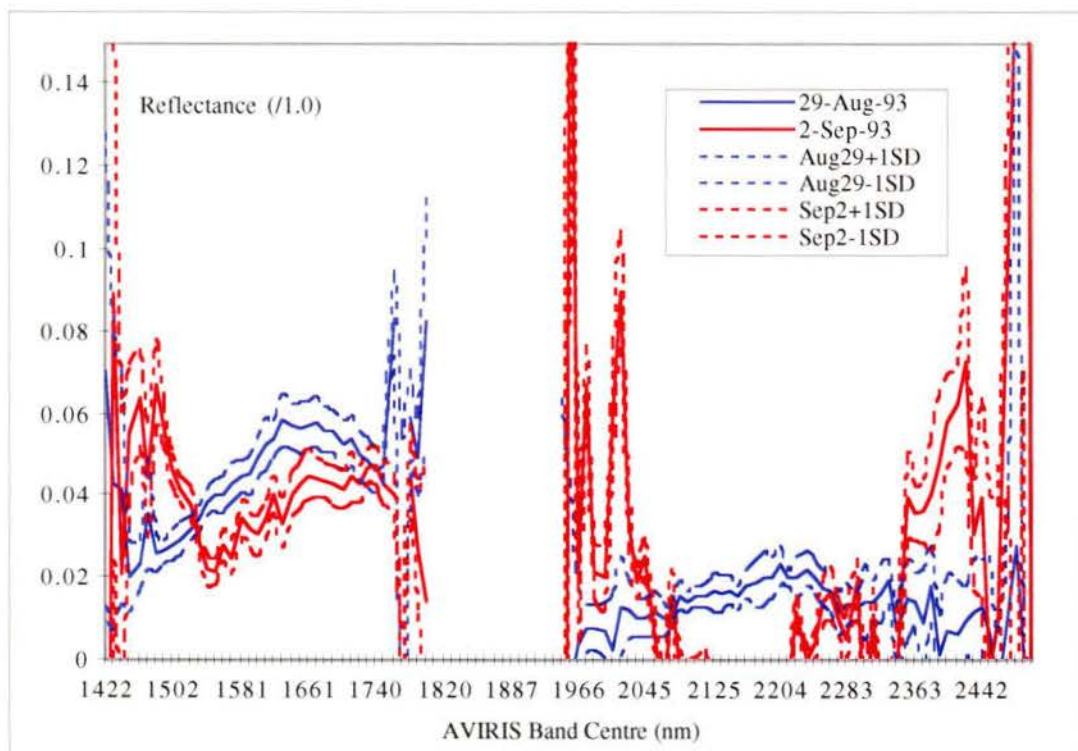
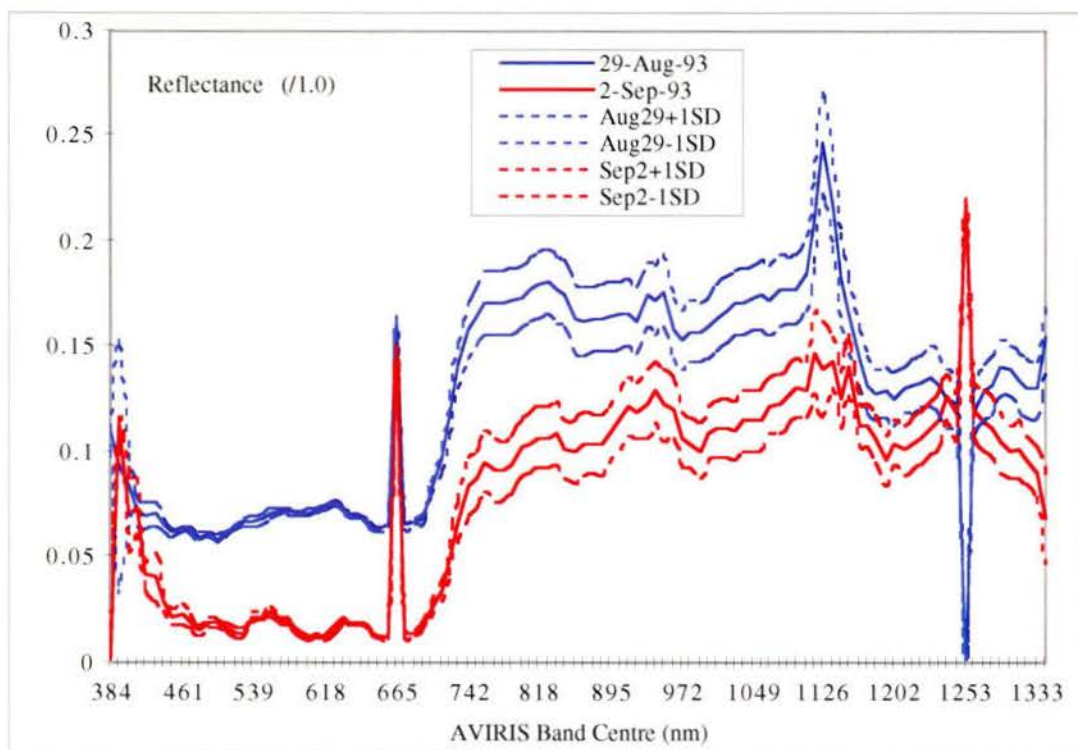


Figure 4-4. Site 7 AVIRIS mean reflectance of 3x3 sample with dashed lines showing one standard deviation (top, 384 - 1342 nm; bottom, 1422 - 2502 nm)

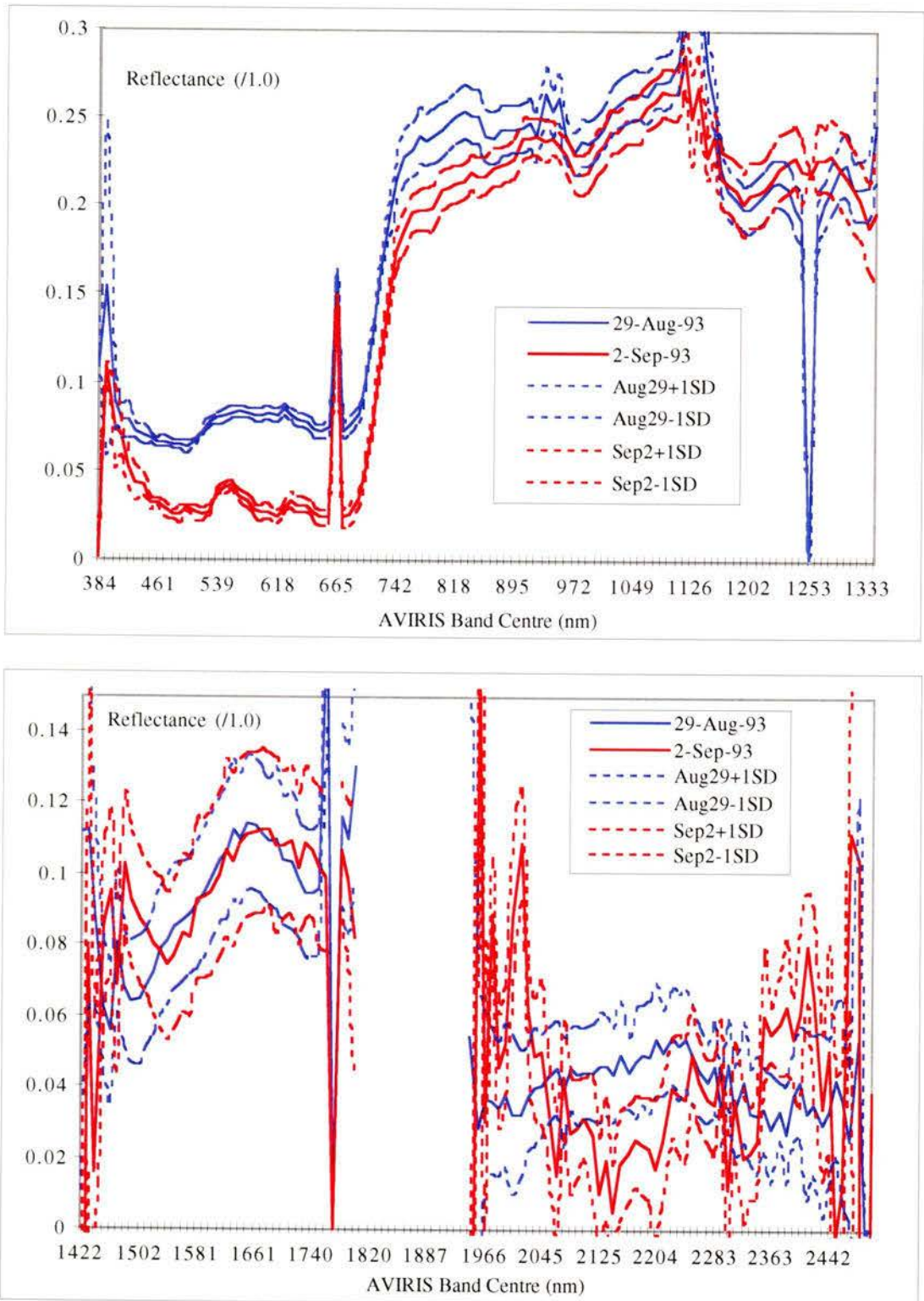


Figure 4-5. Site 6 AVIRIS mean reflectance of 3x3 sample with error bars showing one standard deviation (top, 384 - 1342 nm; bottom, 1422 - 2502 nm)

An initial comparison of Figures 4-1 to 4-5 for general brightness trends reveals that in the near infrared channel (850nm) site 6 is the brightest (0.25%), followed by sites 9 and 10 (0.22%), site 8 (0.20%) and site 7 (0.18%). An examination of general brightness tendencies in the red channel (620nm) is less enlightening. Only Site 6, at 0.08% reflectance is different from the reflectances of the other sites (all ~0.075%). Two insights can be gained from this examination: canopy density is important and, some wavelengths are better suited to BR analysis than others. The flat terrain and relatively sparse cover of site 6 produces significantly different measurements than those recorded from the other four sites, with their closed canopies and varying terrain. The canopy density factor will be examined more thoroughly in Section 4.2.3. The differences between the red and near-infrared reflectance provide a first indication that some wavelengths are better candidates for BR investigation than others. The task of identifying the best set of wavelengths is broken into two steps: first, the wavelengths displaying low within stand variance (relative to between-image change) were identified; and second, the wavelengths containing the greatest separation in change between the sites are identified. Channels that exhibit both clear separation between the AVIRIS passes and which have low internal variance are good candidates for use in the examination of canopy BR, thus the intersection of the sets described above gives the 'BR working set' channels.

Within stand variance

An examination of the error bars about the mean for each spectral curve reveals that some portions of the measurement space are unsuited to BR experimentation. In these areas the within-stand variance is too high to allow clear separation of internal variance from external change (i.e. change due to solar position). For example, at Site 6 (Figure 4-5) overlap of the error bars occurs at 895nm but not at 815nm. A reversal in relative brightness occurs between the two spectra. The light grey areas in Figure 4-6 show the normal situation where the Aug. 29th image was brighter than the Sept. 2nd image. The dark grey area (centred at 1500nm) shows the spectral region wherein the reverse holds true: the Sept. 2nd image was brighter than the Aug. 29th image. The reasons for the reflection reversal are unknown. Possible processes causing more reflectance from the canopy at the second time interval include the interactions between needle angle distribution and either solar or zenith angle (or both), or a relationship between needle structure (e.g. needle moisture) and temperature or relative humidity. The last row (I) in Figure 4-6 shows the intersection of all the sites' spectral regions wherein clear separation is available for every site. The intersection region is labelled WSVmin, for "within stand variance minimization."

Site	400nm	500nm	600nm	700nm	800nm	900nm	1000nm	1100nm	1200nm	1300nm	1400nm	1500nm	1600nm	1700nm	1800nm	
6	Grey											Dark Grey				
7	Grey											Dark Grey		Grey		
8	Grey											Dark Grey		Grey		
9	Grey											Dark Grey		Grey		
10	Grey											Dark Grey		Grey		
Int	Grey															

Figure 4-6. Summary of spectral areas of separability (based on examinations of the error bars of Figures 22-26). Grey areas show where within stand variance is low enough for comparison between sites. The dark grey area shows a region of the AVIRIS spectrum where the brightness trend reversed and the Sept. image is brighter than the Aug. image. The Int row is the spectral regions where within stand variation is low for every site (WSVmin).

Separation of mean ΔR

Reflectance-change curves were generated for each site and plotted against each other in Figure 4-7. The change is in absolute percentage points, not in relative percentage change. For example, sites 7 and 8 show a drop of 7 percentage points in the 722nm band. Some of the noise generated from spectrometer overlap and atmospheric absorption has not been removed from this graph. A second graph, Figure 4-8, plots the deep-water normalized change for the five sites. In the normalized graph, the reflectance curve of an assumed spectrally invariant area of the image (i.e. deep-water section of Sooke Lake) was subtracted from the reflectance curve for each site. Each date (Aug. 29th and Sept. 2nd) for all sites were normalized to the water signature before the normalized change curves were generated. To extend the example above, in the normalized change graph, both sites 7 and 8 show a drop in reflectance of 3 percentage points.

On examination of Figures 4-7 and 4-8, several regions of the measurement space demonstrate relatively broad separation of change for the five sites. Two candidate sections stand out; 700-840nm and 1560-1700nm, and together are dubbed the BSVmax set for “between site variance maximization.” In these sections a pattern emerges. Sites 7 and 8 exhibit the greatest amount of change, while 9 and 10 show the least change. Site 6 is generally found midway between these two groups. Explanations for these groupings are offered later in this chapter (section 4.2.3), when reflectance change and normalized reflectance change are compared to site biophysical characteristics.

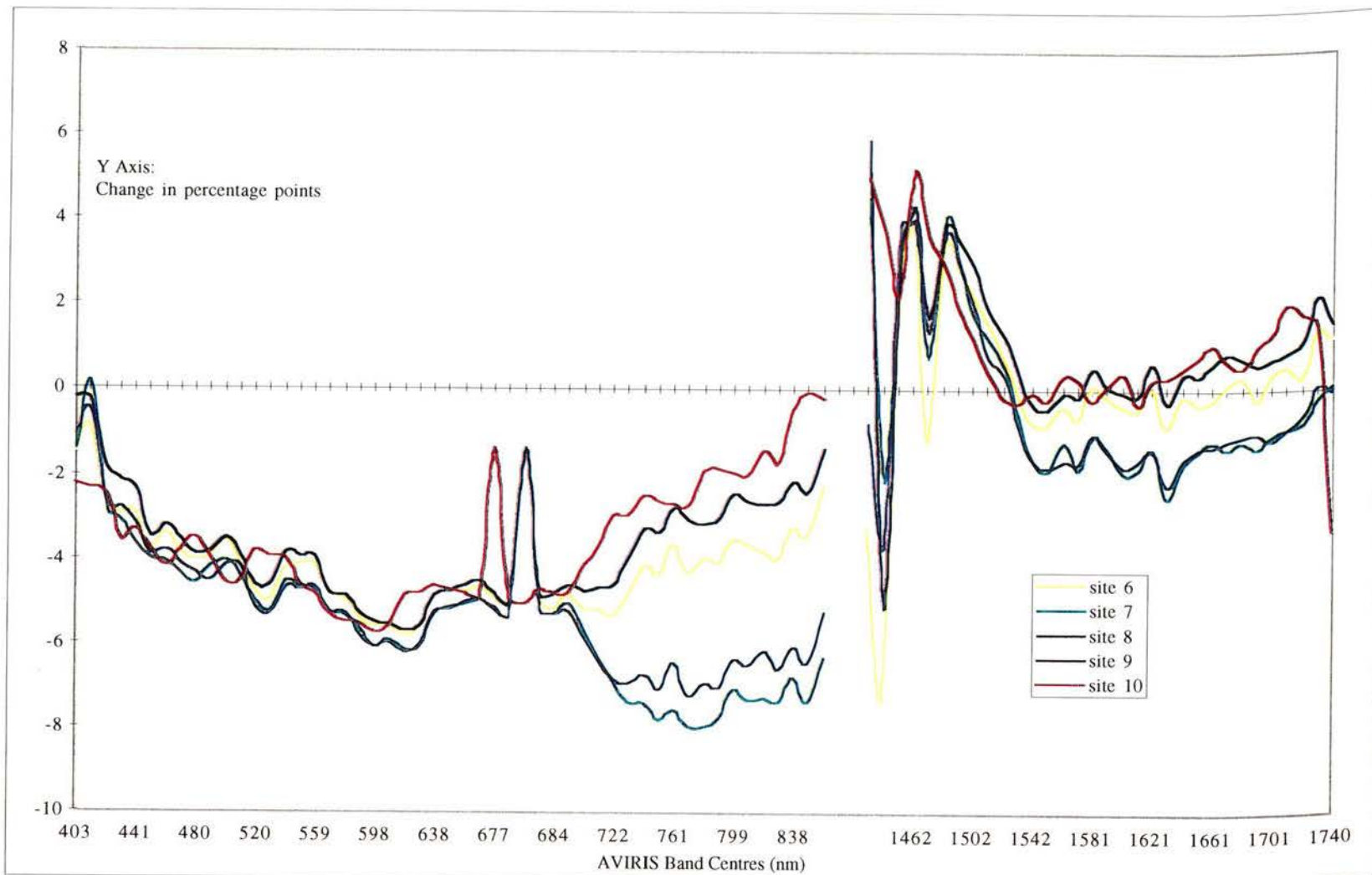


Figure 4-7. Plot of change in percentage points between August 29 and September 03 AVIRIS images

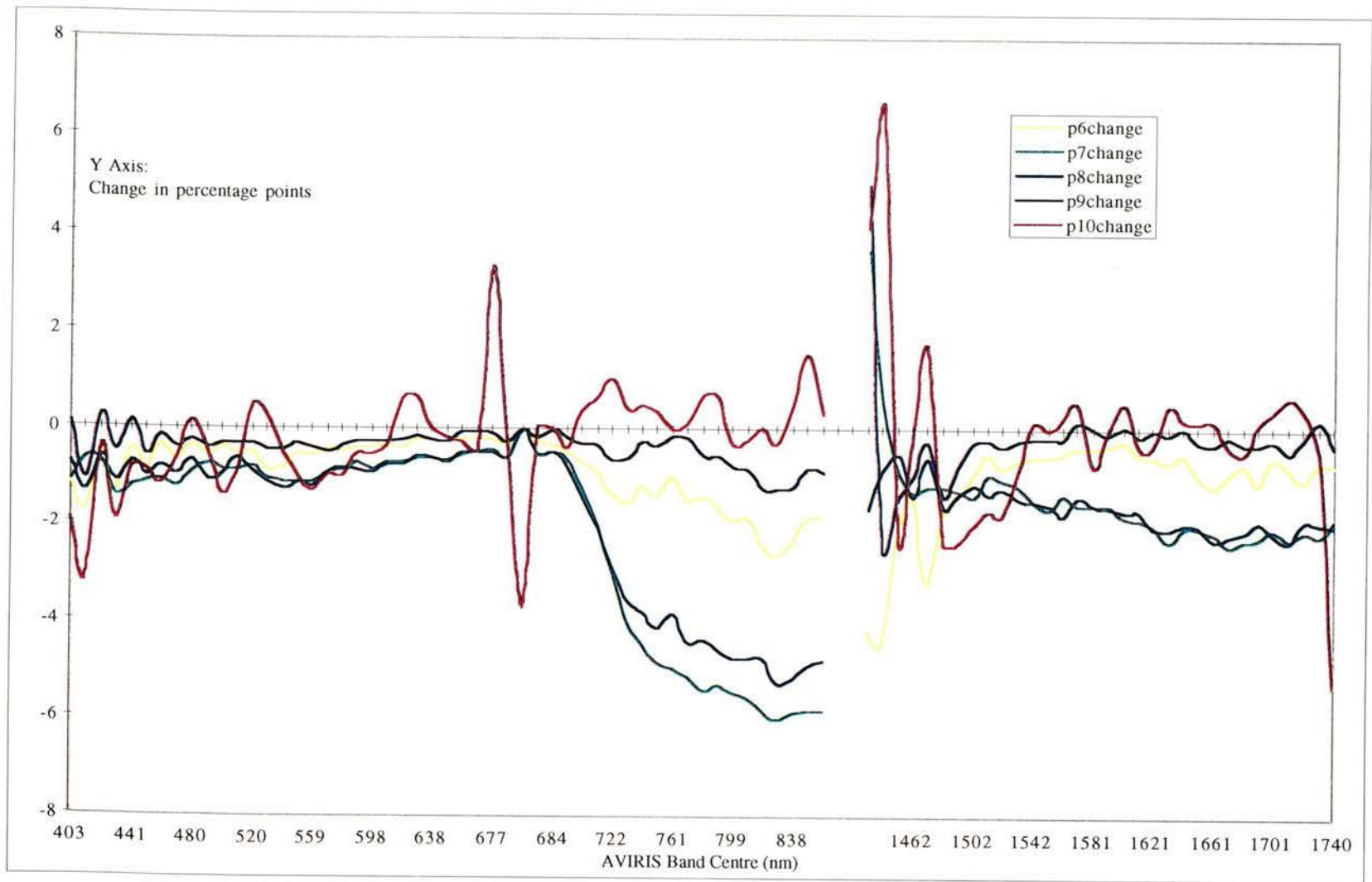


Figure 4-8. Plot of normalized change in percentage points between August 29 and September 03 AVIRIS images

The BR Working Set

There is a subset of the AVIRIS spectral measurement space that is best suited to the analysis of forest BR. This subset is formed by the intersection of (a) the subset of wavelength bands having minimal within-site variance (WSVmin), and (b) the subset of wavelength bands which maximize the between-site variance (BSVmax). Two spectral areas populate the resultant BR Working Set 703-751nm and 1452-1522nm (Figure 4-9).

Site	400nm	500nm	600nm	700nm	800nm	900nm	1000nm	1100nm	1200nm	1300nm	1400nm	1500nm	1600nm	1700nm	1800nm
WSmin		■	■	■								■	■		
BSmax				■	■							■	■	■	
BR				■								■			

Figure 4-9. Suggested BR Working Set formed from intersection of within-site variance minimization (WSmin) and between-site variance maximization (BSmax) subsets

Price (1998) looked at 45 AVIRIS hyperspectral images in order to establish the physical signature of individual spectral bands, demonstrating that five band regions (0.46-0.54 μ m, 0.61-0.69 μ m, 0.99-1.09 μ m, 1.52-1.61 μ m and 2.08-2.17 μ m) describe 98% of the mean square spectral signal. The proximity of the Price subsets to those identified in this work (0.7-0.75 μ m and 1.45-1.52 μ m) is noteworthy. Within each subset, the degree of change for the five sites changes. For instance, at 751nm, the ranking of change (from highest decrease in reflectance, in percentage points) is 7, 8, 6, 9 and 10 with change of -4.82, -4.13, -1.4, -0.37 and +0.35 respectively. At 1474nm, the ranking is 6, 7, 8, 9, 10 (-3.2, -1.18, -0.59, -0.28 and +1.7). Reflectance change rankings are discussed in more depth in Section 4.2.3 (ΔR_{AVIRIS} vs. Site Biophysical Parameters).

4.2.2. Predicted change from BR model

Burnett *et al.* (1996) implemented the model for the five sites but without considering slope or aspect, and using a non-orthographic camera model. The results, shown in Table 4-1, provide a good example of how the modeled Rpixel estimates were synthesized from areal proportion measure and radiance. Columns 2 through 4 (C%, G% & Z%) show the areal fraction estimated by the modeling process. Three iterations were modeled per site per solar position (i.e.

the virtual camera was moved 15m and the model re-rendered as shown in Figure 3-10) in an attempt to capture internal variance. The solution appears to be quite stable, with low standard deviation values (Table 4-1, column 6).

Table 4-1. Component areal extent by ray-tracing (C, G, Z), R calculations and change (from Burnett *et al.*, 1997)

	C (%)	G (%)	Z (%)	Rpixel [= 0.3(G) + 0.7(C)] Modeled	Mean	Std Dev.	Change
Site 6	1.36	76.9	21.74	54.23			
(829)	1.41	77.57	21.02	54.72			
	1	76.16	22.45	53.72	54.23	0.50	
(901)	1.14	71.93	26.93	50.69			
	1.28	72.3	26.42	50.99			
	1.26	70.95	27.79	50.04	50.58	0.49	-3.65
Site 7	6.63	39.87	53.5	29.89			
(829)	6.97	40.08	52.95	30.14			
	7.08	40.79	52.13	30.67	30.24	0.40	
(901)	5.75	34.07	60.18	25.57			
	5.52	34.43	60.05	25.75			
	5.52	34.93	59.55	26.10	25.81	0.27	-4.42
Site 8	18.66	6.15	75.19	9.90			
(829)	15.34	6.97	77.69	9.48			
	19.38	6.24	74.38	10.18	9.86	0.35	
(901)	15.77	5.55	78.68	8.61			
	12.54	6.01	81.45	7.96			
	16.91	5.06	78.03	8.61	8.4	0.37	-1.45
Site 9	9.89	18.36	71.75	15.81			
(829)	9.45	19.45	71.1	16.45			
	8.57	18.06	73.37	15.21	15.83	0.62	
(901)	8.09	15.98	75.93	13.61			
	9.01	17.12	73.87	14.68			
	8.0	17.54	74.46	14.67	14.33	0.62	-1.50
Site 10	17.69	2.12	80.19	6.79			
(829)	18.18	2	79.82	6.85			
	18.08	2.08	79.84	6.88	6.84	0.05	
(901)	14.66	1.11	84.23	5.17			
	15.11	1.11	83.78	5.31			
	14.87	1.28	83.85	5.35	5.28	0.09	-1.56

The change estimates generated from this no-slope/perspective projection model showed little difference between sites and poor relationship to the measured reflectance. The model implementation required improvement before any conclusions could be drawn.

The move to the final model, which incorporated slope and aspect and used an orthographic projection, presented challenges that have been described in the Methods chapter. Table 4-2 shows the predicted change from this final implementation. The model predicted that the flat, sparsely planted 20 year old site 6 (with a large amount of soils and shrubby understory) should be the brightest of the sites at ~60% reflectance, and have the least change as a result of

the change in solar position. Site 7 was modeled as the second brightest (30%), but due to its eastern exposure, site 7 lost the most reflectance (a drop of 14 points) as the sun moves in an azimuth from the east to the south. The model predicted that sites 8, 9 and 10 will be similarly dark (~10%), which is logical as all are mature >150 year old stands. The differences that do exist between these sites likely have more to do with slope aspect than age or structure. The model predicted little change at site 9; a relatively flat site with a south-eastern exposure. Site 8 is modeled to decrease slightly (5 percentage points). Modest change appears congruous since site 8 has an eastern aspect. The departure from the trend was site 10, with its south-western aspect. Here, the model suggested that a net increase in reflectance should occur.

Table 4-2. Final model predicted component areal extent and reflectance change (incorporating slope & aspect data) [$R_{\text{pixel}} = 0.3(G) + 0.7(C)$]. Predicted change is ranked from greatest decrease (-) to greatest increase (+) in change.

	C (%) Mean	G (%) Mean	Shad (%) Mean	R_{pixel}	Predicted Change	Predicted Rank	Actual Rank (751nm)
Site 6 (829)	2.74	85.87	11.39	60.931	-0.341	3	3
(901)	2.56	85.46	11.98	60.59			
Site 7 (829)	13.39	37.63	48.99	30.358	-14.202	1	1
(901)	6.86	20.14	73	16.156			
Site 8 (829)	21.43	4.4	74.17	9.509	-4.96	2	2
(901)	12.1	1.39	86.5	4.603			
Site 9 (829)	12.09	11.35	76.56	11.572	0.914	4	4
(901)	13.08	9.62	77.3	10.658			
Site 10 (829)	17.87	1.64	80.48	6.509	7.137	5	5
(901)	22.62	9.8	67.58	13.646			

Given the simple nature of the model and the use of component reflectance values from the literature rather than from ground measurement, only a qualitative assessment is made of how well the model agrees with AVIRIS reflectance measurements. The two last columns of Table 4-2 compare the ranking of the model predicted change in reflectance and the measured reflectance at the 751nm wavelength. The rank of highest decrease to highest increase match, supporting the thesis that the geometric structure (with a large degree of input from slope and aspect) plays a pivotal role in determining the relative reflectance of forest canopies. In the Summary chapter, suggestions are made for extensions to the model and experiment method that would allow a more quantitative examination of the BR phenomenon versus slope and aspect effects.

4.2.3. ΔR_{AVIRIS} vs. Site Biophysical Parameters

In section 4.2.1, a comparison of Figures 4-1 to 4-5 for general brightness in the near infrared (850nm) described site 6 as the brightest (0.25%), followed by 9 and 10 (0.22%), site 8

(0.20%) and site 7 (0.18%). This ranking is in agreement with the nature of the sites. Site 6 has the largest amount of exposed understory vegetation and is located in a flat area. Thus, canopy reflectance theory would suggest that it should have the highest general reflectance but low levels of change. Sites 9 and 10 are both mature sites on south facing slopes, so any shadows cast in these canopies would be cast up-hill. The effect of this is to reduce the amount of shadow in the nadir-viewed pixel. Sites 9 and 10 should be relatively bright. Sites 7 and 8 are both lower in Rithet valley and are east facing. They should exhibit the lowest relative reflectance but the largest change decrease, as the sun moves from the east to the south.

The results of a comparison of canopy biophysical parameters by site are provided in Table 4-3.A. The sites are ranked from highest parameter value to lowest. For example, Site 6 has the lowest LAI-2000 reading, mean H and density. A ranking of change in reflectance at three wavelengths (751nm, 1472nm and 1522nm) is displayed below in Table 4-3.B and modeled values are included in Table 4.3.C. The bands were chosen from the BR working subset that was distilled in section 4.2.1. This table allows for a quick search for relationships between the biophysical parameters and the measured and modeled reflectance.

Table 4-3. Comparison between site biophysical parameters, AVIRIS ΔR and modeled ΔR for the five AVIRIS experiment sites.

A. Ranking of Sites by Biophysical Parameter					
	lowest				highest
LAI-2000	site 6 (1.42)	site 9 (2.54)	site 10 (3.07)	site 8 (3.36)	site 7 (3.88)
H (mean height, m)	site 6 (5m)	site 7 (15m)	site 10 (24m)	site 8 (33m)	site 9 (43m)
Density (stem/ha)	sites 6 & 8 (450)		site 7 (500)	site 10 (550)	site 9 (675)

B. Ranking of Change (902-829) in R for three spectral band centres					
	highest -				highest +
751nm	site 7 (-4.82)	site 8 (-4.13)	site 6 (-1.4)	site 9 (-0.37)	site 10 (+0.35)
1472nm	site 6 (-3.2)	site 7 (-1.18)	site 8 (-0.59)	site 9 (-0.28)	site 10 (+1.7)
1522nm	site 10 (-1.77)	site 8 (-1.25)	site 7 (-1.05)	site 6 (-0.82)	site 9 (-0.34)

C. Ranking of Change (as predicted by final run of model)					
	highest -				highest +
ΔR predicted	site 7 (-14.2)	site 8 (-4.96)	site 6 (-0.34)	site 9 (+0.914)	site 10 (+7.14)

The LAI-2000 readings appear to reflect the nature of the sites; site 6 is the most open and has the least overstory leaf density (mean H was 5m), and site 9, though mature, had the least amount of suppressed vegetation of the mature sites, and the second lowest LAI-2000 reading.

The fact that the LAI-2000 readings do not relate well to any of the other parameters proves how difficult it is to characterize forest stands through simple height, density and leaf area measures. As mentioned in section 3.2.1, the LAI-2000 measurements were not corrected for interception by tree boles, for example by taking contemporaneous sun speckle distribution measurements (Chen 1992), nor were they translated to LAI values through relationships, since the relationship for coastal Douglas fir was not available (see Table 3-1). This may partially explain why relationships between the LAI-2000 readings and the measured or modeled reflectance values are non-existent.

Height to reflectance relationships were also very weak, with the shortest canopy (site 6) often the middle ranked site in terms of reflectance. The best relationships exist between stem density and the 751nm and 1472nm bands. Generally, denser stands tended to have less reflectance change (or have a positive change) compared to stands of less density. The lack of consistent results added strength to the argument that slope and aspect play a pivotal role in the relative brightness of conifer forest reflectance. The relationship between the 751nm band and the model is strong, a result that has been discussed previously in section 4.2.2. However, further tests using a larger sample set (i.e. more readings at different times of day and for more and different stands) are needed before the relationship can be confirmed. It may be interesting to note that the model best corresponds to the reflectance change in the near-infrared, since this is the spectral location where component spectra were extracted for Li and Strahler (1985) and this experiment.

4.3. Experiment 2: MEIS-II BR

4.3.1. Results: bidirectional radiance hemisphere modeling

Before giving the results of the MEIS-II experiment, it may be useful to summarize some of the differences in experimental design between the two experiments. The MEIS-II experiment differed from the AVIRIS experiment temporally, spatially, structurally, and in terms of model inputs. There was only one MEIS-II flight, so BR comparisons based upon multiple look or sun angles (i.e. temporal change) were impossible. Spatially, the Haysite was localized to one site, resulting in a constant slope and aspect for the experiment. Since slope and aspect had confounded the BR analysis in the AVIRIS experiment, finding a relatively flat site was seen as an important change in the experimental design. Structurally, the Haysite offered better stem-

mapping data, though it was limited to two different structural units (canopies). Lastly, the number of component variables used in the model was changed from three to four.

The decision to increase the number of components was based upon evidence that the shadowed portions of the canopy contributed, and contributed differently, to the pixel radiance. This evidence came from examining the H-resolution MEIS image and the spectral values extracted from the transects (Figure 3-14). Whereas, the shadowed area contribution to the L-pixel total was negligible (Li and Strahler [1992] suggest values of 0.0 for Z [shadow]) only rarely did the radiance drop to zero, and then only in the mature canopy, and the shadowed crown and shadowed ground components often had markedly different values. Additionally, upon examination of the ray-tracing output, it was noted that use of the 3-variable resulted in the discarding of a large amount of detail that the ray-tracing program output provides (Figure 4-10).



Figure 4-10. Ray-tracing output showing gradations of shadow in coloured area and four-component classified section (C, T, G, and Z) in grey-scale area.

Models that made use of more of the ray-tracing detail would include components intermediate to shadow and sunlit. This idea is discussed in Chapter 5. The result of this debate was the extension of the model to four end members by splitting the shadow component into shadowed ground (Z) and shadowed crown (T), as described in Equation 5.

The first modeling runs were processed with component R values extracted from two transects as described in section 3.3.5. Results from this run were published in Burnett *et al.* (1997). The component R values used for this first run were assumed to be equivalent for both immature and mature canopies (Table 4-4).

Table 4-4. Image derived component radiance values and derivation for initial and final modeling runs. *Areas of pure G (sunlit background) are very difficult to locate in 1m resolution image, especially in the immature site.

			Rt	Rc	Rz	Rg
A. Initial Haysite Model	- imm. = mat. - values from transect (Figure 3-15)	641 nm	15	153	0	181
		875 nm	81	199	19	208
B. Final Haysite Model	- values from point sampling	imm. 641 nm	40	83	4	12*
		imm. 875 nm	130	179	75	90*
		mat. 641 nm	45	122	0	12*
		mat. 875 nm	107	181	17	63*

The semi-hemispheric BR surfaces generated by the modeling process are presented in Figures 4-11 and 4-12. The X and Y axis show the Cartesian coordinates for illumination position, with the Y axis as the north-south plane. View position remains constant at nadir and so the origin (0, 0) value is the amount of radiance that the model predicts would radiate from the stand when the sun is directly overhead. The graphs show only one half of the hemisphere, the half for which model predictions were made. As noted by Deering (1989), for vegetation on flat terrain, the assumption of symmetry is appropriate. The assumption of symmetry would not be true for plots on a slope where asymmetric shadow elongation effects would skew the predicted values.

The semi-hemispheric plots have a characteristic “Hershey’s Kiss” shape. With the view angle fixed at nadir, brightness is a factor of the amount of shadow cast over sunlit portions of the canopy and background. Forest canopies have a marked vertical structure that results in rapid extinction of sunlit background with a small increase in solar zenith angle (as the sun descends). Thus the semi-hemispheric plots drop from their peaks quickly and then the radiance or reflectance change slows with bright reflectance at nadir. Later, a second slope break is produced by the extinction of much of the sunlit crown area when the solar zenith angle passes through ~50-60° SZA. This second slope break is probably related to the size and distribution of conifers in the site.

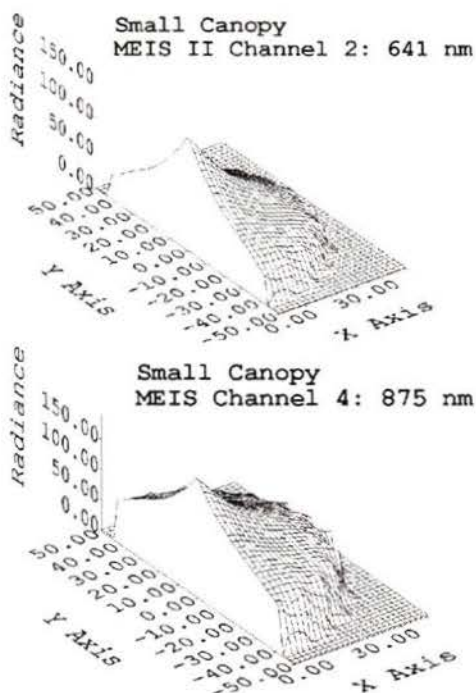


Figure 4-11. Semi-hemispheric models: immature canopy at 641 and 875 nm. The X and Y axis show the Cartesian coordinates for illumination position, with the Y axis as the north-south plane. View position remains constant at nadir, and so the origin (0, 0) value is the amount of radiance that the model predicts would radiate from the stand when the sun is directly overhead.

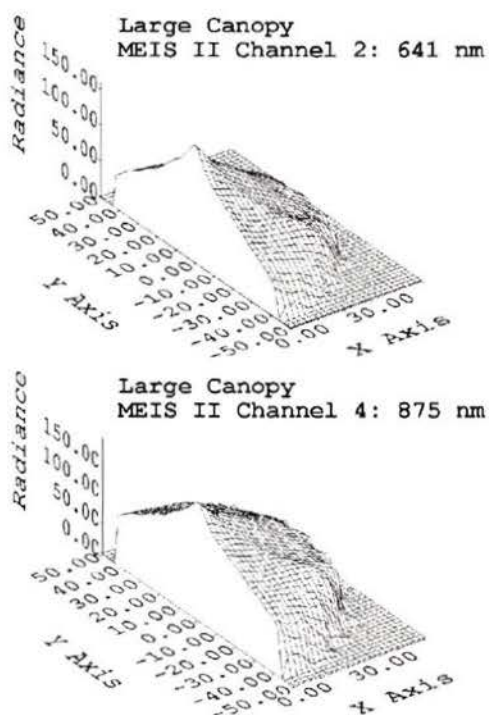


Figure 4-12. Semi-hemispheric models: mature canopy at 641 and 875 nm.

4.3.2. Analysis: $R_{\text{MEIS-II}}$ vs. R_{MODEL} (1st Run)

The results of the first modeling runs (the semi-hemispheric plots) were assessed by comparing the estimated radiance value for each stand with a mean value extracted from three samples of each canopy. The size of the samples taken from the MEIS-II images was chosen to correspond to the size of the modeled virtual canopy, approximately 40m^2 . The model values are taken from the rendering with the illumination position closest to solar position at the time of flights (i.e. with an azimuth angle of 133° and zenith angle of 48°)(Table 4-5). With the initial transect-based R inputs (3.3.5), the model predicts that the mature canopy will have a higher overall tone than the immature canopy. A mature site overall radiance greater than immature site radiance is not consistent with the MEIS-II measurements (3.3.7). Two reasons for this reversal are suggested: either the areal measurements (based on the ray-tracing and tree modeling) inaccurately described the relative amounts of the components making up R_{pixel} , or one or more of the component R values were incorrectly estimated, and both of these sources of error may have contributed to the inconsistency.

Table 4-5. Comparison between MEIS-II radiance measures and estimates of radiance from geometric-optical model

	Imm. R 641nm (Std. Dev.)	Imm. R 875nm (Std. Dev.)	Mat. R 641nm (Std. Dev.)	Mat. R 875nm (Std. Dev.)
A. Modeled				
Transect-based R values, initial run of model	40.6	76.9	51.9	90.9
B. Point sample-based R, final run of model				
	28.4	109.2	29.6	71.9
C. Measured				
Sample #1	31.4 (23.3)	125.7 (37.1)	32.3 (37.8)	97.7 (52.4)
Sample #2	27.5 (21.6)	115.7 (33.9)	30.4 (34.1)	88.8 (50.3)
Sample #3	26.3 (24.3)	116.7 (38.0)	22.8 (33.3)	74.7 (51.5)
Mean	28.4	119.6	28.5	87.1

The Li and Strahler geometric-optical model is a simplification of the forest canopy which takes advantage of a known phenomena: that, in non-closed canopies, the shape and distribution of the scene elements is a key element determining the relative tone in remotely sensed imagery (Li and Strahler 1985). The model had already been extended for this study. It was thought that further extension (incorporating more components or more complex primitives) would limit the utility of the research to establish anything definite about the role that structure plays. Finally, the Li and Strahler model is well established and understood and re-working of the model design may have

jeopardized the robustness of the experiment. Accordingly, efforts were undertaken to improve the estimation of the component radiance values.

The estimation of R_g (sunlit background) was thought to be the least robust of the four component values. R_g was estimated from a sample extracted from an adjacent bright, non-forested site. Locating 'pure' sunlit areas within the study sites in the 1m imagery was difficult, and the adjacent logged site with its dense low vegetation was deemed the best analogue for the sunlit background (understory) component. In order to examine how sensitive the model was to change in R_g value, two lower values were input and mean reflectance curves generated (Figure 4-13). The green curves represent the initial conditions, and R_g is high, at 181. When the R_g value is dropped to 91, the curves (dark and light blue) begin to change position, and when a R_g of 45 is used, the immature stand radiates more brightly than the mature site.

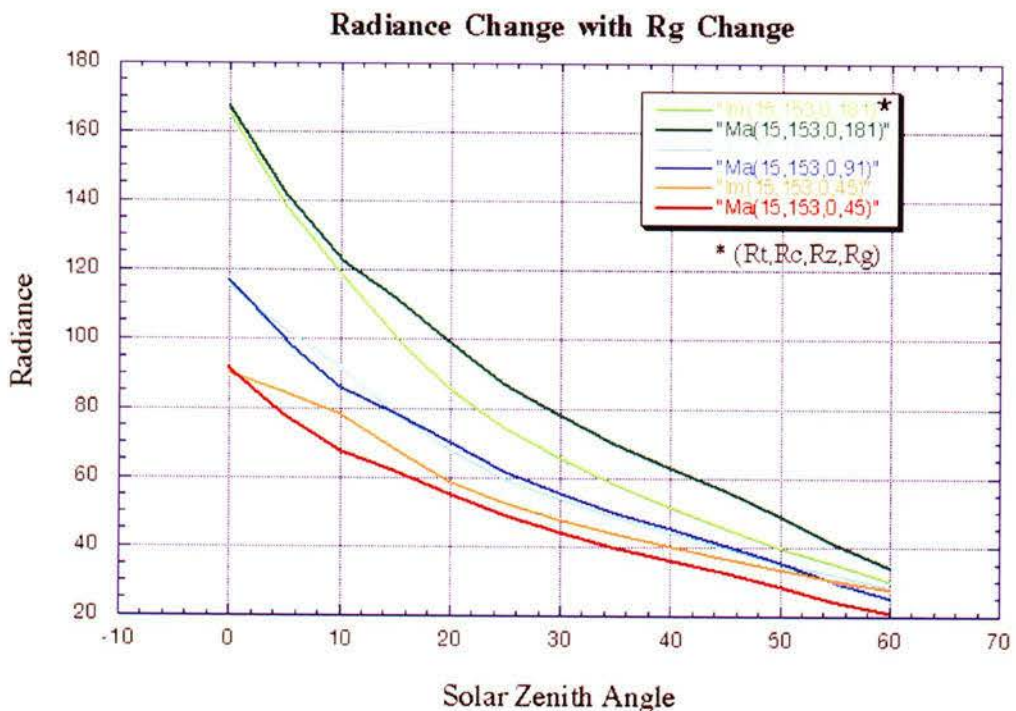


Figure 4-13. Radiance change with change in sunlit background (R_g) value. The two green curves represent the original estimations, when R_g was assumed equivalent to a pixel in a neighbouring clear-cut. Note that for the green curves, the mature is estimated to be brighter. An L-pixel examination of the two canopies proved this incorrect and this change in R_g values resulted in a better estimation (red and orange curves), where overall the immature canopy is brighter.

Spanner *et al.* (1990) acknowledges the contribution of understory to stand spectral response in their study of temperate coniferous forests. Franklin (1986) also makes note of the danger in underestimating the influence of background reflectance on the larger pixel. An improved method for the estimation of R_g was required.

The next criticism of the initial transect-based R estimation methodology was of the assumption that the R values should be similar for both canopies. The equality assumption had been made to expedite the assembly of the first 3D surface plots. Though it is obvious from the transect data that this assumption was not very accurate, at the time it was thought to be a significant improvement over the use of literature-derived values (as in the AVIRIS experiment). To remedy this for the final model run, samples were taken from both canopies and a different set of R values compiled for each (Table 4-5, B rows).

As noted above, three of the four component radiance values (R_c , R_t , and R_z) were extracted from two arbitrary transects. The transect method is prone to error because it is based on the assumption that each line passes through areas containing each of the components. On the positive side, the transect method is an attempt to take some of the subjectivity out of the model, and the resulting transect graphs are useful for examining gross trends within the canopy. The point sampling method used to estimate the R values for the final model run abandons any pretence to objectivity: the quality of the estimate is proportional to the researchers knowledge and interpretation of the canopy. In the point sampling method, the researcher uses air-photographs, knowledge of the ground and the image itself to locate areas that represent spectrally pure component pixels. The R values acquired by this method are shown in the lower half of Table 4-5.

4.3.3. Analysis: R_{MEISH} versus R_{MODEL} (Final Run)

The results of the final model implementation estimations (Table 4-5) are in agreement with the mean of the MEIS-II samples. In the 641nm band, the values are very close (28.4 versus 28.4 for immature and 29.6 versus 28.5 for the mature), while in the 875nm band the modeled versus measured is less close (109.2 versus 119.6 for immature and 71.9 versus 87.1 for the mature). The fact that the IR band is showing a weaker relationship may suggest a need for a change in the model. In both the immature and the mature cases, the model underestimates radiance. Since the location for R extraction appears to be reasonable, at least from an examination of the 641 modeling versus measurement, it may be the estimation of areal components for the IR that requires modification. For instance, it could be that the nature of the scattering (in the IR wavelengths) inside the canopy increases the tone of adjacent 'shadowed' areas. In other words, the fuzzy boundary of the sunlit component extents may be sharper in the visible than in the infrared. The result of this IR 'spill-over' would be enlarged sunlit crown and background areal components and, consequently, brighter R_{pixel} values.

Without more BR measurements, the robustness of the complete estimated hemispheric surface could not be gauged. The production of BR surfaces must be valued as an exercise in producing representations of the anisotropy of a vegetated surface using ray-tracing and a simple geometric-optical model. As such, the exercise was more of practical interest than of pure research.

4.4. Chapter Summary

In this chapter, the results and analysis of the two experiments comprising the thesis were presented. The analysis of the AVIRIS experiment began with an examination of the general brightness of the sites. In the near-infrared bands, the ranking of brightest to darkest sites was 6 (immature) > 9 and 10 (mature) > 7 > 8 (juvenile and mature, respectively). The effort to identify the best set of bands was broken into two parts: identification of spectral bands where internal variance was low and identification of spectral bands where between-site variance was high. The resulting set of bands (The 'BR working subset') covered the spectral ranges of 703-751nm and 1452-1522nm.

The modeling of the five sites used in the AVIRIS experiment was first undertaken without the incorporation of slope and aspect, and using a perspective rather than orthographic camera. Results from this model run were not well related to the measured (AVIRIS) values. Literature-based reflectance values were used for the component reflectance values for both the early model and the final model implementation. The final model, including slope and aspect, predicted site 6 to be the brightest reflector, followed by 7 and then 8, 9, and 10 grouped together as the darkest. The model also predicted that site 7 would have the greatest change. The ranking of change matched that recorded by the AVIRIS sensor. The comparison of the measured reflectance change (AVIRIS) to site biophysical parameters produced only weak relationships. Due to the confounding effects of slope and aspect, the 5 sites were not on "a level playing field" and so quantitative comparisons of BR could not be made.

In the MEIS-II, experiment, the first model run was made using the same component R values for the immature and mature canopies. These R values were extracted from the imagery using a transect method, or, in the case of R_g, from a nearby, non-forested site. Both the transect and the extra-site R_g estimation methods were found to be flawed. The resulting 3D BR surfaces looked similar to those found in the literature, but when compared with the value measured by the MEIS-II sensor, the mature site was modeled brighter than the immature site. The model inputs were improved by using a point sampling method. The results of the final model implementation

were in good agreement with the measured MEIS-II radiance values. The agreement in the red band was better than in the infrared.

5. Summary and Conclusions

5.1. Summary

5.1.1 Experiment 1: AVIRIS BR

The analysis of the AVIRIS experiment began with an examination of the general brightness of the sites. In the near-infrared bands, the ranking of brightest to darkest sites was 6 (immature) > 9 and 10 (mature) > 7 > 8 (juvenile and mature, respectively). General brightness in the visible was seen to relate to tree size and distribution, and, more importantly, to site slope and aspect. A comparison of general brightness in the visible was less revealing, and only site 6 displayed a markedly different (and brighter) reflectance. This was an early indication that there were particular channels suited to BR exploration. The effort to identify the best set of bands was broken into two parts: identification of spectral bands where internal variance was low and identification of spectral bands where between-site variance was high. The resulting set of bands (the 'BR working subset') consisted of the spectral ranges of 703-751nm and 1452-1522nm.

The modeling of the five sites used in the AVIRIS experiment was first undertaken without the incorporation of slope and aspect, and using a perspective rather than orthographic camera. Results from this model run were not well related to the measured (AVIRIS) values. Literature-based reflectance values were used for the component reflectance values for both the early model and the final model implementation. The final model predicted site 6 to be the brightest reflector, followed by 7 and then 8, 9, and 10 grouped together as the darkest. The model also predicted that site 7 would have the greatest change. The ranking of change matched that recorded by the AVIRIS sensor. The hypothesis underlying the Li and Strahler model, that geometry plays a pivotal role in determining the relative reflectance of forest canopies, was thus upheld.

The comparison of the measured reflectance change (AVIRIS) to site biophysical parameters revealed only weak relationships; of these, stem density and 751nm and 1472nm bands were the most clear. Generally, denser stands tended to have less reflectance change (or a positive change) when compared with less dense stands. Due to the confounding effects of slope and aspect, the 5 sites were not on "a level playing field" and so quantitative comparisons of BR could not be made. The need for more than two BR angle-measurements to attempt a differentiation between forest stand parameters based on BR change was emphasized.

The distribution of 3D primitives (modeled trees) using a recursion of field work-determined tree clusters was shown to have shortcomings. The methodology worked reasonably well except when tree heights were large and insufficient numbers of clusters were placed to the sun-ward of the sample region. The addition of stems as well as crowns in the later models proved to be an important addition to the simulation.

Overall, the modeling of the geometric-optical relationships using ray-tracing was successful. Results of the ray-tracing-based modeling support the hypothesis that the shadow areal component grows with increasing solar zenith angle at the expense of sunlit background and sunlit crown areal components. The model predicts more reflectance change to occur in stands with younger trees. Sites with no trees should have very little change between SZA-different images.

5.1.2. Experiment 2: MEIS –II versus ray-tracing-based GOM

Semi-hemispheric BRF distributions were calculated for two structurally distinct stands of Douglas-fir forest via several runs of a computer graphics (ray-tracing) implementation of the Li and Strahler (1985; 1986) geometric-optical model. The bidirectional reflectance factor distributions were made as a function of changing solar position. Only a single image (i.e. one solar position) was available for comparison to the model-predicted values.

The first run of the model was made using identical R values for both immature and mature components. The component R values were extracted from the imagery using a transect method, or, in the case of R_g, from a nearby non-forested site. Both the transect method and the extra-site R_g estimation methods were found to be flawed. The resulting BRF surfaces looked similar to those found in the literature, however, when tested by comparison to the radiance measured by the MEIS-II sensor for 48° zenith and 133° azimuth, the surfaces were found to be incorrect. Based on the mean of three 40m² samples, the mature stand was modeled to be the brighter canopy. To correct this, the input method was improved by replacing the transect with a point sampling method, which called on researcher knowledge of the crowns to find likely locations for the "pure" R component spectral signatures. In particular, the estimation of R_g (sunlit background) was improved. From field visits it was noted that the sunlit ground patches on the forest floor were often too small to be resolved on 1m pixel size imagery.

The results of the final model implementation were in good agreement with the measured MEIS-II radiance values. The agreement in the red band was better than in the infrared, prompting the suggestion that the model might have to be modified to incorporate more of the

reflectance nature of the infrared reflectance within the canopy (i.e. addressing the "spill-over" effect).

5.2. *Conclusions*

An attempt to understand the physical basis for BR effects was made using a ray-tracing implementation of the Li and Strahler (1985; 1986) geometric-optical model. The Li and Strahler model used in this thesis is an example of a mechanistic mathematical model; it uses *a priori* knowledge of the radiation regime in forest canopies. The two thesis experiments can be seen to lie within the second step in the inductive/deductive approach to pure science that is described by Curran (1987). Credit for the inductive first step is given to Li and Strahler, and their progenitors. In both experiments, model predictions for reflectance or radiance were compared to actual (airborne) measurements of reflectance, and then with ground-truthed stand parameters. The model approach was adopted to test the robustness of the theory and to circumvent difficulties associated with studying forest canopy anisotropy by other methods (such as the high costs of acquiring of repeat (BR) measurements, i.e. though towers structures or flights). This research sought to contribute to an understanding of conifer bidirectional reflectance as defined by two questions:

1. *To what extent is canopy structure a factor of BR in conifer forest canopies?*
2. *How does stand age change the canopy structure / reflectance relationship in a Douglas fir forest?*

The results from the two experiments documented in this thesis support the reliability and appropriateness of using the Li and Strahler geometric-optical model for modeling the open to moderately dense coastal Douglas-fir forests. There were, however, insufficient data for model calibration, which might have allowed for an inversion of forest parameters from reflectance measurements. In order for calibration to be possible, several more sun-angle BR measurements and better ground truth in the form of spectral signatures for pure components are required.

This research supports the theory that canopy structure a major factor driving BR in conifer forest canopies by showing a general agreement between ΔR recorded by AVIRIS and modeled ΔR for five structurally diverse sites. Structure drives the model, and thus if the model and the recorded values are in line, then structure must be a main factor driving canopy BR. The stronger the relationship between model and measure, then the greater the 'extent' that structure plays. The AVIRIS experiment relationship was apparent but weak. However, this can be attributed to relief effects and to a lack of a representative continuum of structural diversity in the set of sites. The AVIRIS experiment lacked adequate BR measurements, sites and ground-

truthing to provide a definitive answer on the role of structure. The MEIS-II experiment was more reliable, since it used identical slope and aspect for the two sites and better ground truth. Modeled to measured relationships were stronger, though only one measurement was available. The Li and Strahler model appears to capture forest canopy BR. By extension, forest structure appears to be a major factor defining the Douglas-fir canopy reflection regime.

The second research question focused on the effect of stand age on the relationship between structure and reflectance. The results of the two experiments were insufficient for a thorough analysis of this problem. The sample size was too small for statistical evaluation and the effects of topographic relief made the limited results obtained questionable. However, general trends were apparent. The forest stands examined as part of this research consisted of either 5 or 30 year old plantation (sites 6 and 7) or >100 year old natural regeneration (sites 8, 9 & 10). Because the plantation sites have been managed (planted, thinned), the differences between the sites can not be referenced to age alone. When this is combined with the fact that site conditions varied considerably, and that relief differences were seen to strongly affect the results (of the modeling), the question of changing relationship with age is shown to be oversimplified. Only a more comprehensive examination of the BR of Douglas-fir canopies over a wide range of age classes could come near to defining such a relationship.

A secondary research question was posed, which was derived from an examination of the thesis method:

3. What are the benefits of using a 3-D graphics implementation of the geometric optical model?

The costs of employing ray-tracing for modeling is common to any computer simulation of canopy radiation regimes; it is computationally intensive (Goel 1988). Ten hours were required to render the scenes needed to build one semi-hemispheric BRF function in the MEIS-II experiment and the extraction of component areas took another 10 hours. This must be balanced with the benefits of ray-tracing, including the visual feedback provided by the output (set-up errors are visible), the flexibility (infinite customization of scene elements, illumination and sensor parameters, and site parameters such as slope and aspect), and the true (as opposed to statistical) incorporation of mutual shadowing of scene elements.

Epistemological stance

Finally (and with a nod towards Dr. Moss), this research thesis was undertaken in the spirit of 'pure science' as defined by Curran (1987), driven in large part by curiosity, with only a modicum of whim. However, this being a Master of Science thesis, it might be more accurate to state the existence of practical goals; by embracing this experience as a journey, the candidate sought to develop skills and discipline in the areas of time management, problem solving, analysis, synthesis and communication. The journey has been most satisfying.

5.3. Future Research

In writing this thesis, I have had to wrestle the description of a research 'journey' into the relatively static and linear form of a thesis, adopting the customary hypothesis-testing style popular in the physical sciences. In so doing I have not accurately conveyed how non-linear the experience was. In the interests of readability much of my (crude) initial efforts (which provided the first insights into the processes being examined and led to the final 'improved' methods), are not documented. The method developed over time and the results discovered (or not) have suggested more (and even better!) ideas on how to examine the canopy BR phenomena. Four areas I believe particularly well suited to future work are described below.

Hotspot modeling

In the MEIS-II experiment, semi-hemispheric BRF distributions were calculated for two structurally distinct stands on the basis of changes in illumination position. A useful extension would be to model the hemispheric canopy BR with reference to **view** direction. This would provide an estimate of the canopy hot-spot for the different conifer canopies.

Field measures of component spectra

The use of component spectra taken from the literature or from the imagery itself as adopted for this research is one of the main weaknesses of the methodology. It is rare that the vegetation examined in the literature is identical to that in any current study. End members estimated from the imagery assumes that the pixels are pure, an unlikely situation even with 1m resolution imagery, especially when multiple scattering effects are considered. Any future work should incorporate the use of locally measured spectra, preferably contemporaneous to the remotely sensed image acquisition.

Geometric-optical models with more components

At the 20m GRC, and to a lesser extent 1m GRC, resolution, pixels are composed of a mixture of forest scene elements caught in the instrument IFOV (dominant tree, co-dominants, understory, tree fall, litter, bedrock outcrops, open water and bare soil). The model used in this research separated this continuum into only four discrete components and gives each component a spectral signature that is unrelated to the component's areal proportion. Examples of additional model complexity that might be useful include the incorporation of more components (such as partial shadow components for crown or background) or the use of a weighted scheme whereby proportion of the component weights the spectral signature used in the calculation of R_{pixel} . The development and testing of more complex ray-tracing-implemented geometric-optical models would reveal the value of increased complexity. Figure 5-1 demonstrates the level of detail to which ray-tracing modeling programs can extend.



Figure 5-1. Ray-traced model of Englemann spruce using ray-tracing modeling software (this image was created using software [Tree Professional™ 4.0] developed by Onyx Software Inc.).

Note that added complexity may preclude use of the model for inversion purposes. The model design must be dictated by its proposed uses.

Appendix A: Glossary: list of acronyms and units

ASL	above sea level
AVHRR	Advanced Very High Resolution Radiometer
AVIRIS	Airborne Visible and Infrared Imaging Spectrometer
BSV _{max}	between stand variance maximization
BR	bidirectional reflectance
BRDF	bidirectional reflectance distribution function
BRF	bidirectional reflectance factor
CBD	crown base diameter
CCD	charged coupled device
CR model	canopy reflectance model
DBH	diameter at breast height
DF	Douglas-fir
LAI	leaf area index
GCP	ground control point
GIFOV	ground instantaneous field of view
GOM	geometric-optical model
GRC	ground resolution cell
H	height
IFOV	instantaneous field of view
MEIS-II	Multispectral Electro-optical Imaging Spectrometer II
NDVI	normalized difference vegetation index
nm	nanometer
PAR	photosynthetically active radiation
pixel	picture element
POV-Ray	Persistence of Vision, Ray-tracing software
SAA	solar azimuth angle
SEIDAM	System of Experts for Intelligent Data Management
SNR	signal to noise ratio
SZA	solar zenith angle
TRIM	terrain resource information mapping
WRC	western red cedar
WH	western hemlock
WSV _{min}	within stand variance minimization
Z ₀	surface roughness

Appendix B: Bibliography

- Abuelgasim, A.A. and Strahler, A.H. (1994) Modeling bidirectional radiance measurements collected by the advanced solid-state array spectroradiometer (ASAS) over Oregon Transect conifer forests. *Remote Sensing of Environment* **47**: 261-275.
- Avery and Berlin, (1992) *Fundamentals of Remote Sensing and Airphoto Interpretation*, 5th Edit., Maxwell Macmillan, Toronto, 472p.
- Barker Schaaf, C., Li, X. and Strahler, A.H. (1994) Topographic effects on bidirectional and hemispherical reflectances calculated with a geometric-optical canopy model. *IEEE Transactions on Geoscience and Remote Sensing* **32(6)**: 1186-1193.
- Brakke, T.W. and Otterman, J. (1990) Canopy bidirectional reflectance dependence on leaf orientation. *International Journal of Remote Sensing* **11**: 1023-1032.
- Bruce, D. (1985) Consistent height-growth and growth-rate estimates for remeasured plots," *Forest Science*. **27**: 711-725.
- Burnett, C., Hay, G., Niemann, K. and Goodenough, D. (1997) Modelling bidirectional reflectance distribution functions of conifer canopies using 3-D graphics. In Proceedings of the 3rd International Airborne Remote Sensing Conference, Copenhagen.
- Burnett, C., Niemann, K. O., Goodenough, D. and Barclay, H. (1996) Modeled directional variation in radiance versus AVIRIS-measured change for a non-homogeneous Douglas-fir forest: preliminary findings, in Proceedings of the 2nd International Airborne Remote Sensing Conference, San Francisco.
- Carr, W. W., Dobson, D. A., Lewis, T., Kirmeyer, G. J. and Sanders, P. (1992) Greater Victoria Water District Land Use Technical Review Summary Report. Terrasol Inc., Victoria, BC.
- Chen, J., and Black, T. (1992) Foliage area and architecture of plant canopies from sunfleck size distribution, *Agricultural and Forest Meteorology* **60**: 249-266.
- Chrien, T. G., Green, R. O. and Eastwood, M. L. (1990) Accuracy of spectral and radiometric laboratory calibration of the Airborne Visible / Infrared Imaging Spectrometer. *Proceedings, Imaging Spectroscopy of the Terrestrial Environment, SPIE.*, Bellingham, WA, **1298**: 37-49.
- Cierniewski, J and Courault, D. (1993) Bidirectional reflectance of bare soil surfaces in the visible and near-infrared range. *Remote Sensing Reviews* **7**: 321-339.
- Colwell, J.E. (1974) Vegetation canopy reflectance. *Remote Sensing of Environment*, **3**: 175-183.
- Curran, P. and Williamson, H.D. (1985) The accuracy of ground data used in remote-sensing investigations. *International Journal of Remote Sensing* **6**: 1631-1651.
- Curran, P.J. (1987) Remote sensing methodologies and geography. *International Journal of Remote Sensing*, **6**: 1631- 1651.

- Deering, D. (1989) Field measurements of bidirectional reflectance. *in: Theory and Applications of Optical Remote Sensing* (G. Asrar, edit), John Wiley and Sons, 14-65.
- Deering, D.W., Middleton, E.M. and Eck, T.F. (1994) Reflectance anisotropy for a Spruce-Hemlock forest canopy. *Remote Sensing of Environment* **47**: 242-260.
- Farrand, W., R. Singer, and E. Merenyi (1994) Retrieval of apparent surface reflectance from AVIRIS data: A comparison of empirical line, radiative transfer, and spectral mixture models, *Remote Sensing of Environment*, **47**: 311-321.
- Flewelling, J. (1994) Considerations in simultaneous curve fitting for repeated height-diameter measurements. *Canadian Journal of Forest Research* **24**: 1408-1414.
- Franklin, J. (1986) Thematic mapper analysis of coniferous forest structure and composition. *International Journal of Remote Sensing*, **7**: 1287-301.
- Gausmann, H. (1977) Reflectance of leaf components. *Remote Sensing of Environment*, **6**: 1-9.
- Gauthier, R.P., Teillet, R.P., Staenz, K., Landry, R., Fedosejevs, G. and Fournier, R. (1992). A measurement program for the validation of forest canopy models. *Canadian Journal of Remote Sensing*, **18**: 293-296.
- Gemmel, F. (1998) An Investigation of Terrain Effects on the Inversion of a Forest Reflectance. *Remote Sensing of Environment*. **65**.
- Goel, N. S. (1987) Models of vegetation canopy reflectance and their use in estimation of biophysical parameters from reflectance data. *Remote Sensing Reviews* **3**: 1-212.
- Goel, N. S. (1989) Inversion of canopy reflectance models for estimation of biophysical parameters from reflectance data, *in: Theory and Applications of Optical Remote Sensing* (G. Asrar, edit), John Wiley and Sons, 205-251.
- Goel, N.S. and Thompson, R.L. (1984) Inversion of vegetation canopy reflectance models for estimating agronomic variables. V: estimation of LAI and average leaf angle using measured canopy reflectances. *Remote Sensing of Environment* **16**: 69-85.
- Goodenough, D. G., Bhogal, P., Charlebois, D., Heyd, M., Matwin, S. and Portigal, F., (1996). Knowledge-based imaging spectrometer analysis and GIS for forestry
- Goodenough, D. G., Goldberg, M., Plunkett, G., and Zelek, J. (1987) An expert system for remote sensing. *IEEE Transactions on Geoscience and Remote Sensing* **25**: 349-359.
- Greater Victoria Water District Watershed Management (1991) 1:10000 Forest Cover Classification, Sooke Lake North. GVWD.
- Guyot, G., Guyon, D. and Riom, J. (1989) Factors affecting the spectral response of forest canopy: a review. *Geocarto International* **3**:3-18.
- GVWD (1997) Greater Victoria Water District Watershed Management Forest Cover Classification, Sooke Lake Watershed, scale 1:10,000, Hugh Hamilton Ltd., Vancouver, BC.

- Hafley, W.L. and Schreuder, H.T. (1977) Statistical distributions for fitting diameter and height data in even-aged stands. *Canadian Journal of Forest Research* **7**: 481-487.
- Hall, F.G., Shimabukuro, Y.E. and Huemmrich, K. F. (1995) Remote sensing of forest biophysical structure using mixture decomposition and geometric reflectance models. *Ecological Applications* **5**: 993-1013.
- Hapke, B., DiMucci, D., Nelson, R. and Smythe, W. (1996) The cause of the hot spot in vegetation canopies and soils: shadow-hiding versus coherent backscatter. *Remote Sensing of Environment* **58**: 63-68.
- Hay, G. J. and Niemann, K. O. (1994) Visualizing 3-D texture: a three-dimensional structural approach to model forest texture. *Canadian Journal of Remote Sensing* **20**: 90-101.
- Hay, G.J., Niemann, K. O. and Goodenough, D.G. (1997) Spatial thresholds, image objects, and upscaling: a multiscale evaluation. *Remote Sensing of Environment* **62**: 1-19.
- Irons, J.R., Ranson, K.J., Williams, D.L., Irish, R.R. and Huegel, F.G. (1991) An off-nadir-pointing imaging spectroradiometer for terrestrial ecosystem studies. *IEEE Transactions on Geoscience and Remote Sensing* **29(1)**: 66-74.
- Jupp, D.L.B.J. and Strahler, A.H. (1991) A hotspot model for leaf canopies. *Remote Sensing of Environment* **38**: 193-210.
- Jupp, D., A. Strahler, and C. Woodcock, 1988; Autocorrelation and regularization in digital images: I. Basic theory, *IEEE Transactions on Geoscience and Remote Sensing*, **26(4)**: 463-473.
- Jupp, D., A. Strahler, and C. Woodcock, 1989; Autocorrelation and regularization in digital images: II. Simple image models, *IEEE Transactions on Geoscience and Remote Sensing*, **27(3)**: 463-473.
- Keser, N. (1970) A mapping and interpretation system for the forested lands of British Columbia, British Columbia Forest Service, Victoria, 29pp.
- Kimes, D. and Sellers, P. (1985) Inferring hemispherical reflectance of the Earth's surface for global energy budgets from remotely sensed nadir or directional radiance values, *Remote Sensing of Environment* **18**: 205-223.
- Kimes, D., Sellers, P. and Newcomb, W. (1987) Hemispherical reflectance variations of vegetation canopies and implications for global and regional energy budget studies, *Journal of Climate and Applied Meteorology*, **26**: 959-972.
- Kimes, D.S., Kerber, A.G. and Sellers, P.J. (1993) Spatial averaging errors in creating hemispherical reflectance (albedo) maps from directional reflectance data. *Remote Sensing of Environment* **45**: 85-94.
- Kimes, D.S., Newcomb, W.W., Nelson, R.F. and Schutt, J.B. (1986) Directional reflectance distributions of a hardwood and pine forest canopy. *IEEE Transactions on Geoscience and Remote Sensing* **24(2)**: 281-293.

- Li, X. and Strahler, A. H. (1985) Geometric-optical modeling of a conifer forest canopy. *IEEE Transactions on Geoscience and Remote Sensing*, **23**: 705-721.
- Li, X. and Strahler, A. H. (1986) Geometric-optical bidirectional reflectance modelling of a conifer forest canopy. *IEEE Transactions on Geoscience and Remote Sensing* **23**: 705-721.
- Li, X. and Strahler, A. H. (1992) Geometric-optical bidirectional reflectance modelling of the discrete crown vegetation canopy. *IEEE Transactions on Geoscience and Remote Sensing* **30**: 276-292.
- Li, X., Strahler, A. H. and Woodcock, C.E. (1995) A hybrid geometric optical-radiative transfer approach for modeling albedo and directional reflectance of discontinuous canopies. *IEEE Transactions on Geoscience and Remote Sensing* **33**: 466-480.
- Lillesand, T. and Kiefer, R. (1987) *Remote Sensing and Image Interpretation*. Toronto: Wiley.
- Nicodemous, F. E., Richmond, J. E., Hsia, J. J., Ginsberg, I. and Limperis, W. T. (1977) Geometrical considerations and nomenclature for reflectance. NBS Monograph 160. 52 p. National Bureau of Standards, Dept. of Commerce, Washington D.C.
- Nilson, T., and Peterson, U. (1994) Age dependence of forest reflectance: Analysis of main driving factors, *Remote Sensing of Environment* **48**: 319-331.
- Oetking, P. (1966) Photometric studies of diffusely reflecting surfaces with applications to the brightness of the moon, *Journal of Geophysical Research* **71**: 2505-2413.
- Pellikka, P. (1998) Development of correction chain for multispectral airborne video camera data for natural resource management. *Fennia* (Geographical Society of Finland), **176(1)**: 1-110.
- Pinty, B, Verstraete, M. M. and Dickinson, R.E. (1989) A physical model for predicting bidirectional reflectances over bare soil. *Remote Sensing of Environment*, **27**: 273-288.
- Privette, J.L., Emery, W.J. and Schimel, D.S. (1996) Inversion of a vegetation reflectance model with NOAA AVHRR data. *Remote Sensing of Environment*. **58**:
- Purgold, G.C., Whitlock, C.H., Wheeler, R.J. and LeCroy, S.R. (1994) A multiwavelength airborne radiometer scanner (ARS) for measuring surface bidirectional reflectance characteristics. *Remote Sensing of Environment*, **47**: 322-330.
- Ranson, K.J., Irons, J.R. and Daughtry, C.S.T. (1991) Surface albedo from bidirectional reflectance. *Remote Sensing of Environment*, **35**: 201-211.
- Ranson, K.J., Irons, J.R. and Williams, D.L. (1994) Multispectral bidirectional reflectance of northern forest canopies with the advanced solid-state array spectroradiometer (ASAS). *Remote Sensing of Environment* **47**: 276-289.
- Ross, J.K. and Marshak, A.L. (1989) Influence of leaf orientation and specular composition of leaf reflectance on the canopy bidirectional reflectance. *Remote Sensing of Environment*, **27**: 213-225.

- Rosema, A, Verhoef, W and Noorbergen, H. (1992) A new forest light interaction model in support of forest monitoring *Remote Sensing of Environment* **42**.
- Salisbury, J.W., Milton, N.M. and Walsh, P.A. (1987) Significance of non-isotropic scattering from vegetation for geobotanical remote sensing. *International Journal of Remote Sensing* **8(7)**: 997-1009.
- Seeliger, H. (1887) Zur theorie der beleuchtung der grossen planeten insbesondere des Saturn. *Abhdl. Bayer. Akad. Wiss. Math-Naturw. Kl. II.* **18**: 405-516.
- Seeliger, H. (1895) Theorie der beleuchtung staubformiger kosmischen masses insbesondere des Saturnes. *Abhdl. Bayer. Akad. Wiss. Math-Naturw. Kl. II.* **16**: 1-72.
- Schaaf, C., Li, X. and Strahler, A. (1994) Topographic effects on bidirectional and hemispherical reflectances calculated with a geometric-optical canopy model. *IEEE Transactions on Geoscience and Remote Sensing* **32(6)**: 1186-1193.
- Shoshany, M. (1991) The equifinality of bidirectional reflectance distribution functions of various microstructures. *International Journal of Remote Sensing* **12(11)**: 2267-2281.
- Spanner, M.A., Pierce, L.L., Peterson, D.L. and Running, S.W. (1990) Remote sensing of temperate coniferous forest leaf area index: the influence of canopy closure, understory vegetation and background reflectance, *International Journal of Remote Sensing*, **(11)**: 95-111.
- Spies, T.A. and Franklin, J.F. (1991) The structure of natural young, mature and old-growth forests in Washington and Oregon. *in: Wildlife and Vegetation of Unmanaged Douglas-Fir Forests* (L.F. Ruggiero et al. Eds.), *USDA Forest Service General Technical Report PNW-GTR-285*, Portland, OR, pp. 90-109.
- Strahler, A. H. and Jupp, D. L. B. (1990) Modeling Bidirectional Reflectance of Forests and Woodlands Using Boolean Models and Geometric Optics. *Remote Sensing of Environment* **34**: 153-166.
- Strahler, A. H., Woodcock, C. E. and Smith, J. (1986) On the Nature of Models in Remote Sensing. *Remote Sensing of Environment* **20**: 121-139.
- Swain, P. H. and Davis, S. M. (1978) *Remote sensing: the quantitative approach*. 396p. McGraw Hill, Toronto.
- Syrén, P. (1994) Reflectance anisotropy for nadir observations of coniferous forest canopies. *Remote Sensing of Environment* **49**: 72-80.
- Till, S.M., McColl, W.D. and Neville, R.A. (1983) Development, field performance and evaluation of the MEIS-II multi-detector electro-optical imaging scanner, *in Proceedings of the Seventeenth International Symposium on Remote Sensing of Environment*, Ann Arbor, Michigan, May 9-13, pp.1137-1146.
- Vane, D., Chrisp, M., Ihlnmk, D., Macenka, S. and Solomon J. (1984) Airborne visible/infrared imaging spectrometer: an advanced tool for earth remote sensing, *in Proceedings of the 1984 IEEE International Geoscience and Remote Sensing Symposium*, SP215, p.751-757.

- Walthall, C. Norman, J., Welles, J., Campbell, G. and Blad, B. (1985) Simple equation to approximate the bidirectional reflectance from vegetative canopies and bare soil surfaces. *Applied Optics* **24**: 383-387.
- Williams, D.L. (1991) A comparison of spectral reflectance properties at the needle, branch, and canopy level for selected conifer species. *Remote Sensing of Environment* **35**: 79-93.
- Woodcock, C.E., Collins, J.B., Jakabhazy, V.D., Li, X., Macomber, S.A. and Wu, Y. (1997) Inversion of the Li-Strahler canopy reflectance model for mapping forest structure. *IEEE Transactions on Geoscience and Remote Sensing* **35(2)**: 405-414.
- Wooley, J. T. (1971) Reflectance and transmittance of light by leaves. *Plant Physiology* **47**: 656-662.
- Wulder, M. A. (1998) Optical remote-sensing techniques for the assessment of forest inventory and biophysical parameters. *Progress in Physical Geography* **22(4)**: 449-476.

Appendix C. AVIRIS and MEIS II Sensors

AVIRIS

AVIRIS is a second-generation imaging spectrometer developed at the Jet Propulsion Laboratory for use in earth remote sensing studies across a broad spectrum of scientific disciplines, including botany, geology, hydrology and oceanography (Vane et al. 1984). Construction and calibration of the sensor was completed in June 1987.

AVIRIS acquires images in 220 contiguous 10-nanometer (nm) spectral bands in the region between 0.40 and 2.45 micrometers. The instantaneous field of view of AVIRIS is 1 milliradian and the field of view as defined by the scan angle is 30 degrees. This produces images covering a 10.5km swath composed of picture elements (pixels) which subtend 20m on the ground from the 20km altitude of the NASA U-2. AVIRIS gathers spectral images in the whisk-broom imaging mode, employing fore optics with a scan mirror which scans in one direction, then rapidly returns to the start position for the next scan line. The scan rate and detector readout timing were designed to provide a 17 percent spatial over sampling at sea level in both the cross-track and along-track dimensions. This results in the acquisition of 614 pixels in each scan line. Geometric rectification removes the over sampling, resulting in an image 550 pixels across. Twelve scans are completed per second. During the fly-back portion of the scan cycle, a shutter closes the fore-optics from the rest of the optical system while a detector dark current measurement is made.

The fore-optics is connected to four spectrometers with optical fibers. Spectrometer A contains a 32-element line array of silicon detectors and spectrometers B, C, and D each employ 64-element line arrays of iridium antimonide detectors. While a total of 224 spectral bands are actually acquired, the readout architecture of the detector arrays renders the first band of each array unusable; there are thus 220 useable raw spectral bands. The useable spectral ranges of spectrometers A, B, C, and D are 0.40 to 0.71, 0.68 to 1.28, 1.24 to 1.86, and 1.83 to 2.45 nm, respectively, as currently aligned. During radiometric calibration the spectral region covered by the 220 raw spectral bands is resampled to remove overlap between spectrometers and equalize the spectral sampling interval across the entire 0.40 to 2.45 nm region. This results in 210 spectral bands over this region in the radiometrically corrected data.

Radiometrically corrected means converted into units of radiance, as opposed to the unitless AVIRIS digital numbers. Radiance is measured in units of microwatts per square centimeter

per nanometer per steradian, or $\mu\text{W} / (\text{cm}^2 * \text{nm} * \text{sr})$. AVIRIS radiometric calibration factors are calculated by measuring the response of AVIRIS to an integrating sphere (a known target illuminated by a known light source). This calibration is accurate to within 7%, absolute, over time. Intra-flight accuracy is within 2%.

<i>Spectrometer</i>	Spectral Range (nm)	Sampling Interval (nm)	SN
A	396.9 - 702.7	9.6 - 10.1	150:1
B	674.7 - 1283	8.8 - 9.2	140:1
C	1244 - 1867	9.7 - 10.0	70:1
D	1830 - 2454	9.9 - 11.5	30:1

Table C-1. AVIRIS sensor specifications

<i>Flight Data</i>	Pass 1	Pass 2
Flight Number	930829C run 03	930902A run 05
Date	August 29, 1993	September 02, 1993
GMT start/ end	19:12:36 / 19:15:15	22:11:18 / 22:23:41
Latitude (ϕ) start/end	48:23:41 / 48:40:29 N	48:23:31 / 48:39:30 N
Longitude start/end	-123:39:04 / -123:44:40	-123:39:04 / -123:44:00

Table C-2. AVIRIS flight specifications

MEIS II

MEIS II (MEIS hereafter) is an airborne multi-spectral pushbroom CCD scanner with a spectral sensitivity between 380nm and 1000nm. MEIS records eight separate spectral channels, at user-defined wavelengths (using front-mounted filters); six of these channels are nadir-looking, while two of these channels are configured to produce stereo images (i.e. fore- and aft- pointing). The sensor records 6000 pixels in the x axis, with a field of view of 39.67°, while the forward movement of the aeroplane generates the y axis. The ground instantaneous field of view (GIFOV) can range from 0.3m to 3m depending on flight altitude above ground. GIFOV for the 1996 Sooke Lake data set is nominally 1m. Table C-3 gives the filter set used in the 1993 flights and table C-4 gives a detailed breakdown of the MEIS sensor parameters.

filter (centre wavelength(nm)) peak transmittance (%) mean bandwidth (nm)							
CH0	CH1	CH2	CH3	CH4	CH5	CH6	CH7
3E(549)	3V(641)	3T(518)	3L(875)	3F(549)	3S(448)	22(553)	3G(675)
0.38	0.68	0.72	0.90	0.38	0.73	0.44	0.50
31.80	37.00	23.90	54.70	31.80	30.30	13.80	39.50

Table C-3. Stereo A MEIS II filter set, 1993 (from Leckie, D. (edit.) Proceedings of the International Forum on Airborne Multispectral Scanning for Forestry and Mapping (with Emphasis on MEIS), Forestry Canada Information Report PI-X-113)

Scanner Type	Pushbroom CCD scanner 8 spectral channels
Spectral Response	Range 390-1100 Spectral bands selected by front-mounted filters (blue-shift-free)
Field of View	Total swath 39.66°, with real time data resampler Pixel size 0.70 mrad with resampler (0.53 mrad without the resampler) Selectable by choice of lens focal length
Detector Type	Fairchild CCD 122 silicon, buried channel 1728 element linear array, 13 micrometre X13 micrometre photoelements on 13 micrometre centres
Lens Type	Angenieux, type R2, format 35 mm Focal length 24.61 mm f/2.2 - f/22
Line Sample Rates	25, 50, 100, 200 Hz (operator selectable to match aircraft velocity and altitude)
Gains	1, 2, 4, 8, 16, 32 (operator selectable)
Exposure Times	5 msec (line sample rate) ⁻¹ by powers of 2 (operator selectable)
Data Formats	1024 pixels recorded per channel per scan line 8 bit digitization Ancillary data recorded (sensor parameters: aircraft roll from inertial navigation system)
Signal/Data Processing	Correlated double sampling of CCD signal Real-time dark current subtraction Real-time image data resampling, provides pixel registration, geometric corrections for optical distortions, and roll correction Storage in programmable memory of radiometric and geometric coefficients for 10 sets of filters Real-time aircraft roll correction, using roll signal from inertial navigation signal - up to +/- 22.5° - up to +/- 4.7° for unattenuated image swath width Data rate to 1.75 M bits/sec/channel
Size, Weight, Power	Camera head: 23 x 36 x 46 cm, 30 kg, 7A max, 28V DC, 0.8A max, 115V AC, 400Hz Data processor: 48 x 22 x 48 cm, 27 kg 14A max, 28V DC Resampler: 48 x 22 x 48 cm, 20 kg, 11 A max, 28V DC Power supply: 48 x 22 x 46 cm, 28 kg.
Environment	Ambient temperature operating range - camera head -50° to +40° C - processor and resampler 0° to +40° C Humidity operating range - camera head 0% to 95% RH, non-condensing - processor and resampler 20% to 85% RH, non-condensing
Interfaces	Alice real-time display Inertial navigation system High density digital tape recorder

Table C-4. MEIS-II specifications (from Leckie, D. (edit.) Proceedings of the International Forum on Airborne Multispectral Scanning for Forestry and Mapping (with Emphasis on MEIS), Forestry Canada Information Report PI-X-113)

Appendix D. Solar Angle Calculation

Celestial objects, like the sun, are recorded in astronomical reference guides such as the *Astronomical Almanac* using the equatorial coordinate system. This coordinate system refers the position of celestial objects to the plane of the Earth's equator. However, the positions of the illumination (sun) and camera positions used to model terrestrial surfaces utilize a horizon coordinate system. In order for the models accurately portray the solar positions for the two AVIRIS passes, it was necessary to convert the equatorial coordinate-based AVIRIS reference data found in Table 1 to horizon coordinates found in Table 2. The following sections explain this process in more detail. The example calculation is modified from an example found in Some of the explanation is taken from Duffett-Smith (1979).

Table D.1 Solar position at time of AVIRIS flight

	Pass 1	Pass 2
<i>Flight Data</i>		
Flight Number	930829C run 03	930902A run 05
Date	August 29, 1993	September 02, 1993
GMT start/end	19:12:36 / 19:15:15	22:11:18 / 22:23:41
Latitude (ϕ) start/end	48:23:41 / 48:40:29 N	48:23:31 / 48:39:30 N
Longitude start/end	-123:39:04 / -123:44:40	-123:39:04 / -123:44:00
<i>Almanac Data</i>		
Right ascension (α)	10:29:54	10:44:25
Declination (δ)	9:25:50	7:59:30
GST (0hr GMT)	22:28:51	22:44:37
LST	11:12:36	14:11:18
<i>Calculated Values</i>		
altitude (a)	48.84	42.68
Azimuth (A)	155.97	214.39

Before giving the equations used to translate from one coordinate system to another and an example, a brief description of these coordinate systems is apt. The following section is extracted from Duffett-Smith (1979). All reference systems are designed to locate celestial objects on the sphere that has the Earth (or the Solar System) at its centre. This sphere is called the *celestial sphere*. The horizon coordinate system is simply the portion of the sphere that lies above the observer's horizon. Figure D-1 illustrates this system where O is the observer's location, NESW are the points of the compass prescribing direction to the horizon plane and Z is the point directly overhead the observer; the zenith point. Star X is can then be located using the horizon coordinates, azimuth (A) and altitude(a).

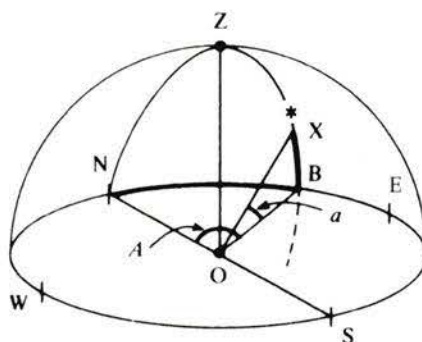
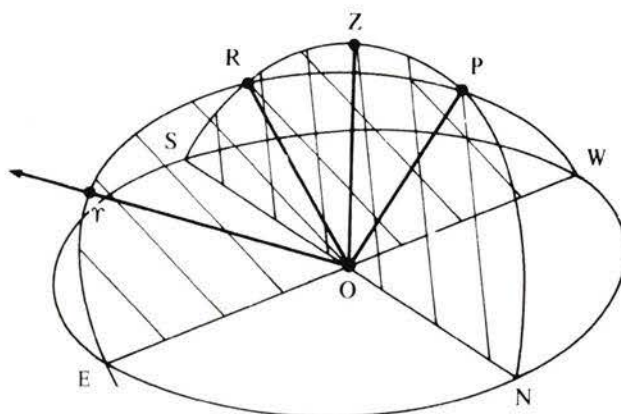


Figure D-1. Horizon coordinates (from Duffett-Smith 1979)

The equatorial coordinate system uses as a reference the plane that extends out from the Earth's equator: the line through the centre (C) of the Earth in Figure D-1. The horizon plane touches the Earth at O, the observer's location, and the angle between these planes is $90^\circ - \phi$, where ϕ is the observer's geographical latitude ($48^\circ 23'$ for the Sooke Lake study sites). Three dimensional representations of this system, Figures D-2&3, show the observer's horizon plane, NESW, and zenith point, Z. In these figures, the equatorial plane has been extended to cut the celestial sphere along the circle E γ RW. At right angles to the equatorial plane along the line OP lies the axis of rotation of the Earth; it intersects the celestial sphere at P, the *north celestial pole*, or *north pole* for short. Since this is the line about which the Earth spins, all the stars appear to describe circles in the sky about P.



(a)

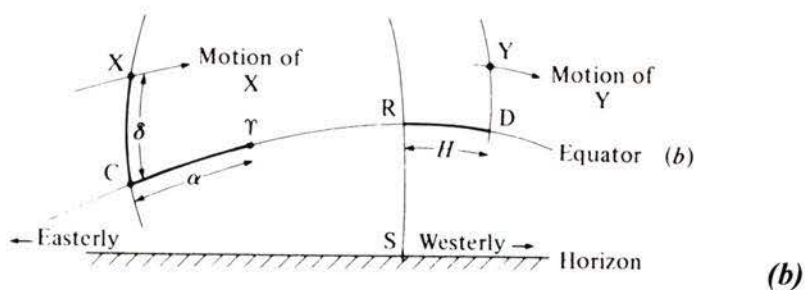


Figure D-2. Equatorial coordinates (a) on the celestial sphere, (b) as seen from the ground (from Duffett-Smith 1979)

Figure D-2b shows the situation as seen by the observer O looking up at the sky. The south point of his horizon is marked and so is the imaginary trace of the equator, C γ RD. The arc descending down through R and S is the great-circle which goes through NPZRS in Figure D-2a. The arc extending through XC is another great circle, not marked in Figure D-2a, which goes through PXC. Consider the star X. The arc XC, or angle subtended at O by the points X and C, is called the *declination*, δ of X, that is ‘how far up’ from the equator coordinate. The other coordinate, ‘how far round’, is defined with respect to a fixed location in the sky, marked by the symbol γ . This direction, called the *vernal equinox or the first point of Aries*, lies along the line of intersection of the plane of the Earth’s equator with that of the Earth’s orbit around the Sun. This point remains fixed with respect to the stars and is called the *right ascension*, α , is the angle subtended at O by the points γ and C.

Throughout the course of the day the star X moves steadily westwards along the circle centred on P, completing one revolution in 24 hours of sidereal time¹. Since this circle is a parallel circle to that of the equator the declination does not change. Furthermore, since the direction γ is fixed in the heavens, it appears to move along the equator at exactly the same rate as X moves along its circle. Hence the right ascension does not change either. Thus α and δ are ideal coordinates for describing the positions of the stars and other ‘fixed’ heavenly bodies.

Related to the right ascension is another ‘how far around’ coordinate called the *hour-angle*, H. For the star Y (Figure D-2a) it is defined as the angle subtended at O by the points R and D and is a measure of how far the star has travelled along the equator from the southern point

¹ A sidereal day is slightly shorter than a solar day, 24 hours of solar time corresponding to 23h 56m of sidereal time. Sidereal time differs from solar time (of which GMT is an example) in that it is based on the time taken for the sun to return to the same position with respect to the background of stars (about 365 1/4 solar days). Solar time, on the other hand, uses as reference the number of revolutions the earth makes in this time (about 366 1/4 revs).

R. In the following example, the right ascension recorded in the Astronomical Almanac must be converted to the hour-angle.

Formulae	where
$LST = GST(0hr\ GMT) + GMT(start) - (longitude/15)$	GST Greenwich sidereal time
$H = LST - \alpha$	LST local sidereal time
$\sin a = \sin \delta \sin \phi + \cos \delta \cos H \cos \phi$	H hour angle
$\cos A = [\sin \delta - (\sin \phi \sin a)] / \cos \phi \cos a$	A azimuth
	a altitude
	δ declination
	α righth ascension
	ϕ Latitude

Example using August 29 data:

- Starting with the GST for 0 hours (22:28:51) from the Astronomical Almanac, calculate LST

$$\begin{aligned} LST_{829} &= GST + GMT - Long^\circ ((DMS/15)) \\ &= 22.4808 + 19.21 - (123.6511 / 15) \\ &= 33.447426 \end{aligned}$$

- Calculate the hour-angle (H) using α from Almanac and LST

$$\begin{aligned} H_{829} &= LST_{829} - \alpha \\ &= 33.447426 - 10.499833 \quad [\text{note: if negative, add 24}] \\ &= 22.949093 \end{aligned}$$

- Change hour-angle to degrees

$$\begin{aligned} H_{829}^\circ &= H_{829} \times 15 \\ &= 344.2364 \end{aligned}$$

- Calculate altitude (a)

$$\begin{aligned} \sin a &= \sin \delta \sin \phi + \cos \delta \cos H \cos \phi \\ &= [\sin(9.4305556) \times \sin(48.394722)] + [\cos(9.4305556) \times \\ &\quad \cos(48.394722) \times \cos(344.2364)] \\ &= 0.7529046 \\ a_{829} &= 48.84261^\circ \end{aligned}$$

- Calculate azimuth (A)

$$\begin{aligned} \cos A &= [\sin \delta - (\sin \phi \sin a)] / \cos \phi \cos a \\ &= \{\sin(9.4305556) - [(\sin(48.394722) \times \sin(48.84261))]\} / \\ &\quad [\cos(48.394722) \times \cos(48.84261)] \\ &= -0.9133343 \\ A' &= 155.97^\circ \end{aligned}$$

Calculators can only return inverse trigonometric functions correctly over half the range of 0° to 360° . It is thus necessary to check to see if an adjustment is needed. Thus, if $\sin H$ is negative, then the true azimuth is $A = A'$; and if $\sin H$ is positive, then the true azimuth is $A = 360 - A'$.

$$\begin{aligned} \sin H &= \sin(344.2364) \\ &= -0.27166899 \end{aligned}$$

$$\text{Giving } A_{829} = A' = 155.97^\circ$$

Appendix E. POV-Ray Source Code Example: Site 10

```
// Here is a sample Persistence Of Vision POV-Ray 3.0
// ray-tracing tree file.

#version 3.0
global_settings { assumed_gamma 2.2 }

#include "shapes.inc"
#include "colors.inc"

// Set up the camera, nadir view, with a focal area
// of 20m2 and with an orthographic projection

camera {
  orthographic
  location < 0, 0, 0>
  right <41*4/3, 0, 0>
  up <0, 41, 0>
  translate < -10, 200, 10>
  look_at <-10, 0, 10>
}

// Add the light source as calculated with the
// solar angle calculator

light_source {<2351.1, 7547.1, 6124.9> color White} // r5

// Add some colored boxes to frame scene from above
object { box { <0.0, 0.0, 0.0> <10, 10, 10> } translate <0, 100, 30>
pigment {color rgb <1.0, 0.0, 0.0>} }
object { box { <0.0, 0.0, 0.0> <10, 10, 10> }
translate <-40, 100, 30> pigment {color rgb <1.0, 1.0, 0.0>} }
object { box { <0.0, 0.0, 0.0> <10, 10, 10> }
translate <10, 100, 30> pigment {color rgb <1.0, 1.0, 0.0>} }
object { box { <0.0, 0.0, 0.0> <10, 10, 10> }
translate <10, 100, -20> pigment {color rgb <1.0, 1.0, 0.0>} }
object { box { <0.0, 0.0, 0.0> <10, 10, 10> }
translate <-40, 100, -20> pigment {color rgb <1.0, 1.0, 0.0>} }

// Finally, get the trees using an 'include' file
#include "s10r5map&plot.inc"
```

Here is the 'include' file with directions on how and where to build the trees. The last directions are to replicate the tree map 4 times over in the sun-ward direction

```
// Persistence Of Vision raytracer version 3.0 tree file.
// By Charles Burnett
// This image contains a tree map and plot placement
```

```
plane {
  <0, 0.878, -0.479>, -0
  pigment {
    color rgb <1.0, 1.0, 1.0>
```

```

    }
  }

#declare PlotMap=
union {

// crowns

object { cone { 8.31649495 *y, 0.0, 0.0, 2.25111115
  translate
  < -6.8923077 , 19.7470218 , 5.71153846 > } pigment
  {color Green}}

object { cone { 7.0707953 *y, 0.0, 0.0, 1.54948764
  translate
  < -3.9923077 , 17.5827531 , 6.31153846 > } pigment
  {color Green}}

object { cone { 7.74439703 *y, 0.0, 0.0, 1.92888472
  translate
  < -7.7923077 , 16.4764769 , 1.81153846 > } pigment
  {color Green}}

object { cone { 7.96305626 *y, 0.0, 0.0, 2.05204158
  translate
  < -3.7923077 , 17.4044913 , 2.71153846 > } pigment
  {color Green}}

object { cone { 7.40824118 *y, 0.0, 0.0, 1.73954948
  translate
  < -3.3923077 , 17.276253 , 4.51153846 > } pigment
  {color Green}}

object { cone { 7.19633275 *y, 0.0, 0.0, 1.62019491
  translate
  < -4.5923077 , 13.0359122 , -2.4884615 > } pigment
  {color Green}}

object { cone { 8.35558702 *y, 0.0, 0.0, 2.27312923
  translate
  < 3.60769231 , 19.2799882 , 4.71153846 > } pigment
  {color Green}}

object { cone { 8.32723484 *y, 0.0, 0.0, 2.25716025
  translate
  < -2.1923077 , 15.5703253 , -1.9884615 > } pigment
  {color Green}}

object { cone { 8.88491971 *y, 0.0, 0.0, 2.57126873
  translate
  < 2.30769231 , 17.2854345 , -0.8884615 > } pigment
  {color Green}}

object { cone { 8.4848713 *y, 0.0, 0.0, 2.34594686
  translate
  < 3.90769231 , 14.3589886 , -4.7884615 > } pigment
  {color Green}}

// + 15 more

```

```

//stems

object { cone { 16.6329899 *y, 0.27 ,0.0, 0.27
  translate
  < -6.8923077 , 3.11403186 , 5.71153846 > } pigment
{color Brown}}

object { cone { 14.1415906 *y, 0.142 ,0.0, 0.142
  translate
  < -3.9923077 , 3.44116248 , 6.31153846 > } pigment
{color Brown}}

object { cone { 15.4887941 *y, 0.201 ,0.0, 0.201
  translate
  < -7.7923077 , 0.98768283 , 1.81153846 > } pigment
{color Brown}}

object { cone { 15.9261125 *y, 0.225 ,0.0, 0.225
  translate
  < -3.7923077 , 1.47837876 , 2.71153846 > } pigment
{color Brown}}

object { cone { 14.8164824 *y, 0.169 ,0.0, 0.169
  translate
  < -3.3923077 , 2.45977062 , 4.51153846 > } pigment
{color Brown}}

object { cone { 14.3926655 *y, 0.1515 ,0.0, 0.1515
  translate
  < -4.5923077 , -1.3567533 , -2.4884615 > } pigment
{color Brown}}

object { cone { 16.711174 *y, 0.2755 ,0.0, 0.2755
  translate
  < 3.60769231 , 2.56881416 , 4.71153846 > } pigment
{color Brown}}

object { cone { 16.6544697 *y, 0.2715 ,0.0, 0.2715
  translate
  < -2.1923077 , -1.0841444 , -1.9884615 > } pigment
{color Brown}}

object { cone { 17.7698394 *y, 0.362 ,0.0, 0.362
  translate
  < 2.30769231 , -0.484405 , -0.8884615 > } pigment
{color Brown}}

object { cone { 16.9697426 *y, 0.2945 ,0.0, 0.2945
  translate
  < 3.90769231 , -2.610754 , -4.7884615 > } pigment
{color Brown}}

// + 15 more

}

// Now place 'copies' of this tree map to the sun-ward of the
// main image area, so that shadows are cast in appropriate
// fashion.

#declare Count=0
#while (Count < 5)
  object{PlotMap
    translate z*20*Count
    translate y*10.9*Count // note that this is up-slope
    translate x*-30}
  #declare Count=Count+1
#end

#declare Count=0

```

```
#while (Count < 5)
  object{PlotMap
    translate y*10.9*Count
    translate z*20*Count
    translate x*-10}
  #declare Count=Count+1
#end
```

```
#declare Count=0
#while (Count < 5)
  object{PlotMap
    translate z*20*Count
    translate y*10.9*Count
    translate x*10}
  #declare Count=Count+1
#end
```

```
#declare Count=0
#while (Count < 5)
  object{PlotMap
    translate z*20*Count
    translate y*10.9*Count
    translate x*30}
  #declare Count=Count+1
#end
```

VITA

Surname: Burnett Given Names: Charles Nils
Place of Birth: Auckland, New Zealand

Educational Institutions Attended:

University of Victoria 1993-1999
University of Alberta, Edmonton 1987-1993

Degrees Awarded:

B.Sc. (Specialization in Physical Geography), University of Alberta 1993

Posters & Proceedings Papers:

Burnett, C., D. Leckie, C. Jay, J. Busler and J. Aitken (1999) The effect of severe topography on image resolution: implications for flight planning, post-processing and applications *in* Proceedings of the Fourth International Airborne Remote Sensing Conference and Exhibition / 21st Canadian Symposium on Remote Sensing, Ottawa, Ontario, Canada, 21-24 June 1999.

Leckie, D., C. Burnett, T. Nelson, C. Jay, N. Walsworth, F. Gougeon and E. Cloney (1999) Forest parameter extraction through computer-based analysis of high resolution imagery *in* Proceedings of the Fourth International Airborne Remote Sensing Conference and Exhibition / 21st Canadian Symposium on Remote Sensing, Ottawa, Ontario, Canada, 21-24 June 1999.

Burnett, C.N., D.G. Leckie and Miller, L.B. (1998) A Survey of Current and Potential Uses of Remote Sensing for the Restoration of Natural Systems, *at the* "Helping the Land Heal: Ecological Restoration in British Columbia" Conference, Victoria, BC Nov. 5-8.

Burnett, C.N., Wulder, M., Daley, N.M.A., Niemann, K. O. and Goodenough, D.G. (1998) Directional variability in 1m *casi* imagery: an analysis using semi-variance range and slope shape, *in* Proceedings of the International Geoscience and Remote Sensing Symposium, Seattle, 6-10 July, p. 3242-44.

Burnett, C.N., Wulder, M., Daley, N.M.A., Niemann, K. O. and Goodenough, D.G. (1998) Comparison of generalized and scale-sensitive windows in the estimation of tree crown position using local maximum filters, *in* Proceedings of the 1st International Workshop on Scaling and Modeling in Forestry, Montreal, February, 1998.

Burnett, C. N., Hay, G., Niemann, K. O., Goodenough, D. (1997) Modeling bidirectional reflectance functions of conifer canopies using 3-D graphics, *in* Proceedings of the 3rd International Airborne Remote Sensing Conference, Copenhagen.

Burnett, C. N., Niemann, K. O., Goodenough, D. and H. Barclay. (1996) Modeled directional variation in radiance versus AVIRIS-measured change for a non-homogeneous Douglas-fir forest: preliminary findings, *in* Proceedings of the Second International Airborne Remote Sensing Conference, San Francisco.

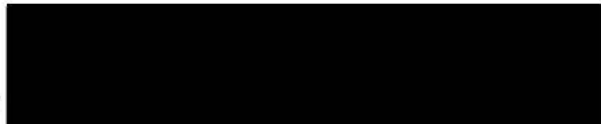
PARTIAL COPYRIGHT LICENSE

I hereby grant the right to lend my thesis to users of the University of Victoria Library, and to make single copies only for such users or in response to a request from the Library of any other university, or similar institution, on its behalf or for one of its users. I further agree that permission for extensive copying of this thesis for scholarly purposes may be granted by me or a member of the University designated by me. It is understood that copying or publication of this thesis for financial gain shall not be allowed without my written permission.

Title of Thesis:

An Exploration of Conifer Canopy Anisotropy:
3D Modeling Versus Airborne Imaging Spectrometer and
Multispectral Scanner Imagery

Author



Charles Nils Burnett

April 30, 1999